Micromechanics Analysis of Space Simulated Thermal Deformations and Stresses in Continuous Fiber Reinforced Composites

by

David Earl Bowles

Dissertation submitted to the Faculty of the
Virginia Polytechnic Institute and State University
in partial fulfillment of the requirements for the degree of

Doctor of Philosophy

in

Engineering Mechanics

APPROVED:

O. H. Griffin Jr., Chairman

M. W. Hyer   K. L. Reifsnider

C. W. Smith   S. S. Tompkins

December 1989

Blacksburg, Virginia

Micromechanics Analysis of Space Simulated Thermal Deformations and Stresses in Continuous Fiber Reinforced Composites

by

David Earl Bowles

O. H. Griffin, Jr., Chairman

Engineering Mechanics

(ABSTRACT)

Space simulated thermally induced deformations and stresses in continuous fiber reinforced composites were investigated with a micromechanics analysis. The investigation focused on two primary areas. First, available explicit expressions for predicting the effective coefficients of thermal expansion (CTE's) for a composite were compared with each other, and with a finite element (FE) analysis, developed specifically for this study. Analytical comparisons were made for a wide range of fiber/matrix systems, and predicted values were compared with experimental data. All of the analyses predicted nearly indentical values of the axial CTE, α_1, for a given material system, and all of the predictions were in good agreement with the experimental data. Results from the FE analysis, and those from the solution of a generalized plane strain boundary value problem, were in excellent agreement with each other, and with the experimental data for the transverse CTE, α_2. Less rigorous formulations were in poor agreement with the experimental data.

The second area of investigation focused on the determination of thermally induced stress fields in the individual constituents. Stresses predicted from the FE analysis were compared to those predicted from a closed-from solution to the composite cylinder (CC) model, for two carbon fiber/epoxy composites. A global-local formulation, combining laminated plate theory and FE analysis, was used to determine the stresses in multidirectional laminates. Thermally induced damage initiation predictions were also made. The type of analysis (i.e. CC or FE) was shown to significantly affect

the distributions and magnitudes of the predicted stresses. Thermally induced matrix stresses increased in absolute value with increasing fiber volume fraction, but were not a strong function of fiber properties. Multidirectional $[0_2/\pm\theta]_s$ laminates had larger predicted thermally induced matrix stresses than unidirectional ([0]) laminates, and these stresses increased with increasing lamination angle θ. Thermally induced matrix failure predictions, using a maximum stress failure criterion based on the normal interfacial stress component and the measured transverse lamina strength, were in excellent agreement with experimental data.

Acknowledgements

The author wishes to thank Professor O. H. Griffin, Jr. for his guidance and support during the course of this work. The author would also like to thank the other members of his committee for their helpful comments and endurance through this rather lengthy process. A special thanks is also given to Dr. Stephen S. Tompkins of NASA Langley Research Center for his many helpful comments and suggestions, as well as his continuous encouragement. Finally, the author would like to thank his wife   for her unending love, patience, support, and encouragement, without which none of this would have been possible.

Table of Contents

List of Illustrations

List of Tables

1.0 Introduction

Continuous graphite fiber reinforced composites are candidate materials for many space structures because of their capability for high stiffness, low coefficient of thermal expansion, and light weight. This combination of properties allows for the design of large stiff structures with minimal thermal distortions. Examples of applications currently under consideration include the large truss structure of NASA's Space Station Freedom (SSF)[1], Figure 1, and the support structure and reflector panels for NASA's Large Deployable Reflector (LDR) spacecraft[2]. The NASA Hubble Space Telescope, already built and scheduled for launch in 1990, makes extensive use of composites in the optics metering and support structure[3] (Figure 2). Although composite materials offer the potential for enhanced performance and significant weight savings, there are concerns about their long-term stability in the space environment.

Materials in the space environment are exposed to ultraviolet and particulate radiation, atomic oxygen, vacuum, micrometeoroids, and large cyclic changes in temperature[4]. The level of exposure to most of these parameters depends upon the orbit and protection systems on the spacecraft. For example, spacecraft in low-earth-orbit (LEO), approximately 250 to 500 miles, are exposed to significant amounts of energetic atomic oxygen. In geostationary-earth-orbit (GEO), at approximately 22,000 miles, the levels of atomic oxygen are negligible, but there are significant amounts of particulate (electron and proton) radiation. Spacecraft are exposed to vacuum, ultraviolet radiation, and the threat of micrometeoroid impact in both orbits.
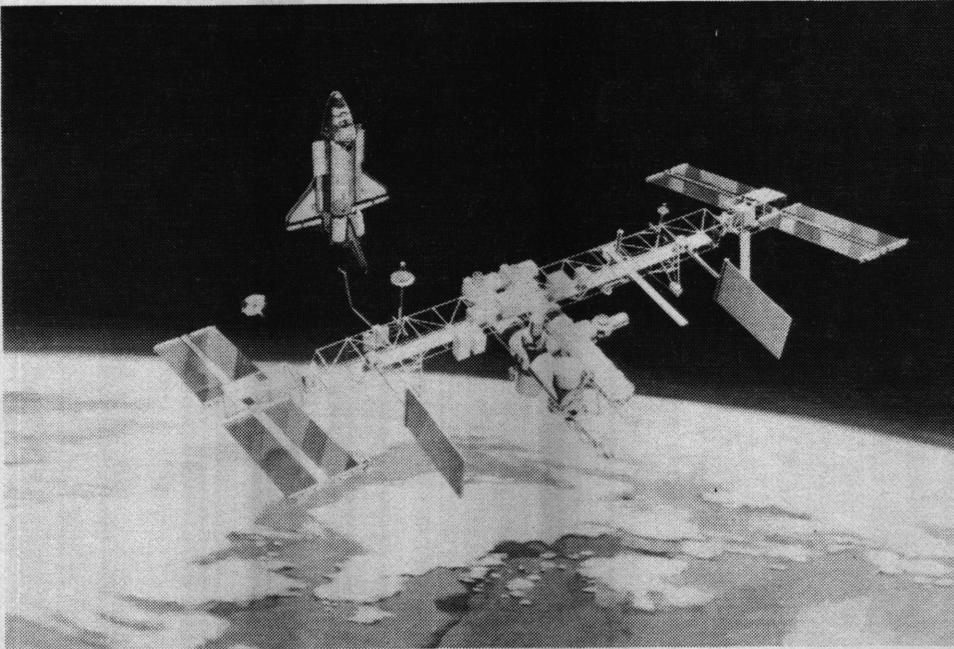
Figure 1. NASA Space Station Freedom.
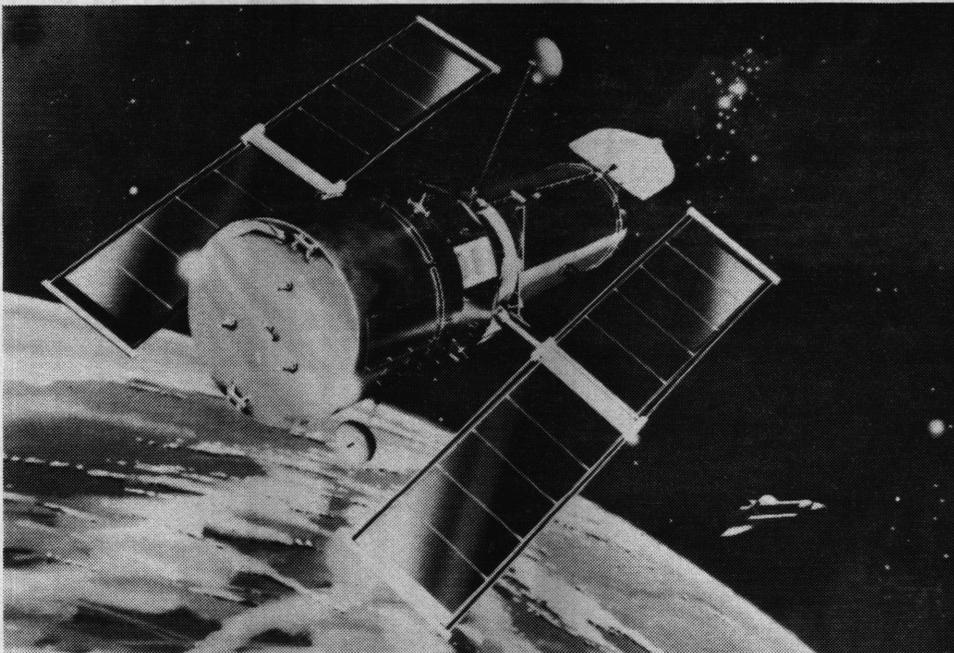
Figure 2. NASA Hubble Space Telescope.

Temperature cycling also occurs in both orbits, however the frequency of the cycling does vary with the orbit. In LEO, spacecraft are exposed to approximately 16 cycles per day. A LEO spacecraft designed for a 30 year lifetime, such as SSF, will experience approximately 175,000 thermal cycles. In GEO, the thermal cycling frequency is 1 per day. The maximum and minimum temperatures in a given cycle can be controlled by various thermal control/protection schemes, including active heating/cooling, and/or passive coatings and enclosures. The coating system proposed for the truss structure tubes of SSF have a predicted "worst case" temperature cycle of $\pm150\,^\circ$F [1].

In order to successfully design spacecraft structures with composite materials the effects of the space environment must be well understood. Most of the environmental parameters discussed above can affect the response and performance of composite materials during the design lifetime of the structure[4]. Previous research has shown that large temperature changes and/or repeated thermal cycling can cause significant damage in composite materials and adversely affect their performance[5-10] (Figure 3). The majority of past research has focused on analysis and testing of laminate response. However, the effects of constituent properties and microstructural characteristics (i.e. micromechanics) have not been thoroughly investigated for composites exposed to the thermal environment of space.

The objective of this research is to analyze the deformations and stresses, induced by thermal loading, in continuous fiber reinforced composites using the properties and behavior of the constitutents (i.e. fiber, matrix, and interface). The research will focus on two primary areas. First, available explicit expressions for predicting effective coefficients of thermal expansion for the composite will be compared with each other, and with a finite element analysis that was developed as part of this research. Comparisons will be made for a wide range of fiber/matrix systems to determine the influence of the constituent properties. All of the predictions will be compared with experimental data to assess the validity and shortcomings of the individual analyses. The remainder of the research will focus on the determination of thermally induced stress fields in the individual

$[0_2/90_2]_s$ P75/934 Graphite/Epoxy
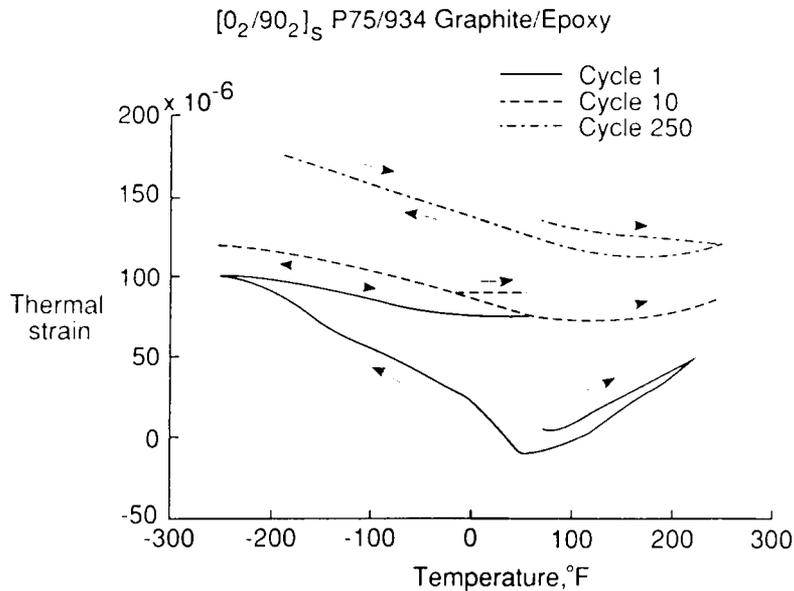
Figure 3. Effects of thermal cycling on cross-ply graphite/epoxy laminates.

constituents. Stresses predicted from a finite element analysis will be compared to those predicted from a closed-form analysis available in the literature. The constituent properties and microstructure that control the behavior will be identified and material modifications to improve the behavior will be suggested. A simple global/local formulation will be used to determine the influence of multiple ply laminate constraints on the constituent stresses. Thermal stress calculations will be used to predict probable damage initiation locations, and the results will be compared to experimentally observed damage in polymer matrix composites.

Four papers have been written and published by the author during the course of this research. These papers describe an experimental study of thermally induced microcracking in high modulus graphite/epoxy[10], the micromechanics finite element analysis[11], the prediction of effective coefficients of thermal expansion[12], and the analysis of thermally induced matrix stresses[13]. A majority of the information contained in these papers will be included in this report. Also included will be new results that have yet to be published.

2.0 Literature Review

The micromechanics literature can be divided into two categories. The first deals with the development of explicit expressions for directly predicting the effective properties of the composite from the properties of the constituents. The second category covers analyses that provide detailed information about the displacements, strains, and stresses in the composite from which the effective properties can be calculated. Extensive research for general multiphase composite materials has been conducted and published in both of these categories. This review will be limited to those papers dealing specifically with continuous fiber reinforced composites. Furthermore, this review will address only those papers that deal specifically with predicting the effective coefficients of thermal expansion (CTE's), or present stress analyses that are applicable to thermally induced loading.

2.1 Effective Coefficients of Thermal Expansion

Numerous expressions have been derived, with varying degrees of complexity, for predicting the in-plane CTE's of unidirectional continuous fiber reinforced composites. A summary of research on prediciting both the effective mechanical and thermal properties of composites was given by Chamis and Sendeckyj[14], where various analyses were compared with each other and experimental data. Chamis and Sendeckyj divided the analysis methods into the following major categories: strength of materials, self-consistent models, variational or energy approaches, and exact
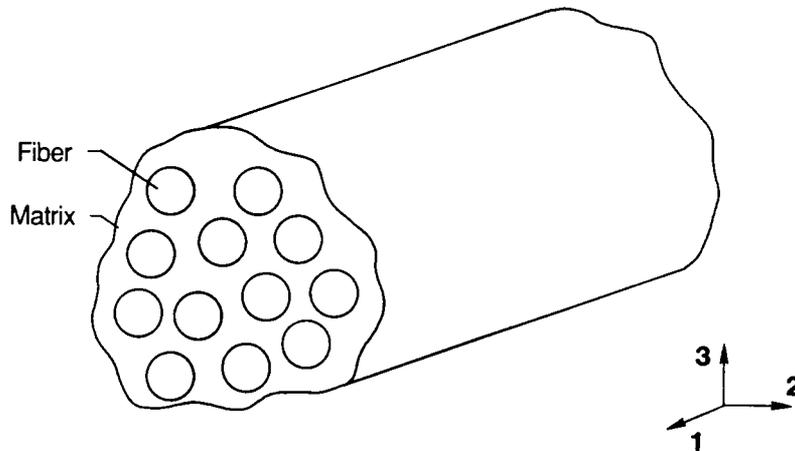
Figure 4. Unidirectional composite geometry and principal material coordinates.

(i.e. using the concept of a periodic array of fibers and a repeating unit cell). Several theories have been proposed since this publication, and much more experimental data exists on current material systems. A brief description of some of the more widely used current analyses will be given here.

The geometry of the problem under consideration is shown in Figure 4. There are several basic assumptions that are common to all of the analyses to be presented and can be stated as follows:

1. The fibers are circular in cross-section and infinitely long in the 1-direction.

2. All of the constituents exhibit linear elastic material behavior.

3. The displacements are continuous across the fiber/matrix interface.

4. The temperature distribution is uniform throughout the body, and the constituent material properties do not vary with temperature.

Shapery[15] derived expressions for the effective longitudinal and transverse CTE's (α_1 and α_2, respectively) of a unidirectional composite with isotropic fibers embedded in an isotropic matrix,

based on a variational energy appraoch. These expressions may be written as

$$\alpha_1 = \frac{E_1^f \alpha_1^f V^f + E^m \alpha^m V^m}{E_1^f V^f + E^m V^m} \tag{2.1.1}$$

and

$$\alpha_2 = (1 + \nu^m)\alpha^m V^m + (1 + \nu_{12}^f)\alpha_1^f V^f - \alpha_1 \nu_{12} \tag{2.1.2}$$

The terms E, ν, and V refer to Young's modulus, Poisson's ratio, and phase volume fraction, respectively. Terms without superscripts in equations (2.1.1) and (2.1.2) refer to effective composite properties. All other terms with superscripts of f and m, refer to fiber and matrix properties, respectively. This superscript convention is applied throughout the paper. The subscripts used in equations (2.1.1) and (2.2.2), and throughout this section, refer to the principal material coordinates of Figure 4.

Unfortunately, most fibers such as graphite are not isotropic, but are orthotropic. Graphite fibers are often considered to be transversely isotropic (i.e. the plane of isotropy is perpendicular to the longitudinal axis of the fiber). A further discussion of the implications of fiber orthotropy will be given in **Section 5.1**. Strife and Prewo[16] have used a simple modification of equation (2.1.2) by replacing the isotropic fiber CTE, α_1^f, with the transverse fiber CTE, α_2^f, to account for transversely isotropic fibers. This modified expression is written as

$$\alpha_2 = (1 + \nu^m)\alpha^m V^m + (1 + \nu_{12}^f)\alpha_2^f V^f - \alpha_1 \nu_{12} \tag{2.1.3}$$

However, the authors note that the modification is not based on any mathematical derivation. Comparisons between experimental data for unidirectional Kevlar/epoxy and predicted values from equations (2.1.1) and (2.1.3) have been reported by Strife and Prewo[16]. A simple rule-of-mixtures

formula written as

$$\nu_{12} = \nu_{12}^f V^f + \nu^m V^m \qquad (2.1.4)$$

was used for the effective longitudinal Poisson's ratio of the composite needed in equation (2.1.3). The agreement between experimental and predicted values of α_1 was very poor. The authors attributed the poor agreement to inaccurate input values of α_1^f. The predicted values of α_2 were within 15 percent of the measured values.

Chamberlain[17] used the plane stress solution of a thick walled cylinder to derive simple expressions for α_1 and α_2 of a transversely isotropic fiber embedded in a cylindrical isotropic matrix region. The expression for α_1 is identical to equation (2.1.1). The expression for α_2 takes the form

$$\alpha_2 = \alpha^m + \frac{2(\alpha_2^f - \alpha^m)V^f}{\nu^m(F - 1 + V^m) + (F + V^f) + (E^m/E_1^f)(1 - \nu_{12}^f)(F - 1 + V^m)} \qquad (2.1.5)$$

where F is a packing factor which accounts for fiber packing geometry, and is equal to 0.9069 and 0.7854 for hexagonal and square packing geometries, respectively.

Rogers et al[18] used equations (2.1.1) and (2.1.5) to predict the CTE's of unidirectional graphite/ epoxy composites, and compared the predicted values with measured values. The predicted values were within 2 percent of the measured vaules of α_2, using the hexagonal packing factor. The α_1 predictions, in absolute terms, were within $0.03 \times 10^{-6}/°F$ of the measured values. Strife and Prewo[16] also used equation (2.1.5) to predict α_2 for Kevlar/epoxy, and reported differences of about 13 percent from the measured values.

Chamis[19] used a simple force-balance, or strength-of- materials approach, to derive expressions

for the CTE's of unidirectional composites consisting of transversly isotropic fibers in an isotropic

matrix. The expression for α_1 is again identical to equation (2.1.1). The expression for α_2 can be

written as

$$\alpha_2 = \alpha_2^f V^f + \alpha^m V^m (1 + V^f \nu^m E_1^f / E_1) \tag{2.1.6}$$

where E_1 is the longitudinal Young's modulus of the composite, given by the simple rule-of-mixtures

formula written as

$$E_1 = E_1^f V^f + E^m V^m \tag{2.1.7}$$

No comparisons between measured and predicted values using equation (2.1.6) could be found

in the literature. However, a comparison between equation (2.1.6) and a finite element analysis

showed very poor agreement[20].

Rosen and Hashin[21] extended the work of Levin[22] to derive expressions for the effective CTE's

of multiphase composites. Hashin[23] summarized this approach for unidirectional fiber reinforced

composites with transversly isotropic constituents. This analysis is the most general of the anal-

yses discussed thus far, and relates the volume average stresses and strains in a characteristic

volume element to the effective properties of that element. The derivation leads to complicated

tensor expressions for α_1 and α_2, and requires three of the effective elastic mechanical properties

(longitudinal modulus and Poisson's ratio, and transverse bulk modulus) of the composite in the

calculations. In contrast, the Shapery analysis requires only the effective longitudinal Poisson's

ratio, the Chamis analysis requires only the effective longitudinal modulus, and the Chamberlain

analysis requires none of the effective elastic mechanical properties. The general form of the results may be written in tensor notation as[23]

$$\bar{\alpha}_{ij} = \hat{\alpha}_{ij} + (\alpha_{ij}^{(f)} - \alpha_{ij}^{(m)})P_{klrs}(\bar{S}_{rsij} - \hat{S}_{rsij}) \tag{2.1.8}$$

$$P_{klrs}(S_{rsij}^{(f)} - S_{rsij}^{(m)}) = I_{klij} \tag{2.1.9}$$

where S_{rsij} are the elastic compliances and I_{klij} is a fourth rank symmetric unit tensor. Superscripts (f) and (m) refer to fiber and matrix, respectively, are enclosed in parentheses to distinguish them from tensor indices. The terms with an overbar and hat refer to effective and volume average composite properties, respectively. Composite volume average properties are obtained by

$$\hat{p} = V^f p^f + V^m p^m \tag{2.1.10}$$

where p is the property of interest.

For transversely isotropic constituents, equation (2.1.8) simplifies to

$$\alpha_1 = \hat{\alpha}_1 + (\alpha_{kl}^{(f)} - \alpha_{kl}^{(m)})P_{klrs}(\bar{S}_{rs11} - \hat{S}_{rs11}) \tag{2.1.11a}$$

$$\alpha_2 = \hat{\alpha}_2 + (\alpha_{kl}^{(f)} - \alpha_{kl}^{(m)})P_{klrs}(\bar{S}_{rs22} - \hat{S}_{rs22}) \tag{2.1.11b}$$

The overbar has been dropped from α_1 and α_2 to be consistent with equations (2.1.1)-(2.1.7). Equations (2.1.11a) and (2.1.11b) are solved by determining P_{klrs} from equation (2.1.9). The

components of S are obtained from expressions for the effective mechanical properties given by Hashin[23]. Equations (2.1.11a) and (2.1.11b) were expanded and simplified to a form more suitable for routine computations in **Appendix A**. To the author's best knowledge, this is the first time that a fully expanded version of equations (2.1.11a) and (2.1.11b) has appeared in the open literature. No comparisons between measured and predicted values using equations (2.1.11a) and (2.1.11b) could be found in the literature. This may be partly due to the complexity of the expressions relative to some of the other previously discussed derivations.

Exact methods employing the assumption of a regular periodic array of fibers, from which a repeating unit cell may be extracted, have also been used to predict CTE's. A discussion of these methods will be given in the section on stress analysis formulations.

As described above, numerous expressions have been derived, with varying degrees of complexity, for explicitly computing the effective CTE's of unidirectional composites, based on the elastic properties and CTE's of the constituents. However, a systematic comparison of these different formulations with each other, and with a broad range of experimental data has not been reported. This type of comparative study is essential for determining the applicability of each formulation, and will be one of the major thrusts of this dissertation.

2.2 Thermal Stress Analysis

The prediction of thermally induced damage and comparisons with experimental data have, for the most part, been limited to the macro or laminate level[9-10]. However, numerous papers have been published on predicting the mechanical stress-strain behavior of unidirectional composites using micromechanics analyses. The three most common approaches fit into the three categories listed in **Section 2.1** as exact, self consistent, and strength of materials formulations. Representative papers from all three categories are discussed below.

Exact formulations usually assume that the fibers occur in a regular periodic array. This allows the analyses to be performed on a repeating unit cell rather than the whole array of fibers, thus greatly reducing the size and complexity of the problem. The influence of adjacent fibers is incorporated through the boundary conditions on the unit cell. Many of the exact formulations have employed the finite element method. Adams et. al.[24-27] have published extensively in this area using a generalized plane strain formulation, with constant strain triangular (CST) elements, to model circular fibers in a square array surrounded by matrix material. This analysis was used to examine the effects of matrix material nonlinearity and temperature dependence on graphite/epoxy composite stress- strain behavior for various load conditions. All of the thermal load conditions were for room temperature and above. Foye[28] and Dvorak et. al.[29] have also used finite element analyses with CST elements to predict nonlinear stress-strain behavior of unidirectional composites subjected to thermomechanical loading. These papers were primarily aimed at predicting matrix yielding in metal matrix composites subjected to mechanical loading.

Aboudi[30-32] has also used an exact formulation. The Aboudi model assumes a triply periodic array of parallelepiped fibers embedded in an infinite matrix region. The representative cell for this model is a single parallelepiped fiber subcell surounded by three parallelepiped matrix subcells. This general geometry can be used to model particulate reinforcements, short fibers, continuous fibers, and 3D woven fabrics. A first order displacement expansion is employed in each subcell, which leads to average constant stresses and strains in each subcell. Imposition of continuity of tractions and displacements across the boundaries of the individual subcells leads to closed form expressions relating the applied stress to the average stresses and strains in each subcell. This model has had very good success in predicting the global effective properties and stress-strain behavior of metal matrix composites[33]. However, the assumption of parallelepiped fibers, and constant subcell stresses and strains, raises concerns about the accuracy of this model for predicting the local stress fields in the vicinity of the fibers.

Several stress analyses have been formulated using variations of the self- consistent model. All of the self-consistent models assume that the real composite can be replaced by a representative cell embedded in a homogeneous medium whose properties are equivalent to the effective properties of the composite. These models neglect certain microstructural details, such as the influence of adjacent fibers, and are usually best suited for prediction of global behavior. One of the most widely used self-consistent models is the composite cylinder assemblage (CCA) formulation of Hashin[34]. The representaive cell in this formulation is a composite cylinder (i.e circular fiber embedded in a cylindrical region of matrix) and can be solved as an elasticity boundary value problem. A thorough description of this formulation will be given in **Section 3.3.2**. Avery and Herakovich[35] have used this method to examine the effects of fiber anisotropy on the thermomechanical stresses in unidirectional composites. Mikata and Taya[36] have also used this method to examine the effects of fiber coatings on thermomechanical stresses. Both of these analyses were linear elastic with temperature independent material properties, and did not consider thermal loads below room temperature or the initiation of thermally induced damage.

Another variation of the self-consistent model is the "solid mixture" formulation of Min[37]. This is a plane stress elastic-plastic analysis with uniform stresses in the fiber and matrix phases. This analysis was used to study the elastic-plastic mechanical response of metal matrix composites. Dvorak et. al[38] have derived a "vanishing fiber diameter" formulation which is also a variation of the self-consistent model. The composite is modeled as a continuum reinforced by cylindrical fibers of vanishingly small diameters that occupy a finite volume fraction of the composite. This leads to uniform local stress and strain fields in the constituents, but greatly simplifies the computation of the global composite stress-strain behavior. The authors do state that this formulation neglects certain interactions between phases in the transverse direction, and therefore has questionable accuracy for predicting composite response in that direction. This analysis was also used to study the elastic-plastic mechanical behavior of metal matrix composites.

Chamis[39] has used a strength of materials approach to derive simple expressions for fiber and matrix stresses using constituent properties, effective unidirectional lamina properties, and applied lamina stresses. Fiber stresses are assumed to be uniform, and there are two regions of uniform matrix stresses. This formulation is consistent with the formulation given by Chamis[19] for predicting effective properties.

Analyses that fall under the category of exact, as described at the beginning of this section, give more accurate descriptions of the local variations in the stress and strain fields of the constituents by virtue of their formulation. Analyses based on variations of the self-consistent model have been shown to be well suited for predicting global properties and response, but lack the microstructural details to predict localized phenomenon. If the unidirectional composite response is needed as input to a laminate model, then a global response might be adequate and even desirable due to its usually simpler computational scheme. However, accurate predictions of thermally induced damage require detailed information about local variations in the stress field, and thus require analyses that fall within the exact category. None of the micromechanics studies found in the literature, and described above, investigated the initiation of thermally induced damage in polymer matrix composites. An analytical investigation of this problem will be one of the main thrusts of this study. The results of an exact formulation based on a finite element analysis will be compared to a self-consistent scheme based on the composite cylinder model.

3.0 Theoretical Development

3.1 Approach

The theoretical thrust of this dissertation is divided into two areas. The first deals with the prediction of effective CTE's of unidirectional composites. Four formulations for explicitly predicting effective CTE's were presented in **Section 2.1**, and a discussion of these formulations will not be repeated in this chapter. Those expressions assumed temperature independent constituent properties. A method for correctly incorporating the effects of temperature dependent constituent properties will be developed and presented in this chapter.

The second area of theoretical investigation deals with the prediction of thermally induced stresses in the constituents of unidirectional composites. Two formulations will be presented in this chapter; a finite element analysis, and an elasticity solution of the composite cylinder problem discussed in **Section 2.2**. These two formulations will be presented for temperature independent constituent properties first. A general method for incorporating the effects of temperature dependent constituents will then be presented. A brief discussion on the use of classical laminated plate theory (LPT) for predicting laminate thermal response, and a simple global/local formulation combining LPT with micromechanics will also be presented.

The general problem geometry under consideration was shown in Figure 4. The assumptions that are common to all of the theoretical work of this study are listed below.

1. The fibers are circular in cross-section and infinitely long in the 1-direction.

2. All of the constituents are linear elastic.

3. The displacements are continuous across the fiber/matrix interface.

4. The temperature distribution is uniform throughout the body.

These assumptions are the same as those used in the derivations for predicting effective CTE's discussed in **Section 2.1**, with the exception that the constituent properties may now be functions of temperature.

3.2 Effective Coefficients of Thermal Expansion

The expressions for predicting effective CTE's presented in **Section 2.1** were derived assuming temperature independent constituent properties. If the constituent properties vary with temperature the expressions are no longer valid, and must be modified. The appropriate modification consists of replacing all of the α's (effective, fiber, and matrix) with thermal strains, ϵ, given by

$$\epsilon(T) = \int_{T_{SFT}}^{T_1} \alpha(\tau) d\tau \tag{3.2.1}$$

where T_{SFT} and T_1 are the stress free temperature and analysis temperature, respectively. The T_{SFT} is usually assumed to be the temperature at which the composite is fabricated, and as the name implies, is the temperature where the composite and its constituents are all stress free.

Conversely, by definition α is given by

$$\alpha(T) = \frac{d\epsilon(T)}{dT} \tag{3.2.2}$$

Therefore, the instantaneous effective CTE of the composite at T_1 is obtained from the derivative of the expression for the effective thermal strain of the composite evaluated at T_1.

The above procedure is best illustrated by considering a specific example. The expression for the effective longitudinal thermal strain is obtained from equation 2.1.1 and may be written as

$$\epsilon_1 = \frac{E_1^f \epsilon_1^f V^f + E^m \epsilon^m V^m}{E_1^f V^f + E^m V^m} \tag{3.2.3}$$

where all of the constituent properties may now be functions of temperature.

The effective longitudinal CTE is now computed from equation (3.2.2) and is written as

$$\alpha_1 = \frac{d}{dT} \left(\frac{E_1^f \epsilon_1^f V^f + E^m \epsilon^m V^m}{E_1^f V^f + E^m V^m} \right) \tag{3.2.4}$$

Now, if the moduli, E_1^f and E^m, are not functions of temperature, then equation (3.2.4) simplifies to the form of equation (2.1.1), written as

$$\alpha_1 = \frac{E_1^f \alpha_1^f V^f + E^m \alpha^m V^m}{E_1^f V^f + E^m V^m} \tag{3.2.5}$$

where α_1^f and α^m are the CTE's of the constituents evaluated at the temperature of interest, T_1. However, if the constituent moduli are functions of temperature, then equation (3.2.4) becomes

$$\alpha_1 = \frac{1}{E_1^f V^f + E^m V^m} \left(E_1^f V^f \alpha_1^f + E^m V^m \alpha^m + \epsilon_1^f V^f \frac{dE_1^f}{dT} + \epsilon^m V^m \frac{dE^m}{dT} \right)$$

$$- \left(\frac{1}{E_1^f V^f + E^m V^m} \right)^2 \left[\left(E_1^f V^f \epsilon_1^f + E^m V^m \epsilon^m \right) \left(V^f \frac{dE_1^f}{dT} + V^m \frac{dE^m}{dT} \right) \right] \tag{3.2.6}$$

Equation (3.2.6) is rather lengthy, and its evaluation at a particular temperature may be very cumbersome. This is especially true if the functional form of the constituent property variation with temperature is not known. The development of explicit expressions for the temperature dependent transverse CTE becomes even more lengthy and complicated.

An alternate approach to determining explicit expressions for the temperature dependent effective CTE's, as outlined above, is to first compute effective thermal strains, and then numerically evaluate the derivative of equation (3.2.2). The effective thermal strains are computed by substituting the constituent thermal strains (defined by equation (3.2.1)) for the constituent CTE's into the expressions presented in **Section 2.1**. An example of this substitution was shown in equation (3.2.3). This computation requires that the constituent elastic properties be known only at the analysis temperature. The functional form of their variation with temperature is not required. However, the path dependence of the constituent CTE's with temperature is required for evaluation of equation (3.2.1).

The numerical approach used in this study for evaluating equation (3.2.2) was to fit a second order interpolating polynomial to three discrete effective thermal strain values. The three temperatures selected were the analysis temperature, T_1, and temperatures $T_1 \pm 5\,°F$. The expression for the derivative of the effective thermal strain evaluated at T_1 may then be written as[40]

$$\alpha = \frac{d\epsilon}{dT} = \frac{1}{10}\left(\epsilon(T_1 + 5) - \epsilon(T_1 - 5)\right)$$

(3.2.7)

The above expression was used for both the longitudinal and transverse CTE's at each temperature of interest.

3.3 Thermal Stress Analysis

3.3.1 Finite Element Model

A finite element (FE) model was used to determine the thermally induced stresses and deformations in unidirectional composites. The FE analysis of the unidirectional composite geometry, shown earlier in Figure 4, was greatly simplified by assuming the fibers are arranged in some type of regular and periodic array. This allows the analysis to be performed on a representative unit cell rather than the entire composite, and greatly reduces the size and complexity of the analysis. Additional simplifications to the unit cell can be obtained by utilizing the symmetry of its geometry and applied loads. The two fiber array geometries assumed for this study were square and hexagonal. The simplified unit cells, boundary conditions for a uniform thermal load, and coordinate systems for these two array geometries are shown in Figure 5. The (1,2,3) principal material coordinates of Figure 4 are coincident with the (x,y,z) cartesian coordinates of Figure 5.

A condition of generalized plane strain was assumed to exist in the composite. The displacement field for this condition may be written as

$$u = U(y, z) + \epsilon_x^o \cdot x$$

$$v = V(y, z) \tag{3.3.1.1}$$

$$w = W(y, z)$$

where U, V, and W are unknown functions of the spatial coordinates y and z, and ϵ_x^o is a uniform strain (i.e. constant in the yz plane) in the x coordinate direction. The term ϵ_x^o may be a known applied strain or treated as an unknown for a uniformly applied force, F_x^o in the x direction. For thermal loading only, the uniform axial applied force is zero and ϵ_x^o is the unkown thermal strain in the x direction.
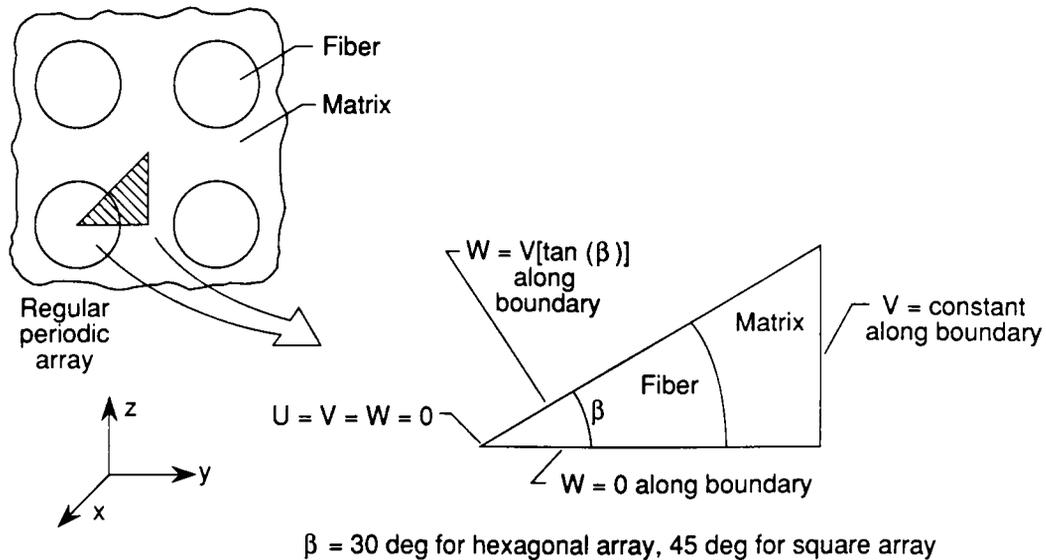
Figure 5. Finite element micromechanics model geometry and boundary conditions.

A linear elastic displacement formulation was used to solve for the above unknowns, using eight node isoparametric quadratic elements. The FE mesh used in this study is shown in Figure 6. This final mesh geometry was derived from a mesh refinement study to determine the minimum number of degrees of freedom (DOF's) that would provide convergence of the solution for the displacements. Details of displacement based FE formulations are found readily in the literature[41]. A description of the formulation is given in **Appendix B**. This description covers the solution for the nodal displacements as well as the computation of the element stresses and strains from these displacements.

Several unique features, specifically required for this study, were incorporated into the formulation presented in **Appendix B**. First, the inclusion of an unkown ϵ_x^0 is carried throughout the formulation, and its effect on the global system of equations is highlighted. A detailed treatment of this type could not be found in the literature. A method to account for material cylindrical orthotropy is also included in the formulation. This type of orthotropy caused the material stiffness matrix to vary

8-node quadratic isoparametric elements
158 nodes, 45 elements

Fiber/matrix interface ⎯
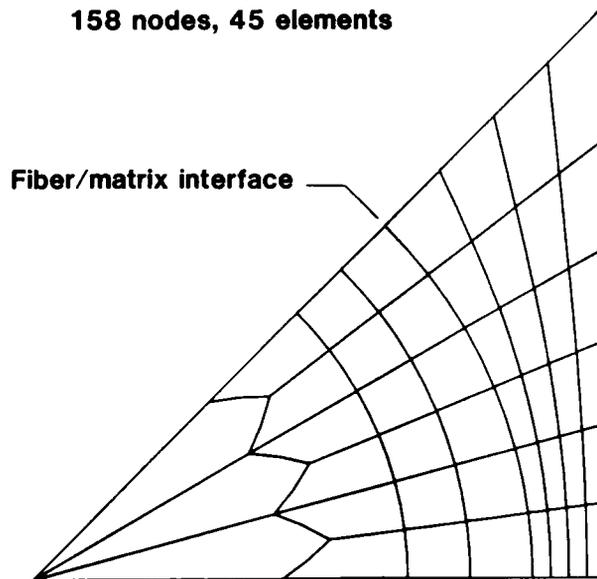
Figure 6. Micromechanics finite element mesh.

within a given element. The variation was included in the formulation by evaluating the stiffness matrix at each of the integration points used in the numerical integration scheme for an element. Finally, a special solution algorithm was developed for efficiently sloving the global system of linear equations for the case of an unknown ϵ_x^o. This was necessary because the inclusion of an unkown ϵ_x^o destroys the bandedness of the global system of equations. The specially developed algorithm allowed the banded nature of the system to be retained, thus greatly increasing solution efficiency.

The formulation described above and in **Appendix B** was implemented in a computer program called FECAP (Finite Element Composite Analysis Program),and was written to run interactively on a desktop microcomputer[11]. FECAP was written in Hewlett Packard BASIC 3.0, and can run on any Hewlett Packard 9000 Series microcomputer with a BASIC 3.0 or compatible operating system. Nodal coordinate and element connectivity data are read from a user generated file. A very simple mesh generation program was written to produce the data files used in this study. The output from FECAP (i.e displacements, stresses, and strains) was written to a file for further post-processing

and plotting.

3.3.2 Composite Cylinder Model

The other analysis used for predicting thermally induced stress fields was the solution to the composite cylinder (CC) boundary-value problem. The CC model, which consists of a circular fiber embedded in a cylindrical region of matrix, is shown in Figure 7, along with the coordinate system and boundary conditions. The use of the CC model for providing the solution to a composite consisting of many fibers (Figure 4) is based on the composite cylinder assemblage (CCA) formulation of Hashin[30]. This formulation, a variation of the self-consistent approach, assumes that a composite can be modeled as a collection of composite cylinders of varying size, all of which have the same ratio of fiber radius to matrix radius (i.e fiber volume fraction). A single composite cylinder becomes representative of the entire composite by requiring that, for a given load state, the stored strain energy in this single composite cylinder is equal to the strain energy in a cylinder of homogeneous material with the same "effective" thermoelastic properties. Consequently, the stresses and strains in a single composite cylinder represent only the average stresses and strains in the "real" composite.

The CC model is most easily solved using the cylindrical coordinate system shown in Figure 7. The terms u, v, and w in the following formulation refer to displacements in the x, θ, and r directions, respectively. Due to the axial symmetry of the geometry and load, for a uniform change in temperature, the v displacement will be zero and the solution will be axisymmetric (i.e independent of the θ coordinate). Conditions of generalized plane strain may also be assumed for this problem, leading to a displacement field which has the functional form of

$$u = u(r) + \epsilon_x^0 \cdot x$$

$$v = 0 \qquad\qquad (3.3.2.1)$$

$$w = w(r)$$
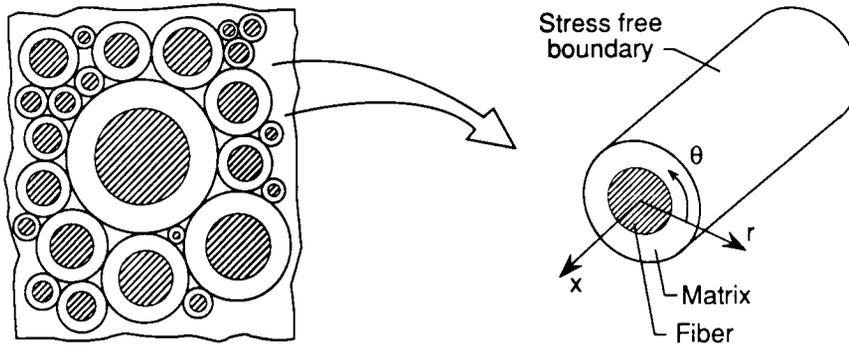
Figure 7. Composite cylinder model geometry and boundary conditions.

where u(r) and w(r) represent the functional form of the u and v displacements, respectively, and ϵ_x^o is an unknown uniform strain in the x direction. The strain-displacement relations can be written as

$$\epsilon_x = \frac{\partial u}{\partial x}, \quad \epsilon_r = \frac{\partial w}{\partial r}, \quad \epsilon_\theta = \frac{w}{r},$$

$$\gamma_{r\theta} = 0, \quad \gamma_{\theta x} = 0, \quad \gamma_{xr} = \frac{\partial u}{\partial r} \tag{3.3.2.2}$$

The nonvanishing equilibrium equations for this problem are

$$\frac{\partial \sigma_r}{\partial r} + \frac{1}{r}(\sigma_r - \sigma_\theta) = 0 \tag{3.3.2.3}$$

$$\frac{\partial \tau_{xr}}{\partial r} + \frac{\tau_{xr}}{r} = 0 \tag{3.3.2.4}$$

Substituting the strain-displacement relations (equation (3.3.2.2)) into the appropriate material constitutive relations, and then substituting the resulting relations into equation (3.3.2.3) yields the

governing differential equation for the w displacement written as

$$C_{rr}\left[\frac{\partial^2 w}{\partial r^2} + \frac{1}{r}\frac{\partial w}{\partial r}\right] - C_{\theta\theta}\frac{w}{r^2} = \frac{1}{r}(C_{\theta x} - C_{rx})\epsilon_x^0 + \frac{1}{r}(C_{ri} - C_{\theta i})\alpha_i \Delta T \tag{3.3.2.5}$$

where the C_{ij} and α_i are the stiffness and CTE coefficients, respectively, and are defined in **Appendix D**. The repeated subscript i in equation (3.3.2.5) is summed over x, r, and θ. The general solution to equation (3.3.2.5) has been given by Cohen and Hyer[42] for an orthotropic tube, and by Avery and Herakovich[31] for a fiber/matrix composite, and is repeated in **Appendix D** for completeness.

The solution of equation (3.3.2.4) may be written down by inspection as

$$\tau_{xr} = \frac{K}{r} \tag{3.3.2.6}$$

where K is a constant that can be determined form the boundary condition on τ_{xr} at the outer surface of the cylinder. For thermal loading only, the outer surface is stress free and therefore K must equal zero. This implies that there are no shear stresses or strains for the case of thermal loading only. Also, the functional form of u given in equation (3.3.2.1) may be simplified to

$$u = \epsilon_x^0 \cdot x \tag{3.3.2.7}$$

where the displacement u is no longer a function of r.

The solution to equation (3.3.2.5) and the subsequent expressions for the stresses in the fiber and matrix presented in **Appendix D** were coded into a computer program for ease of computation. This program was also written to run on a Hewlett Packard 9000 Series microcomputer.

3.3.3 Global/Local Model

The boundary conditions for the FE model shown in Figure 5 are for a unidirectional composite with no externally applied loads except for a uniform change in temperature. These boundary conditions must be modified to model an array of fibers and matrix in a laminated composite, in order to account for the constraints imposed on the individual laminae. These constraints arise from the mismatch in CTE (α_1 and α_2) between plies with different fiber orientations when the laminate is subjected to change in temperature. The theory governing this behavior in thin laminates, where conditions of plane stress may be assumed, is known as laminated plate theory (LPT) and is found readily in the literature [43]. In a symmetric laminate subjected to a uniform change in temperature the strains in each ply are equal, and may be written as

$$\left\{ \begin{array}{c} \epsilon_x^0 \\ \epsilon_y^0 \\ \gamma_{xy}^0 \end{array} \right\} = [A]^{-1} \left(\sum_{k=1}^{n} [\bar{Q}]_k \{\alpha\}_k t_k \right) \Delta T \tag{3.3.3.1}$$

where $\{\alpha\}_k$ is the CTE matrix of the k'th ply, t_k is the thickness of the k'th ply, and [A] and $[\bar{Q}]_k$ are the stiffness matrices of the laminate and k'th ply, respectively. The summation is over the total number of plies, n. Definitions of the above terms can be found in the LPT reference cited earlier.

The strains in equation (3.3.3.1) are referenced to the (x,y,z) laminate coordinate system shown in Figure 8, and must be transformed to the (1,2,3) principal material coordinate system (Figure 4) for use with the FE analysis. This is accomplished through a simple transformation equation written as

$$\left\{ \begin{array}{c} \epsilon_1 \\ \epsilon_2 \\ \gamma_{12} \end{array} \right\}_k = \begin{bmatrix} \cos^2\theta & \sin^2\theta & \cos\theta\sin\theta \\ \sin^2\theta & \cos^2\theta & -\cos\theta\sin\theta \\ -2\cos\theta\sin\theta & 2\cos\theta\sin\theta & \cos^2\theta - \sin^2\theta \end{bmatrix}_k \left\{ \begin{array}{c} \epsilon_x^0 \\ \epsilon_y^0 \\ \gamma_{xy}^0 \end{array} \right\} \tag{3.3.3.2}$$

where θ is the angle measured from the x-axis to the 1-axis for the k'th ply.

The through-the-thickness (3 or z direction) thermal strain of a given ply is also constrained in a multidirectional laminate. The expression for this strain is derived directly from Hooke's Law, and is written for the k'th ply as[44]

$$\epsilon_3 = \alpha_2 \Delta T - \left(\frac{\nu_{12}}{E_1}\right)\sigma_1 - \left(\frac{\nu_{23}}{E_2}\right)\sigma_2 \tag{3.3.3.3}$$

The above equation assumes that the lamina or ply properties are transversely isotropic (2-3 plane of isotropy). The terms ν_{12} and ν_{23} are the lamina Poisson's ratios, E_1 and E_2 are the lamina moduli, and α_2 is the unconstrained lamina CTE. The terms σ_1 and σ_2 are the thermally induced lamina stresses in the principal material coordinates. These stresses are determined from LPT, and are written as

$$\left\{\begin{array}{c}\sigma_1 \\ \sigma_2 \\ \tau_{12}\end{array}\right\}_k = [T]_k[\bar{Q}]_k(\{\epsilon^o\} - \{\alpha\}_k \Delta T) \tag{3.3.3.4}$$

where $\{\epsilon^o\}$ is defined by equation (3.3.3.1), and $[T]_k$ is a transformation matrix given by

$$[T]_k = \begin{bmatrix} \cos^2\theta & \sin^2\theta & 2\cos\theta\sin\theta \\ \sin^2\theta & \cos^2\theta & -2\cos\theta\sin\theta \\ -\cos\theta\sin\theta & \cos\theta\sin\theta & \cos^2\theta - \sin^2\theta \end{bmatrix}_k \tag{3.3.3.5}$$

The method for imposing the laminate induced constraints on a fiber/matrix unit cell is shown schematically in Figure 8. The thermally induced laminate strains, ϵ_1, ϵ_2, and γ_{12}, and the through-the-thickness lamina strain, ϵ_3, were determined from equations (3.3.3.1) through (3.3.3.5), for a given ΔT, and ply. These strains were then used as displacement boundary conditions on the FE model of a single fiber and surrounding matrix exposed to the same ΔT. The FE model shown
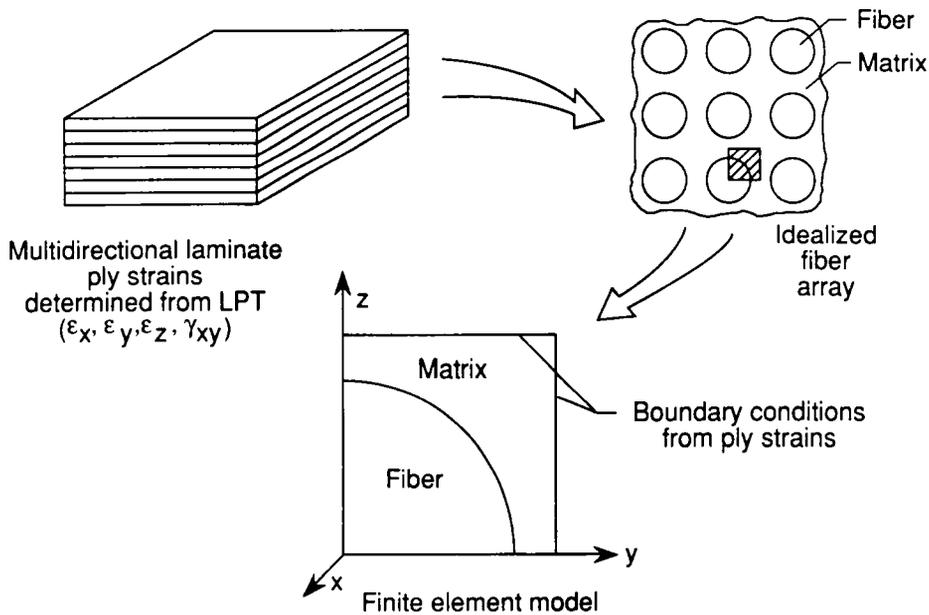
Figure 8. Finite element model for global/local formulation.

in Figure 5 could not be used for this formulation because of a difference in symmetry conditions. Instead, the "quarter-symmetry" model (i.e. modeling of a quarter of a fiber) shown in Figure 8 was used. The axial strain condition was imposed by setting the uniform applied axial strain, ϵ_x^o of equation (3.3.1.1) from the FE formulation, equal to ϵ_1. The transverse strain condition was imposed by setting the V displacement along the $y=1$ edge equal to ϵ_2. The V displacement along $y=0$ was set equal to zero. The shear strain condition was imposed by setting the U displacement along $y=0$ to zero, and the U displacement along $y=1$ to γ_{12}. Finally, the W displacement along $z=0$ was set equal to zero, and the W displacement along $z=1$ was set equal to ϵ_3.

3.3.4 Temperature Dependent Constituents

The CC and FE models described above were presented for the case of temperature independent constituent properties. However, both models were implemented with the capability to allow for temperature dependent constituent material properties. The formulations were modified by follow-

ing the procedure described in **Section 3.2.** Terms containing $\alpha \Delta T$ were replaced with thermal strains given by

$$\epsilon(T) = \int_{T_{SFT}}^{T_1} \alpha(\tau) d\tau \qquad (3.3.4.1)$$

which is identical to equation (3.2.1). The stresses in the constituents may be written in generic form as

$$\{\sigma(T_1)\} = H(T_1) \int_{T_{SFT}}^{T_1} G(\tau) d\tau \qquad (3.3.4.2)$$

where $H(T_1)$ is some function of the constituent elastic properties evaluated at T_1, and $G(\tau)$ is some function of the constituent CTE's.

This formulation is refered to in the literature as a "total strain theory"[45]. As discussed in **Section 3.2**, the elastic moduli and Poisson's ratios are only required at the analysis temperature. Their path dependence with temperature is not required. This formulation is only valid for elastic constituent material properties (i.e. properties not a function of stress). When the properties are inelastic, an incremental approach must be used.

4.0 Experimental Methods

A brief description of the experimental method used to determine the thermal strain behavior of composites will be presented first. This will be followed by a discussion of the method used to observe and characterize thermally induced damage in a high modulus graphite/epoxy composite.

4.1 Measurement of Thermal Strains

Thermal strain data were determined for a number of different continuous fiber reinforced unidirectional composite systems. These data will be presented in **Section 5.2**. All of the measurements were made using a laser interferometric dilatometer at NASA-LaRC. This equipment has a strain resolution of approximately 1×10^{-6} and a temperature range of $-250\,^{\circ}F$ to $+300\,^{\circ}F$. The specimen length is approximately 3 inches, and the strain is determined over the full length of the specimen. All of the resin matrix composites were vacuum dried to a constant mass before testing, and all of the specimens were tested in a dry N_2 environment. Details of the experimental technique are given in the literature[46].

Values of α_1 and α_2 were obtained by fitting a least-squares polynomial (usually 3rd order) to the thermal strain-temperature curves and then evaluating the derivative of this polynomial at the desired temperature. A typical axial thermal strain-temperature curve for unidirectional T300/5208, along with the least-squares polynomial fit, is shown in Figure 9.
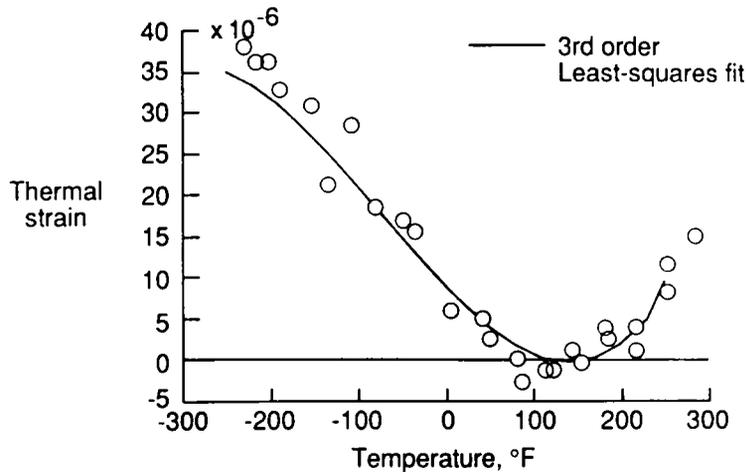
Figure 9. Axial thermal strain curve for unidirectional T300/5208.

4.2 Damage Observation and Characterization

The formation and growth of thermally induced damage was observed and characterized in a high

modulus P75/934 graphite/epoxy composite system. A description of the constituent properties

of this particular system will be given in **Section 5.1**. Unidirectional and cross-ply panels were

fabricated from prepreg tape according to the manufacturer's standard cure cycle. The maximum

temperature in this cure cycle was 350°F , which was the assumed stress-free-temperature in the

thermal stress analysis to be presented in **Section 5.3**. The panels were ultrasonically C-scanned

after fabrication, and exhibited no significant voids or delaminations. Both panels had an average

fiber volume fraction of 0.50.

Specimens from unidirectional and cross-ply laminates were observed after fabrication, and af-

ter various numbers of thermal cycles between ±250°F , for the presence of thermally induced

damage. The observations consisted of examining the polished edges of the specimens with an

optical microscope at magnifications of 400x. The specimen dimensions were 3(L) by 1(W) by 0.04(T) inches. All of the specimens were dried prior to observation and were kept dry throughout the thermal cycling process. The effects of thermal cycling induced damage on the modulus and CTE of these specimens, as well as the details of the experimental procedure, have been reported elsewhere[10]. The present study will focus on the initiation and morphology of the damage observed in these specimens.

5.0 Results and Discussion

The discussion of the analytical results will be divided into four main sections. The first section will discuss the constituent property data that was used as input for all of the analytical predictions. The second section will discuss the various methods for predicting effective CTE's of unidirectional composites, and their comparisons with experimental data. The third section will describe the results of the thermal stress predictions, and the final section will discuss the formation of thermally induced damage.

5.1 Constituent Properties

As discussed in **Section 2.1**, carbon fibers are not isotropic, but are commonly assumed to be transversely isotropic with the plane of isotropy being the 2-3 plane of Figure 4. However, studies[47-51] of carbon fiber morphology suggest that the fibers may posses a combination of a cylindrically orthotropic (i.e different properties in the x, r, and θ directions of Figure 7) sheath near the outer surface of the fiber, and a transversely isotropic core as shown in Figure 10. The type of cylindrical orthotropy (i.e. radial or circumferential) depends upon the fiber fabrication process. Carbon fibers made with a PAN (polyacronitrile) precursor typically have a circumferentially orthotropic sheath and those made from a pitch precursor typically have a radially orthotropic sheath. A thorough investigation of the effects of fiber morphology on composite
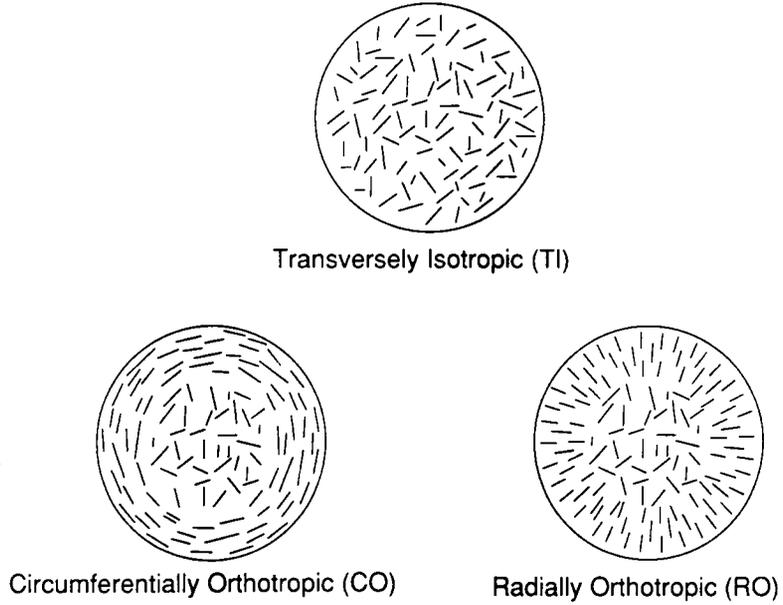
Figure 10. Carbon fiber morphology.

effective properties and stresses has been given by Knott[52]. Specific results from that study will be discussed in subsequent sections.

The majority of results for the present study were generated with the assumption of transversely isotropic fibers. This reduces the number of independent elastic constants for the fiber to five, written as

$$E_1^f, \ E_2^f = E_3^f, \ \nu_{12}^f = \nu_{13}^f, \ \nu_{23}^f, \ G_{12}^f = G_{13}^f \tag{5.1.1}$$

with the transverse shear modulus related to the other properties by

$$G_{23}^f = E_2^f/2(1 + \nu_{23}^f) \tag{5.1.2}$$

All of the matrix materials were assumed to behave isotropically with two independent elastic constants written as

$$E^m, \ \nu^m \tag{5.1.3}$$

and the shear modulus defined by

$$G^m = E^m/2(1 + \nu^m)$$
(5.1.4)

E, ν, and G in the above expressions represent the Young's moduli, Poisson's ratios, and shear moduli, respectively. The subscripts refer to the material coordinates of Figure 4, and the superscripts f and m refer to fiber and matrix, respectively. In addition to the elastic constants, there are two independent CTE's for a transversely isotropic fiber, α_1^f and α_2^f, and one for an isotropic matrix, α^m.

Fiber property data, especially as a function of temperature, are very difficult to find in the literature due to the extreme difficulty of generating these values experimentally. The carbon fiber properties used in the present study were assumed to be temperature independent. This assumption is thought to be valid due to the relatively small temperature range used for the analyses ($-150\,°F$ to $+250\,°F$) compared to the large useful operating temperature range of carbon fibers, and the large distance of the analysis temperature range from the fabrication temperatures of the fibers. The axial CTE of PAN based carbon fibers has been shown to be independent of temperature over this range[53]. The elastic constants and CTE's for the various carbon fibers used in the analyses are given in Table 1. The T300, C6000, and HMS fibers are PAN based, and are manufactured by Amoco, BASF, and Hercules, respectively. P75 and P100 are high modulus pitch based fibers manufactured by Amoco. The data in Table 1 come from various literature sources, including both research papers and manufacturers product data sheets[54-57]. Experimentally measured values from the literature were used when available. However, the transverse fiber properties represent values from the literature that were back-calculated from composite properties using micromechanics theories for predicting effective composite properties[23].

Table 1. Carbon Fiber Properties at 75°F.

Fiber	E_1 (Msi)	E_2 (Msi)	G_{12} (Msi)	$G_{23}^{(1)}$ (Msi)	ν_{12}	ν_{23}	α_1 $(10^{-6}/°F)$	α_2 $(10^{-6}/°F)$
T300	33.8	3.35	1.30	1.20	0.20	0.40	-0.30	5.60
C6000[2]	33.8	3.35	1.30	1.20	0.20	0.40	-0.30	5.60
HMS	55.0	0.90	1.10	0.32	0.20	0.40	-0.55	3.80
P75	79.8	1.38	1.00	0.49	0.20	0.40	-0.75	3.80
P100	115.5	1.05	1.00	0.38	0.20	0.40	-0.78	3.80

(1) $G_{23} = E_2/2(1 + \nu_{23})$

(2) C6000 assumed to have same properties as T300

A wide range of matrix materials was used for the effective CTE predictions. The properties of these materials are listed in Table 2. The elastic and CTE properties for the aluminum and glass matrices were assumed to be temperature independent over the temperature range of interest, and were taken from the literature[58]. The polyimide properties[19] were also assumed to be temperature independent due to a lack of temperature dependent data. The epoxy properties are those of Fiberite Corp. 934, a widely used 350°F cure aerospace epoxy matrix. This was the matrix material used for the majority of the stress analysis predictions. The other epoxies in Table 2 (Narmco 5208, Fiberite 930, and Ferro CE339) were all assumed to have the same room temperature properties as 934, except α^m for CE339 which is a rubber-toughened epoxy and has a higher CTE[27]. The 934 matrix properties were assumed to be temperature dependent. Experimental values of E^m and ν^m, at room temperature (RT) and +250°F, were given by Fox et.al.[59]. The elastic properties at -250°F were back-calculated for this study, from T300/934 unidirectional lamina properties[60] at -250°F using the CCA formulation of Hashin for predicting effective elastic composite proper-ties[23]. The temperature dependent values of α^m for 934 were back-calculated at -250°F, RT, and +250°F from T300/934 unidirectional lamina CTE data, using the Rosen and Hashin analysis discussed in **Appendix A**.

Table 2. Matrix Properties at 75°F .

Matrix	E (Msi)	$G^{(1)}$ (Msi)	ν	α $(10^{-6}/°F)$
934 epoxy[2]	0.67	0.25	0.36	23.0
5208 epoxy[2]	0.67	0.25	0.36	23.0
930 epoxy[2]	0.67	0.25	0.36	23.0
CE339 epoxy[2]	0.67	0.25	0.36	35.2[3]
PMR15 polyimide	0.50	0.19	0.35	20.0
2024 aluminum	10.60	4.00	0.33	12.9
Borosilicate glass	9.10	3.80	0.20	1.8

(1) $G = E/2(1 + \nu)$

(2) All epoxies were assumed to have the same properties unless noted

(3) Value for a similar rubber-toughened epoxy

Second order polynomial representations of the dependence of the 934 properties with temperature are given in Table 3. These polynomials were used in the analyses for computing the matrix properties at discrete temperatures between -150°F and +250°F .

Table 3. Functional Form of Temperature Dependent 934 Epoxy Properties.

$$\text{Property} = A_0 + A_1 T + A_2 T^2, \quad (T = °F)$$

Property	A_0	A_1	A_2
E (Msi)	0.7743×10^0	-0.1422×10^{-2}	0.1123×10^{-5}
G (Msi)	0.2832×10^0	-0.5160×10^{-3}	0.4448×10^{-6}
ν	0.3677×10^0	-0.4400×10^{-4}	-0.2514×10^{-6}
α $(10^{-6}/°F)$	0.1975×10^2	0.4500×10^{-1}	-0.1700×10^{-4}

5.2 Effective Coefficients of Thermal Expansion

Predictions of effective CTE's from the four explicit formulations presented in **Section 2.1**, and from the finite element analysis, developed for this study and presented in **Section 3.1.1**, will be

compared with each other and with experimental data. These five analyses will be referred to by the following abbreviations: Shapery (SH), Chamberlain (CB), Chamis (CH), Rosen and Hashin (RH), and finite element (FE). The Hex and Sq designations for the CB and FE predictions refer to hexagonal and square fiber arrays.

The specific material systems examined are given in Table 4, along with their experimentally determined values of α_1 and α_2 at RT. Some of these values were measured specifically for this study, while others were taken from previous studies[61-62]. All of the data were obtained from the interferometric dilatometer system described in **Section 4.1**. These material systems have axial fiber to matrix stiffness ratios of E_1^f/E^m ranging from 6 to 140, and axial fiber to matrix CTE ratios of α_1^f/α^m ranging from -0.01 to -0.30, and thus cover a wide range of fiber/matrix combinations. The RT fiber and matrix properties needed as input to the analyses were given in Tables 2 and 3.

Predictions and comparisons with experimental data for the axial CTE will be discussed first, followed by a discussion of transverse CTE predictions and comparisons. These predictions will assume temperature independent constituent property behavior. The sensitivity of effective CTE's to constituent properties, the effects of temperature dependent constituent properties, and the effects of fiber orthotropy will be discussed in seperate sections.

Table 4. Experimentally Determined CTE Values at 75 °F .

Material System (Fiber/Matrix)	V^f (%)	α_1 ($10^{-6}/$ °F)	α_2 ($10^{-6}/$ °F)
T300/5208	68	-0.063	14.02
T300/934	57	-0.001	16.13
P75/934	48	-0.584	19.18
P75/930	65	-0.598	17.62
P75/CE339	54	-0.567	26.34
C6000/PMR15	63	-0.118	12.46
HMS/Borosilicate	47	-0.230	2.10
P100/2024	40	0.800	14.51

5.2.1 Axial Coefficient of Thermal Expansion

Figures 11-14 show a comparison of α_1 as a function of V^f predicted from the different analyses for four of the material systems: T300/934, P75/934, HMS/Borosilcate, and P100/2024. Experimental data are also shown on these figures. Predicted and measured values of α_1 for all of the materials studied are given in Table 5. The SH, CB, and CH analyses all used equation (2.1.1) for predicting α_1 and are labeled SH in the figures and Table. As shown in the figures, the differences between the RH and FE results were negligible and there were only small differences between these and the SH results. All of the analyses were in good agreement with the experimental data. The largest deviation between any of the predicted and experimental values was only $0.1 \times 10^{-6}/°F$, and in most cases the deviation was on the order of about $0.05 \times 10^{-6}/°F$. Although the magnitudes of α_1 differed for the different material systems, the general response was the same (i.e. decreasing α_1 with increasing V^f). This implies that the relative magnitudes of the fiber/matrix stiffness and CTE ratios did not significantly affect the general trend in α_1 as a function of V^f. This was not true for α_2, as will be discussed subsequently.

Table 5. Comparison of Experimental and Predicted Values of the Axial CTE at 75°F.

| Material System | $\alpha_1 (10^{-6}/°F)$ | | | FE | |
	Exp	SH	RH	Hex	Sq
T300/5208	-0.063	-0.083	-0.051	-0.050	-0.041
T300/934	-0.001	0.045	0.089	0.089	0.093
P75/934	-0.584	-0.535	-0.511	-0.512	-0.511
P75/930	-0.598	-0.642	-0.627	-0.627	-0.623
P75/CE339	-0.567	-0.493	-0.460	-0.461	-0.460
C6000/PMR15	-0.118	-0.125	-0.104	-0.104	-0.099
HMS/Borosilicate	-0.230	-0.180	-0.180	-0.181	-0.181
P100/2024	0.800	0.875	0.907	0.906	0.905
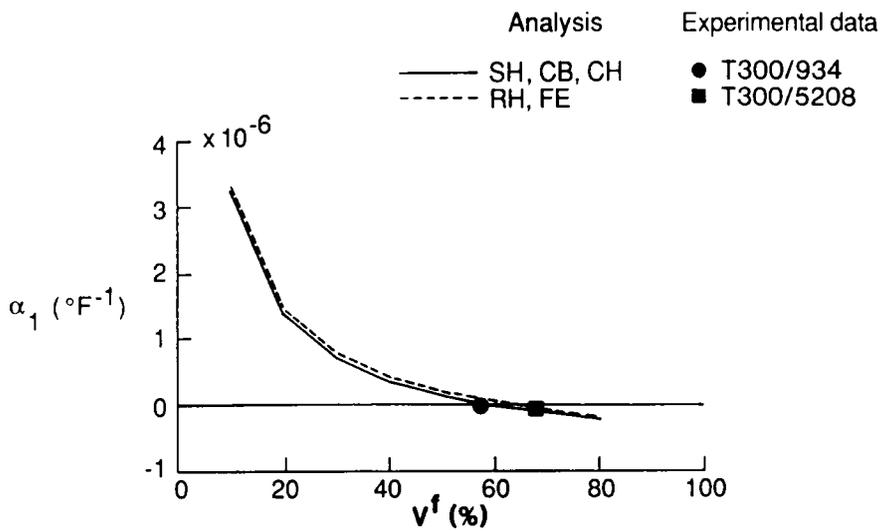
Figure 11. Axial CTE of unidirectional T300/934 and T300/5208.
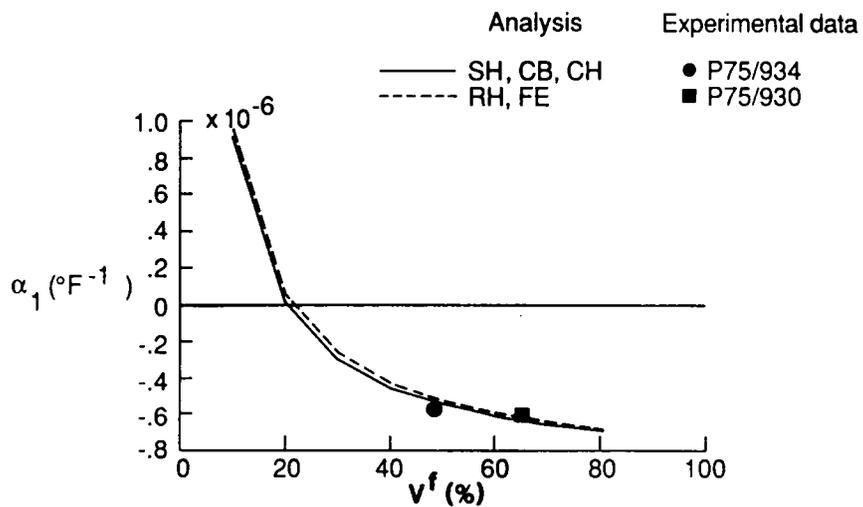
Figure 12. Axial CTE of unidirectional P75/934 and P75/930.
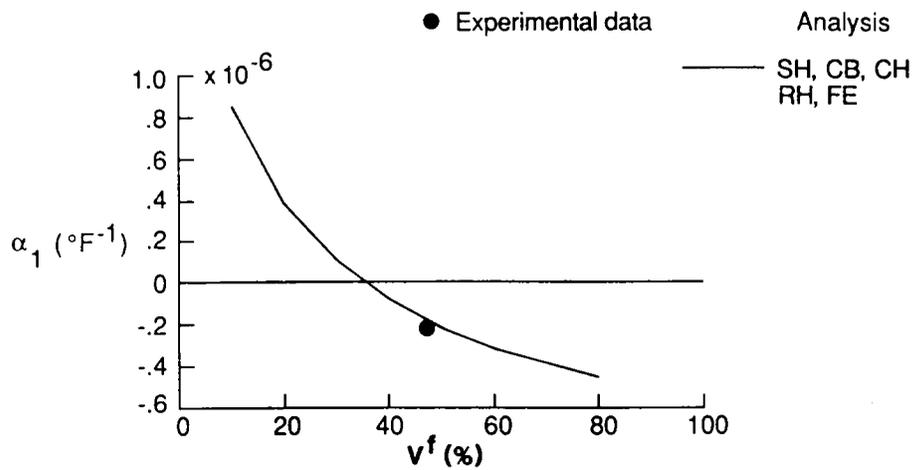
Figure 13. Axial CTE of unidirectional HMS/Borosilicate.
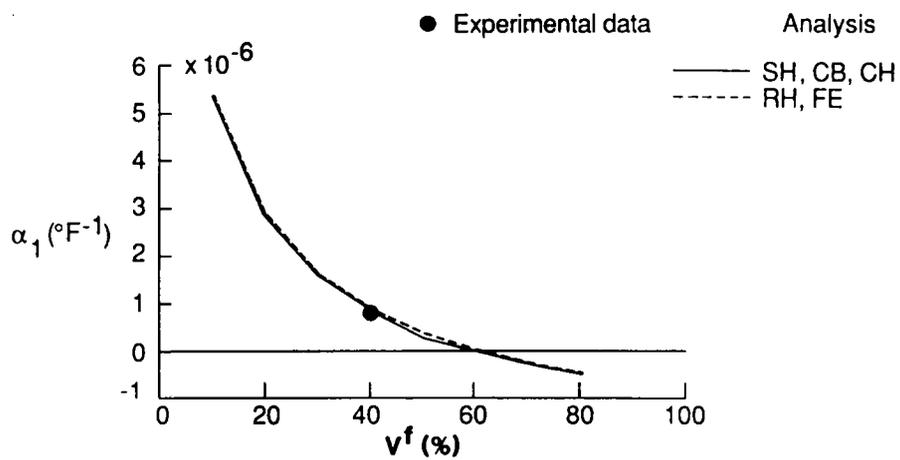
Figure 14. Axial CTE of unidirectional P100/2024.

5.2.2 Transverse Coefficient of Thermal Expansion

Figures 15-18 show the response of α_2 as a function of V^f for the same four material systems shown in figures 10-13. Experimental data are also shown on these figures, as well as in Table 6, where predicted and experimental values are compared for all of the material systems. The SH results were computed with the modified version for transversely isotropic fibers (equation (2.1.3)).

There were large differences between the predicted values of all of the analyses, except for the RH and FE analyses. Results from these two analyses were in excellent agreement with each other, including both array geometries of the FE model. Significant differences between the CH and FE analyses for prediciting α_2 have been previously documented in the literature[20]. These differences were attributed to Poisson restraining effects not included in equation (2.1.6). The neglection of this type of three dimensional effect was also thought to be responsible for the large difference between the CB and FE results. Figures 15-18 and Table 6 also demonstrate that the RH and FE results for α_2 were consistently in much better agreement with the experimental data than were the other analyses. The SH results were in slightly better agreement with the experimental data for the P75/930 and P75/CE339 systems. However, it should be noted that the matrix mechanical properties for these two systems were assumed to be the same as the other epoxy matrices, which is probably not an accurate assumption, and therefore the better agreement with the experimental data is believed to be fortuitous. It should also be remembered that the modification of the SH analysis for transversely isotropic fibers was not based on any mathematical derivation, and was included for comparison purposes only. Agreement between experimental values and RH and FE predicted values were usually within about 15 percent. Predictions from the other analyses differed with the experimental data by as much as 50 percent.
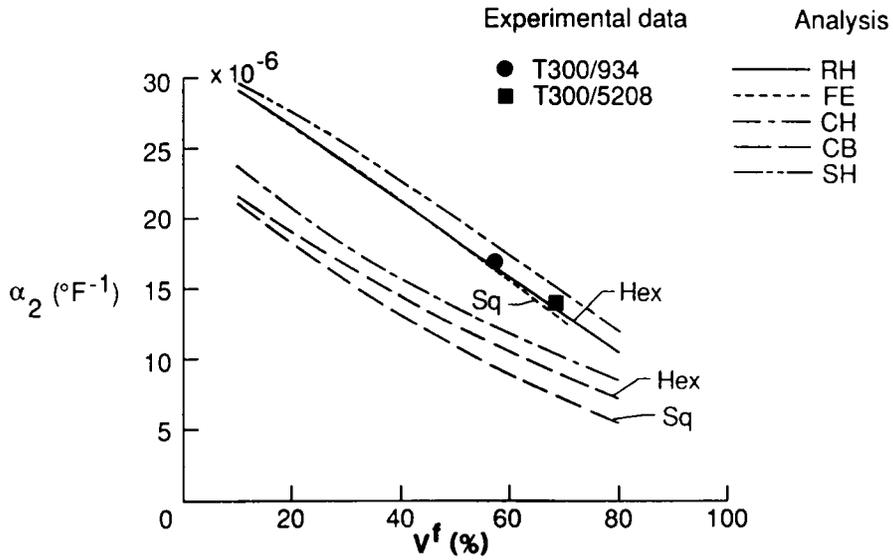
Figure 15. Transverse CTE of unidirectional T300/934 and T30/5208.
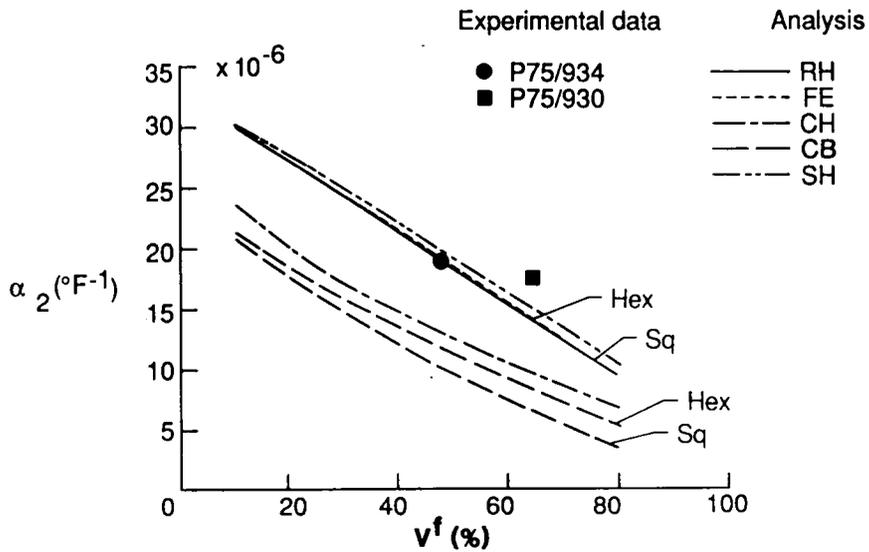
Figure 16. Transverse CTE of unidirectional P75/934 and P75/930.
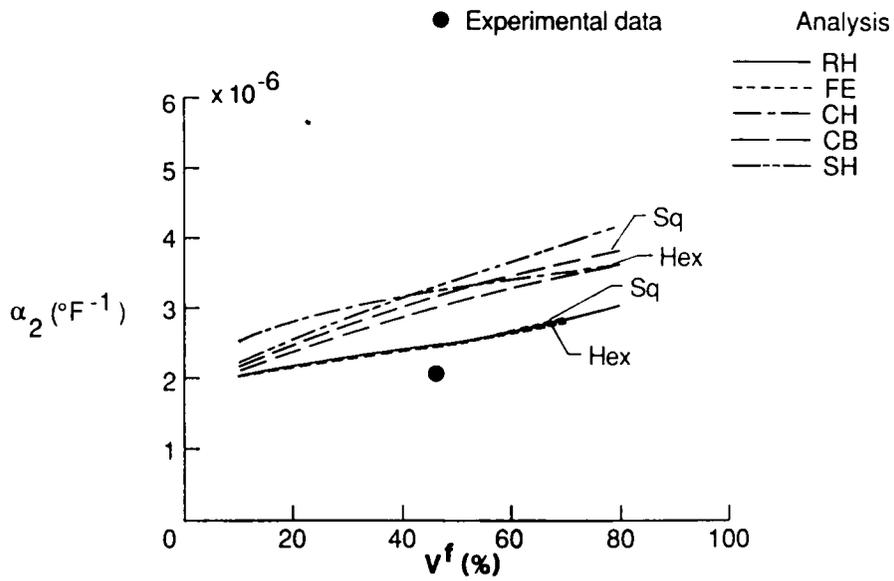
Figure 17. Transverse CTE of unidirectional HMS/Borosilicate.
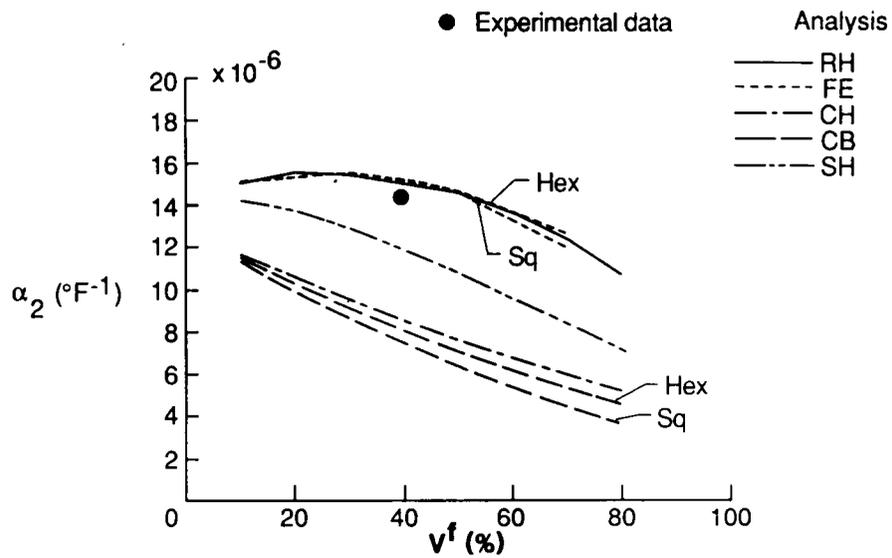
Figure 18. Transverse CTE of unidirectional P100/2024.

Table 6. Comparison of Experimental and Predicted Values of the Transverse CTE at 75°F.

| Material | $\alpha_2(10^{-6}/°F)$ | | | | | | | |
| System | | | CB | | | | FE | |
	Exp	SH	Hex	Sq	CH	RH	Hex	Sq
T300/5208	14.02	14.60	8.85	7.28	10.10	13.00	12.99	12.72
T300/934	16.13	17.30	10.60	9.20	11.90	15.60	15.69	15.59
P75/934	19.18	18.60	11.10	9.63	12.20	17.90	18.05	18.03
P75/930	17.62	14.10	7.89	6.20	9.13	13.20	13.37	13.33
P75/CE339	26.34	24.70	13.80	11.30	15.50	23.60	23.94	23.88
C6000/PMR15	12.46	14.30	8.92	7.67	10.00	12.40	12.56	12.63
HMS/Borosilicate	2.10	3.32	3.04	3.18	3.27	2.49	2.46	2.47
P100/2024	14.51	11.90	8.08	7.47	8.52	15.00	15.15	15.13

Unlike the results for α_1, the response of α_2 as a function of V^f was affected by the fiber/matrix property ratios. T300/934 and P75/934 had similar fiber/matrix property ratios, and exhibited a similar response (Figures 15-16). The P100/2024 system (Figure 18) had CTE fiber/matrix property ratios similar to T300/934 and P75/934, but had much smaller moduli ratios. This difference in moduli ratios resulted in a different response of α_2 as a function of V^f as predicted from the RH and FE analyses (i.e. increasing α_2 with increasing V^f for small values of V^f). The HMS/Borosilicate system (Figure 17) had moduli ratios similar to P100/2024 Al but had much larger CTE property ratios. This difference caused a significantly different response in α_2 as a function of V^f compared to the trends exhibited in Figures 15-16 and 18 (i.e. increasing α_2 with increasing V^f for all values of V^f).

The results presented above and from **Section 5.2.1** show that both simple and rigorous analyses accurately predict the axial CTE of carbon fiber unidirectional composites. These results also demonstrate that plane stress (CB analysis) and strength of materials (CH analysis) formulations do not accurately predict the transverse CTE of these same composites. The more rigorous RH analysis does accurately predict the transverse CTE and can be used in lieu of a detailed FE analysis for such predictions.

5.2.3 Sensitivity to Constituent Properties

As stated earlier, the analytical predictions discussed in the previous section used constituent property data compiled from various literature sources. Some of the values were measured directly, some were back-calculated from composite data, and some were only estimates. A parametric study was conducted using the RH analysis to determine the sensitivity of α_1 and α_2 of P75/934 to the constituent properties. Each of the independent thermoelastic fiber and matrix properties were individually reduced 20 percent, while holding the other properties constant. The resulting changes in α_1 and α_2 are given in Table 7.

As would be expected, α_1 was most sensitive to E_1^f and α_1^f. Fortunately, these are the easiest fiber properties to measure, and therefore usually the most reliable. The prediction of α_1 was insensitive to the transverse fiber properties and matrix properties. The prediction of α_2 was most sensitive to matrix properties. Matrix properties are relatively easy to obtain experimentally, however there are concerns as to whether the chemistry of resin matrices is the same in bulk form as it is in the composite. The sensitivity of α_2 to transverse fiber properties was less than expected. This is again fortunate because transverse fiber properties are the most difficult to obtain, and therefore usually the most unreliable.

The sensitivity analysis presented above demonstrates that the good agreement between the RH and FE analyses and the experimental data was not fortuitous. The constituent properties with the most uncertainty (transverse fiber properties) have only a small effect on the prediction of α_1 and α_2.

The sensitivities of α_1 and α_2 to V^f for all of the material systems studied have been illustrated in Figures 11-18. Predicted values of α_1 were very sensitive to small changes in V^f for values of V^f less than 30 percent. This sensitivity decreased for large values of V^f. The sensitivity of α_2 to V^f is much less, from a percentage standpoint, than that of α_1.

Table 7. Sensitivity Analysis for P75/934 CTE's ($V^f = 0.60$).

20 Percent Reduction in	Percent Change in[1]	
	α_1	α_2
E_1^f	-6.2	-0.6
E_2^f	+0.2	+5.8
G_{12}^f	0.0	0.0
G_{23}^f	0.0	-5.2
ν_{12}^f	-0.7	0.0
α_1^f	-24.9	-0.6
α_2^f	0.0	-3.2
E^m	+5.0	-10.4
ν^m	+1.5	-7.1
α^m	+5.0	-16.9

(1) Calculations based on Rosen and Hashin Analysis

5.2.4 Effects of Temperature Dependent Constituent Properties

As discussed in **Section 5.1**, the 934 epoxy matrix properties are not temperature independent. The method for properly incorporating the effects of temperature dependent constituent properties in the prediction of effective CTE's was described in **Section 3.2**. This method was applied to the RH analysis, and the results will be presented in this section. The RH analysis was selected due to its consistently better agreement with experimental data than the other closed-form analyses, and because of its computational simplicity compared to the FE analysis.

Figures 19-21 show temperature dependent CTE predictions, labeled exact, compared with experimental data for T300/934, T300/5208, and P75/934. Also shown in each figure are predictions from the RH analysis using an approximate method for incorporating temperature dependent matrix properties (i.e. using α^m at temperature T, rather than the $\int_{T_{SFT}}^{T} \alpha^m dT$). The exact analysis predictions were in better agreement with the experimental values of α_2 than the approximate analysis for all three material systems. The excellent agreement between predicted values and experimental data for α_2 of T300/934 (Figure 19) were expected, due to the fact that the T300/934 data was
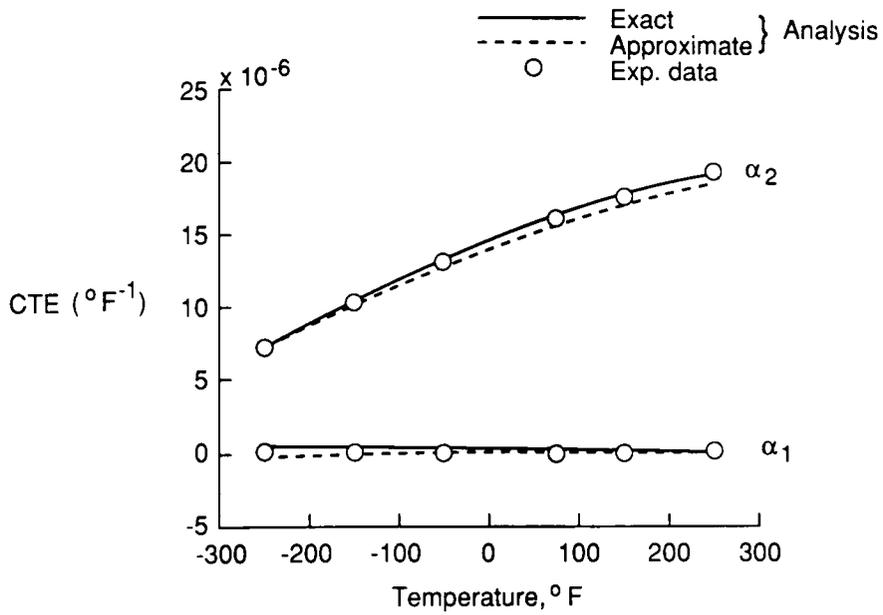
Figure 19. Temperature dependent CTE of unidirectional T300/934 (V^f =0.57).
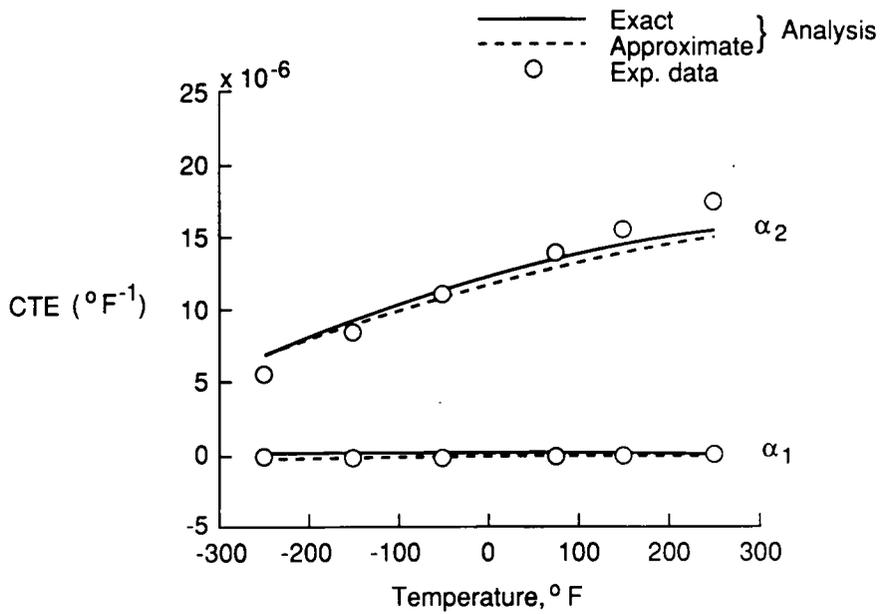
Figure 20. Temperature dependent CTE of unidirectional T300/5208 (V^f =0.68).
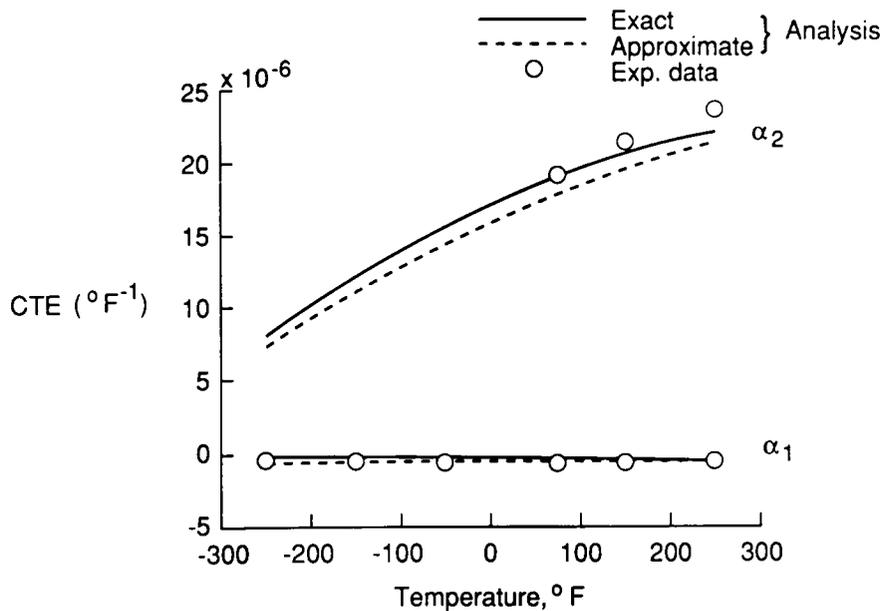
Figure 21. Temperature dependent CTE of unidirectional P75/934 ($V^f = 0.48$).

used to back-calculate the temperature dependent properties of the 934 matrix. These figures do demonstrate the error introduced with the approximate analysis. The agreement between predicted and experimental temperature dependent values of α_1 was also good.

The above results demonstrate that the CTE's of carbon fiber reinforced epoxies do vary with temperature, and accurate predictions of these values require accurate data on the temperature dependence of the constituent properties.

5.2.5 Effects of Fiber Orthotropy

As mentioned previously, Knott[52] conducted an extensive analytical study of the effects of carbon fiber orthotropy on the effective properties and stresses in unidirectional composites, using the CC model discussed in **Section 3.3.2.** The effective CTE's predicted with the assumption of transversely isotropic (TI) fibers were compared to those obtained by assuming two types of

cylindrical fiber orthotropy; circumferential, where $E_\theta > E_r$, and radial, where $E_r > E_\theta$. For transversely isotropic fibers, $E_\theta = E_r$. Large differences in the effective CTE's were predicted for the three types of fiber orthotropy. However, the fiber properties used in that study represent extreme degrees of cylindrical orthotropy. For the circumferentially orthotropic (CO) case E_θ and α_θ were set equal to E_x and α_x, respectively, while E_r and α_r were maintained at their transversely isotropic values. For the radially orthotropic (RO) case E_r and α_r were set equal to E_x and α_x, respectively, while E_θ and α_θ were maintained at their transversely isotropic values. No data in the literature could be found to verify that this degree of cylindrical orthotropy actually exists in carbon fibers. As mentioned earlier, and as pointed out by Knott, the experimental data suggests that carbon fibers contain a transversely isotropic core, and therefore the effective degree of cylindrical orthotropy for the entire fiber would be much less than values described above.

The effects of a less severe degree of cylindrical orthotropy were considered for the present study. The fiber properties for T300 and P75, given earlier in Table 1, were modified according to the relations shown in Table 8 to account for cylindrical orthotropy. The CC model was used to compute the effective CTE's for the three types of fiber orthotropy shown in Table 8. As described in **Section 3.3.2**, this model is formulated on the basis of cylindrical material orthotropy, where transverse isotropy is a special case of the more general condition. The results for the CTE's of T300/934 ($V^f = .57$) are shown in Figure 22, and the results for the CTE's of P75/934 ($V^f = .48$) are shown in Figure 23. Also shown on these figures are predictions from the RH analysis for transversely isotropic fibers. There are two main points demonstrated by these figures. First, the RH analysis and the CC model predict very similar values for the case of transversely isotropic fibers. This implies that the CC model is another formulation, in addtion to the RH and FE discussed in **Sections 5.2.1 and 5.2.2**, that can be used to accurately predict the effective CTE's of unidirectional composites. Secondly, the degree of cylindrical orthotropy shown in Table 8

produces only small differences, in absolute magnitudes, in predicted CTE's compared to the assumption of transversely isotropic fibers.

Table 8. Cylindrically Orthotropic Carbon Fiber Properties.

Property	Circumferential Orthotropy	Radial Orthotropy	Transverse[1] Isotropy
E^f	$E^f_\theta = 2E^f_r$	$E^f_r = 2E^f_\theta$	$E^f_r = E^f_\theta$
G^f	$G^f_{x\theta} = 2G^f_{xr}$	$G^f_{xr} = 2G^f_{x\theta}$	$G^f_{xr} = G^f_{x\theta}$
ν^f	$\nu^f_{x\theta} = .5\nu^f_{xr}$	$\nu^f_{xr} = .5\nu^f_{x\theta}$	$\nu^f_{xr} = \nu^f_{x\theta}$
α^f	$\alpha^f_\theta = .5\alpha^f_r$	$\alpha^f_r = .5\alpha^f_\theta$	$\alpha^f_r = \alpha^f_\theta$

(1) x, r, and θ directions are equivalent to the 1, 2, and 3 directions, respectively.

Based on the above results, carbon fiber transverse isotropy is a reasonable and simplifying assumption for predicting effective CTE's of unidirectional carbon fiber reinforced composites. This is especially true given the lack of quantitative experimental data on fiber mechanical and thermal properties.

5.3 Thermally Induced Stresses

The majority of thermal stress analysis results are presented for P75/934. This is a high modulus composite system with many potential applications on stiffness and dimensionally critical space-craft structures. These results were generated with the composite cylinder (CC) and finite element (FE) models described in **Section 3.3**, and used the fiber properties from Table 1 and the temperature dependent 934 matrix properties from Table 3. In the analyses, the principal material coordinates (1,2,3) of Figure 4 correspond to the FE cartesian (x,y,z) coordinate system of Figure 5, and the CC cylindrical (x,r,θ) coordinate system of Figure 7. Stress components are presented in
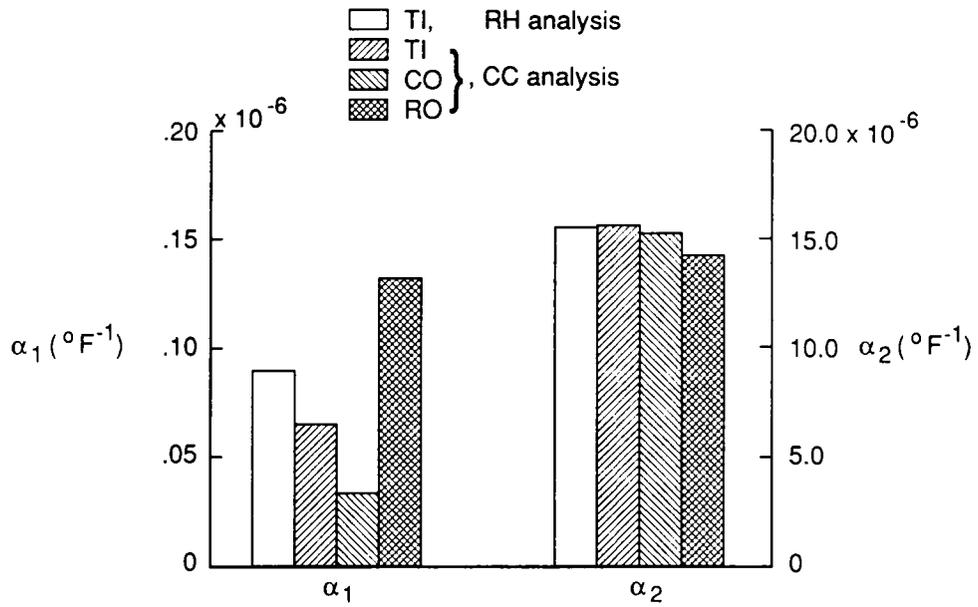
**Figure 22. Effects of fiber orthotropy on the CTE of T300/934 (V^f =0.57).**
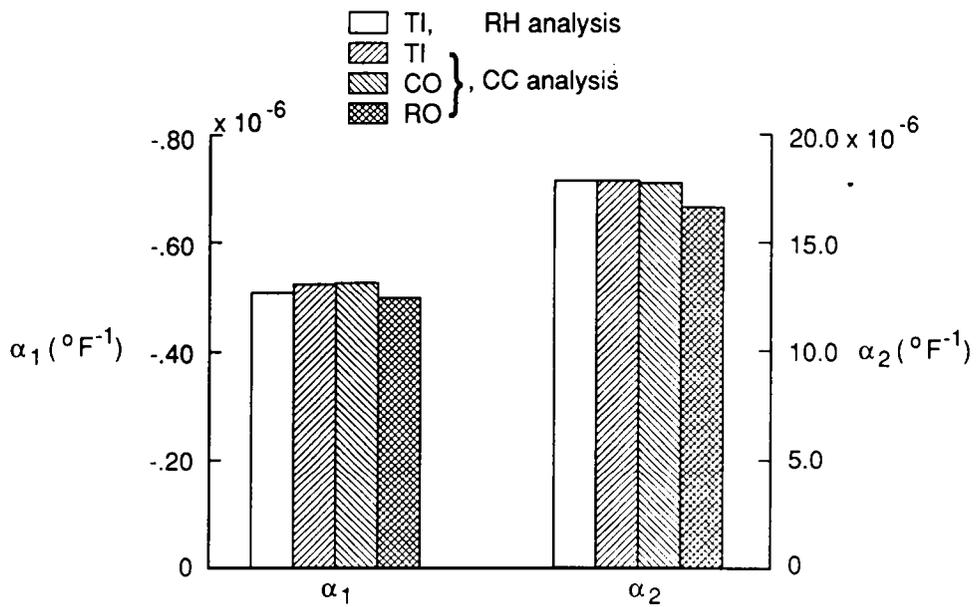
Figure 23. Effects of fiber orthotropy on the CTE of P75/934 (V^f =0.48).

terms of the cylindrical coordinate system (i.e. σ_x, σ_r, σ_θ, and $\tau_{r\theta}$). The thermal load used, unless otherwise noted, was a uniform ΔT of -500°F. This ΔT corresponds to a stress- free-temperature (SFT) of +350°F, which is the cure temperature for 934 epoxy, and a use temperature of -150°F, a typical spacecraft operating environment. Results for unidirectional laminates will be presented first, followed by results from the global/local formulation for predicting stresses in multidirectional laminates.

5.3.1 Unidirectional Laminates

5.3.1.1 Comparison of Analyses. Thermal stress results from the CC and FE analyses are presented for unidirectional P75/934, with a fiber volume fraction, V^f, of 0.60, in Figures 24-29. The matrix stresses at the fiber/matrix interface as a function of the circumferential position around the fiber (θ is measured from the y axis of Figure 5) are shown in Figures 24 and 25. The maximum values of σ_x (16.2 Ksi) and σ_θ (15.2 Ksi) occurred on this interface at the circumferential locations shown in the figures. Both the CC and FE analyses predict approximately the same magnitude and distribution for σ_x. The FE results for σ_θ do exhibit a small dependence on θ, and differ in magnitude from the CC results. For all cases, the FE results using the hexagonal fiber array geometry were in closer agreement with the CC results than those using the square array. This was expected, due to the fact that the hexagonal array more closely resembles an axisymmetric geometry.

The largest differences between the analyses are exhibited in the σ_r and $\tau_{r\theta}$ components at the interface. As shown in Figure 24, the σ_r component varied from approximately -7 Ksi at $\theta = 0°$, to a maximum tensile value of 0.60 Ksi at approximately $\theta = 37°$ for the square array FE results. The CC results predicted a constant value of -3.3 Ksi. There was also a significant $\tau_{r\theta}$ component (Figure 25) in the square array FE results that was nonexsistent in the CC results. The maximum value of $\tau_{r\theta}$ was 5 Ksi (not shown on Figure 25), which occurred at $\theta = 22.5°$, not on the interface but at $r/r_f = 1.2$, where r_f is the fiber radius.

[0] P75/934, $V^f = 0.6$, $\Delta T = -500°$ F

Stress, Ksi

CC
FE-Sq
FE-Hex

σ_x

σ_r

θ , deg
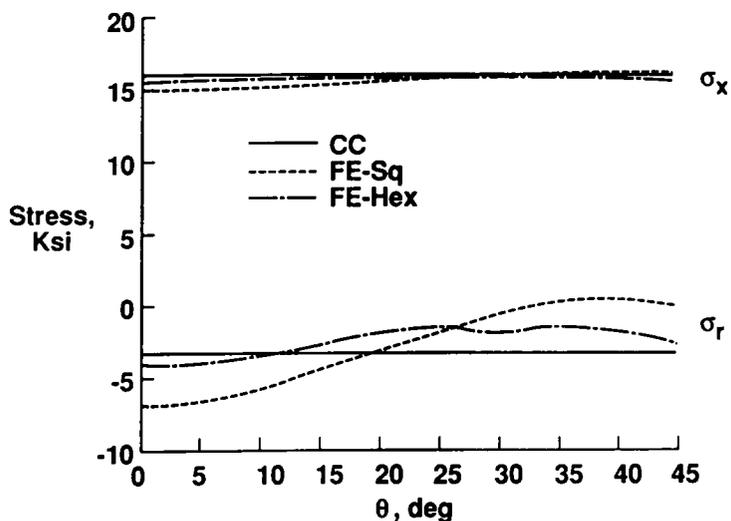
Figure 24. Axial and radial interfacial matrix stresses.

[0] P75/934, $V^f = 0.6$, $\Delta T = -500°$F

CC
FE-Sq
FE-Hex

Stress, Ksi

σ_θ

$\tau_{r\theta}$

θ , deg
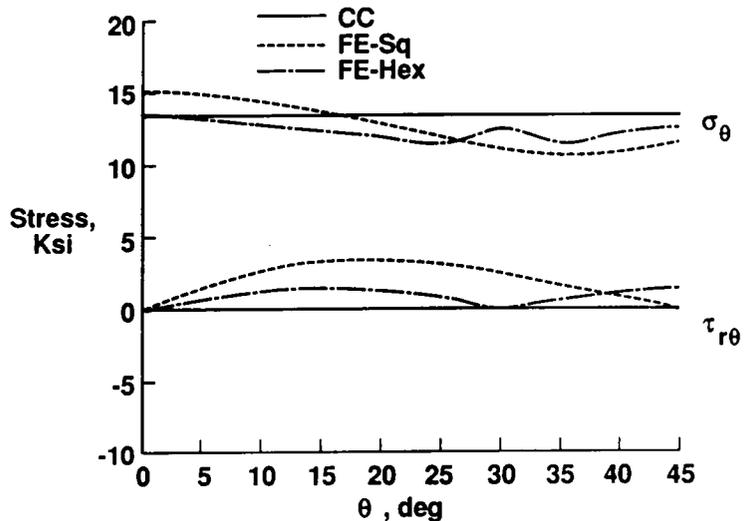
Figure 25. Tangential and shear interfacial matrix stresses.
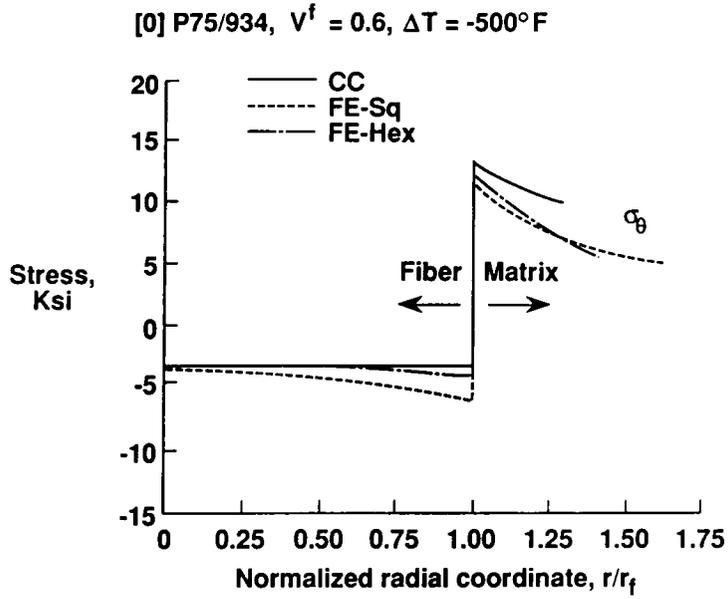
Figure 26. Tangential stresses along the line of maximum fiber spacing.
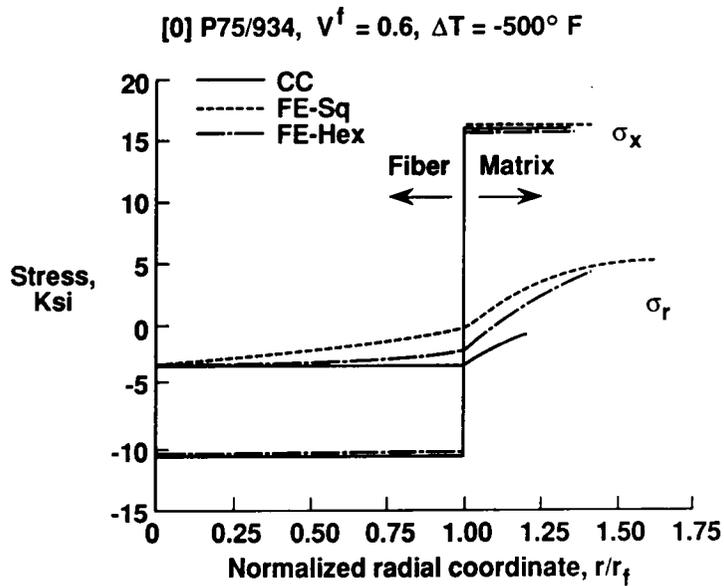
Figure 27. Axial and radial stresses along the line of maximum fiber spacing.

Results and Discussion

54

[0] P75/934, $V^f = 0.6$, $\Delta T = -500°F$
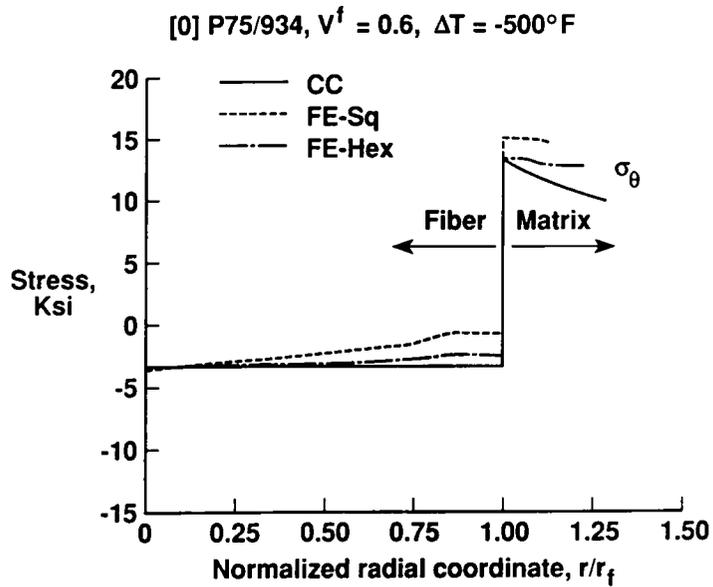
Figure 28. Tangential stresses along the line of minimum fiber spacing.

[0] P75/934, $V^f = 0.6$, $\Delta T = -500°F$
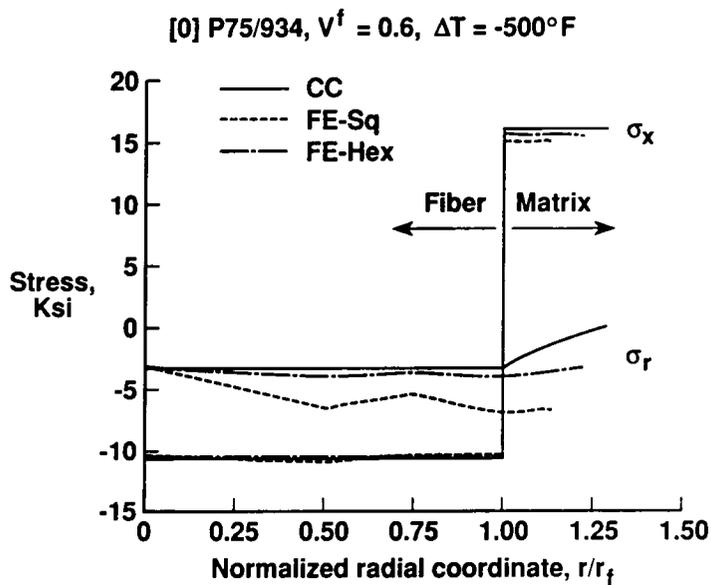
Figure 29. Axial and radial stresses along the line of minimum fiber spacing.

Figures 26 and 27 show the stresses along a radial line of maximum distance between fibers. The circumferential position of this line is either θ = 30°, or 45° depending on whether the results are for the hexagonal or square array, respectively. The radial coordinate was normalized with respect to the fiber radius. The CC results are the same for all radial lines due to its axisymmetric solution. There is no $\tau_{r\theta}$ predicted along this radial line with the FE analysis because it is a line of symmetry. Both the CC and FE analyses predict similar magnitudes and distributions for the fiber stresses. All three components are compressive, with a maximum value of approximately -11 Ksi for σ_x . Both analyses also predict approximately the same magnitude and ditribution for the σ_x matrix stress.

There are significant differences between the predicted values of σ_r and σ_θ in the matrix from the two analyses. The σ_θ component predicted from the FE analysis is significantly smaller than σ_θ from the CC analysis (Figure 26). The other major difference between the two analyses is exhibited in the σ_r component along this radial line (Figure 27). The CC analysis predicts a σ_r stress that is compressive at the interface and decreases to zero at the outer boundary of the CC model, as required by the free surface boundary conditions. The FE analysis also predicts a compressive σ_r at the interface, but this component reaches a tensile value of 5.3 Ksi at the boundary of the FE model (i.e the midpoint of maximum fiber spacing). This is because the FE model does not treat the fiber and surrounding matrix as an isolated problem with stress free boundaries, but rather takes into account the influence of adjacent fibers.

Figures 28 and 29 show the stresses along the radial line of minimum distance between fibers (i.e. θ = 0°). The trends are similar to those exhibited in Figures 26 and 27. The CC results are identical to those shown in Figures 26 and 27 due to the axisymmetric nature of its solution. Again, the shear stress along this line is zero, and the fiber stresses are compressive. The most significant differences between the stresses along this line and those along the line of maximum fiber spacing occur in the matrix σ_θ and σ_r components from the FE analysis. The interfacial value of the σ_θ

component (Figure 28) is significantly larger at this location (15 Ksi) compared to the interfacial value at the maximum distance between fibers (11 Ksi, Figure 26). Also, the σ_r component (Figure 29) remains compressive in the matrix with a magnitude similar to that of the fiber σ_r component.

The above results show that FE analysis predicts higher localized matrix stresses than the CC analysis. This is because the FE analysis takes into account the influence of adjacent fibers, rather than treating a single isolated fiber as in the CC analysis. The effects of these localized higher stress regions on the initiation of damage will be discussed in a subsequent section.

5.3.1.2 Effects of Constituent Properties.

A comparison of the stress distributions for P75/934 and T300/934 are shown in Figure 30. The normal stresses at the interface are compared for the FE square array analysis at a $V^f = .60$. The differences in the stresses are relatively small compared to the large differences in fiber moduli and CTE (Table 1). This may be explained by examining a simple one-dimensional strength of materials formulation for predicting axial thermally induced stresses. Assuming temperature independent properties, the axial stress in the fiber and matrix may be written as[63]

$$\sigma_x^f = V^m E^m E_1^f \left(\frac{\alpha^m - \alpha_1^f}{V^f E_1^f + V^m E^m} \right) \Delta T \qquad (5.3.1.2.1)$$

$$\sigma_x^m = -V^f E^m E_1^f \left(\frac{\alpha^m - \alpha_1^f}{V^f E_1^f + V^m E^m} \right) \Delta T \qquad (5.3.1.2.2)$$

where $V^m = (1 - V^f)$. In polymer matrix composites reinforced with graphite fibers, where $E_1^f \gg E^m$, $V^f E_1^f + V^m E^m$ may be approximated by $V^f E_1^f$. This approximation results in less than a 2% error

[0] FE-Sq analysis, $V^f = 0.6$, $\Delta T = -500°F$
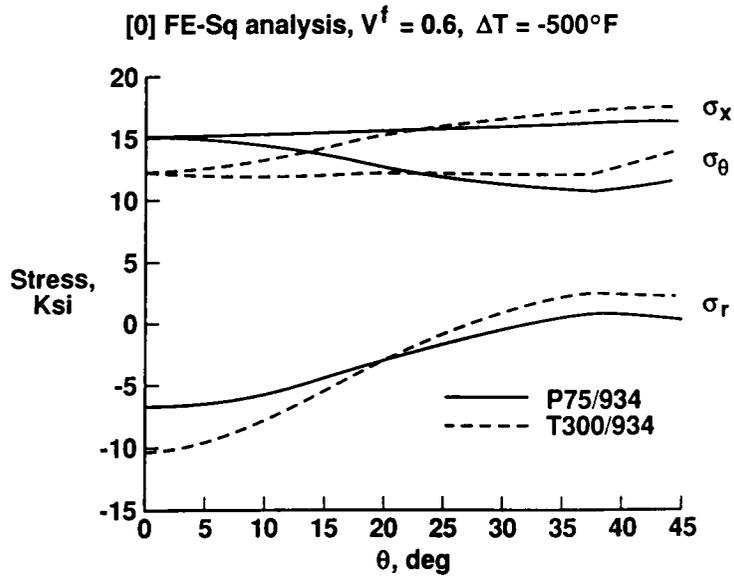
Figure 30. Effects of fiber modulus on interfacial matrix stresses.

for V^f's greater than .50. The term $(\alpha^m - \alpha_1^f)$ may also be approximated by α^m without introducing greater than a 3% error. This is because $\alpha^m \gg \alpha_1^f$.

These two approximations result in simplified forms of equations (5.3.1.2.1) and (5.3.1.2.2) written as

$$\sigma_x^f = (V^m/V^f)E^m\alpha^m\Delta T \qquad (5.3.1.2.3)$$

and

$$\sigma_x^m = -E^m\alpha^m\Delta T \qquad (5.3.1.2.4)$$

The fiber properties do not appear at all in equations (5.3.1.2.3) and (5.3.1.2.4). Although the above simplified analysis is based only on the axial stress component, the same trend is exhibited by the other components, as evidenced by Figure 30. It is also interesting to note that V^f does not appear

in equation (5.3.1.2.4), implying that the axial matrix stresses are not a strong function of V^f for V^f's greater than .50.

In order to significantly reduce the magnitudes of thermal stresses for a fixed ΔT , the term $E^m \alpha^m$ must be reduced. Unfortunately, there exsists an inverse proportionality between E^m and α^m for a wide range of polymer systems[64], as shown in Figure 31. The product, $E^m \alpha^m$, ranges from a high of 17.7 to a low of 12 psi/°F for the polymers shown in the figure. The 934 epoxy has a value of 15.4 psi/°F . Therefore, for a given ΔT , the matrix stresses in a 934 system could be reduced by approximately 22% by using one of the other polymers shown in the figure (i.e. polyphenylene) as the matrix. However, it is not known whether all of these other polymers would make suitable matrix materials for graphite reinforced composites. Large reductions in the level of residual thermal stresses in graphite reinforced composites are obtained by lowering the applied ΔT during use. This could be accomplished from a materials standpoint by lowering the SFT through processing and/or chemistry modifications.

The importance of matrix properties on thermally induced stresses was demonstrated above. Figure 32 shows the importance of properly accounting for the temperature dependence of these properties. Matrix stresses at the fiber/matrix interface were compared for the cases of temperature independent matrix properties and temperature dependent matrix properties. The RT values of 934 epoxy shown in Table 2 were used for the temperature independent case. These results were generated with the FE analysis assuming a square array of fibers. As shown in the figure, the temperature independent property results exhibit stresses that are significantly smaller than the temperature dependent property results for σ_x and σ_θ by as much as 38%. This is due to the stiffening of the 934 epoxy matrix at low temperatures which is neglected when temperature independent properties are assumed.

Based on the results presented above, the effects of fiber orthotropy on thermally induced stresses
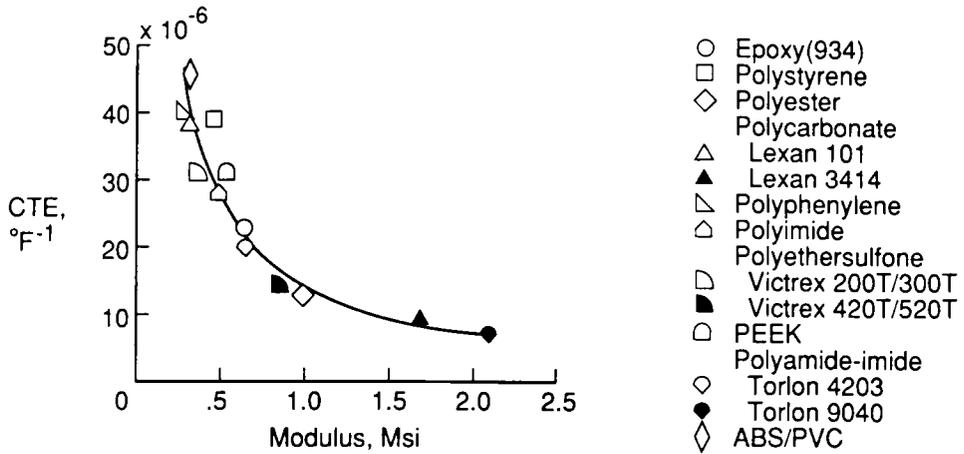
Figure 31. Relationship between CTE and modulus for various polymers.
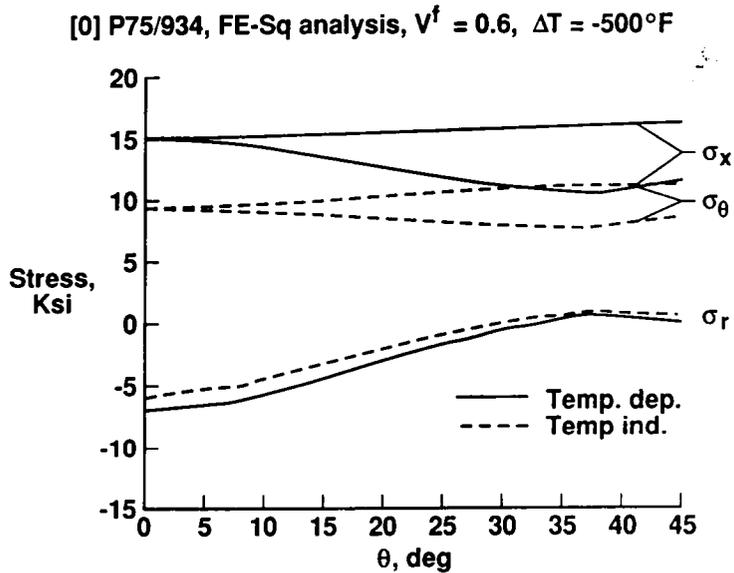

Figure 32. Effects of temperature dependent matrix properties on interfacial matrix stresses.

would be expected to be small. This was proven to be true, as evidenced by the results presented in Table 9. These results were generated with the CC analysis, and used the cylindrically orthotropic properties shown in Table 8. Only small differences in the maximum matrix stresses were predicted for the three types of fiber orthotropy; transversely isotropic (TI), radially orthotropic (RO), and circumferentially orthotropic (CO). The RO fiber had the largest predicted deviation from the TI case, with an approximately 11% larger σ_θ stress component.

Table 9. Effects of Fiber Orthotropy on P75/934 Thermal Stresses (V^f=0.60, ΔT=-500°F).

Type of Orthotropy	Maximum Matrix Stress[1] (Ksi)		
	σ_x	σ_r	σ_θ
TI	15.96	-3.33	13.31
RO	16.36	-3.70	14.80
CO	15.99	-3.36	13.43

(1) Calculations based on CC Analysis

5.3.1.3 Effects of Fiber Volume Fraction.

The effects of V^f on the stress distributions in unidirectional P75/934 were also determined for each analysis. The σ_x , σ_r , and σ_θ matrix stress components, at the fiber/matrix interface, are shown as a function of V^f in Figures 33, 34, and 35, respectively. These results were generated with the FE analysis assuming a square array of fibers. The results for the hexagonal array show similar trends. In general, the FE analysis predicted increases in the absolute value of all of the stress components with increasing V^f. The only exception to this was the σ_r component at θ = 45°, which changed from a compressive -5.7 Ksi at V^f = .10 to a tensile value of 2.8 Ksi at V^f = .75. The behavior of the matrix σ_r component was also the major difference between the stresses as a function V^f from the CC and FE analyses. The CC analysis predicted a steadily decreasing compressive value of σ_r towards zero with increasing V^f. One of the most significant features of these data is the presence of large matrix stresses even at very low values of V^f. This is especially true for σ_x , where the maximum matrix stress at V^f = .10

[0] P75/934, FE-Sq analysis, $\Delta T = -500°F$
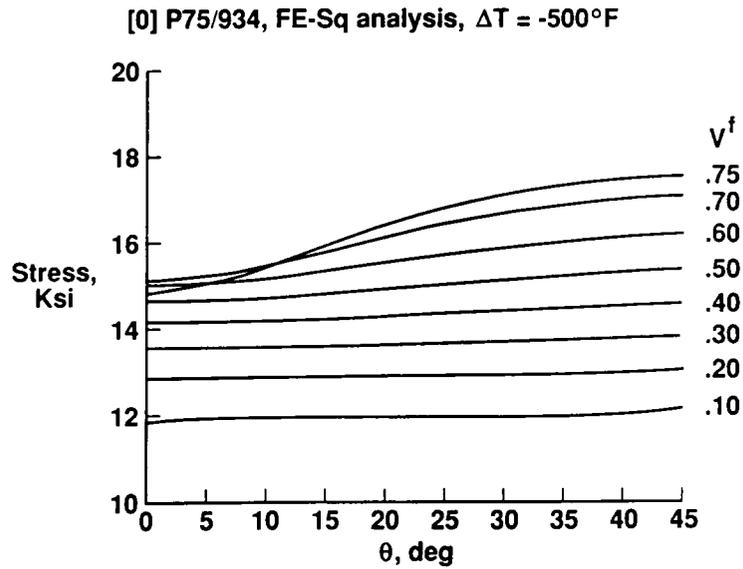
Figure 33. Effects of V^f on axial interfacial matrix stresses.

[0] P75/934, FE-Sq analysis, $\Delta T = -500°F$
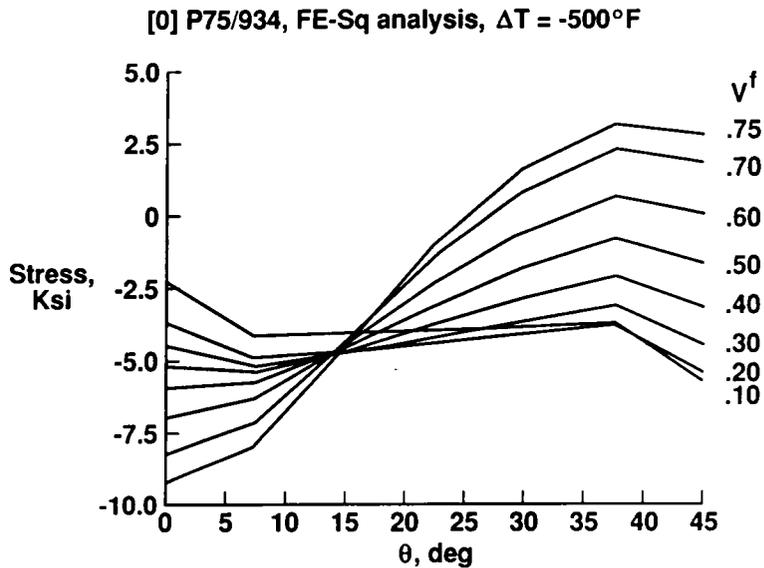
Figure 34. Effects of V^f on radial interfacial matrix stresses.

[0] P75/934, FE-Sq analysis, ΔT = -500°F
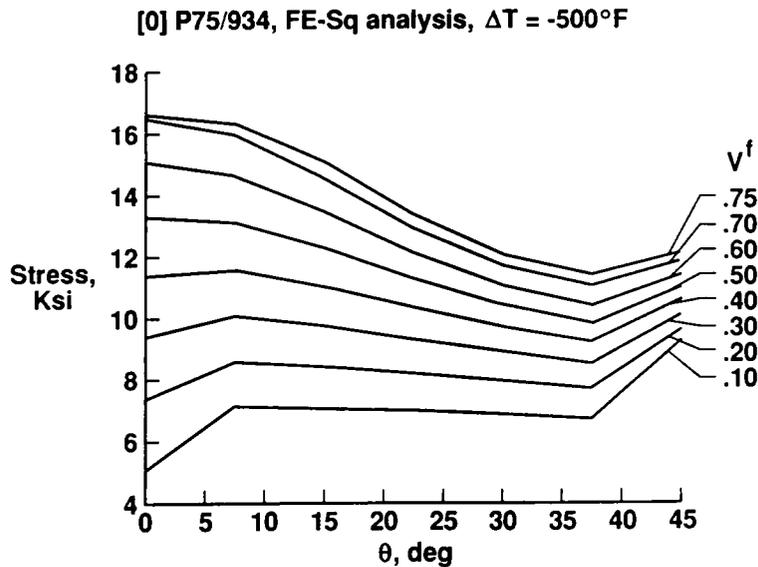
Figure 35. Effects of V^f on tangential interfacial matrix stresses.

is only 30% less than the maximum value of 17.6 Ksi at V^f = .75. These results support the trends

exhibited by the simple one-dimensional analysis presented in the preceding section, where V^f

does not appear in the expression for σ_x^m (equation (5.3.1.2.4)).

The array geometries used in the FE analysis have upper bounds on V^f for contiguous fibers. These

upper bounds are V^f = .785 and V^f = .907 for the square and hexagonal arrays, respectively.

The upper bound on V^f for the CC analysis is 1.0, or no matrix phase, for which case the matrix

stresses are obviously zero. The matrix stresses at the fiber/matrix interface for V^f's of .75, .85, and

.99, corresponding to the FE square array, FE hexagonal array, and CC analyses, respectively, are

shown in Figure 36 and 37. Values of .75 and .85 were used as upper limits on V^f for the square

and hexagonal array FE analyses, respectively, due to difficulties in modeling a contiguous fiber

array with the type of elements used in the analysis. An upper limit of V^f = .99 was used for the

CC analysis to represent the presence of a small, but measurable matrix phase. It is interesting to

note that, for the σ_x and σ_θ components, there are only small differences in the maximum tensile
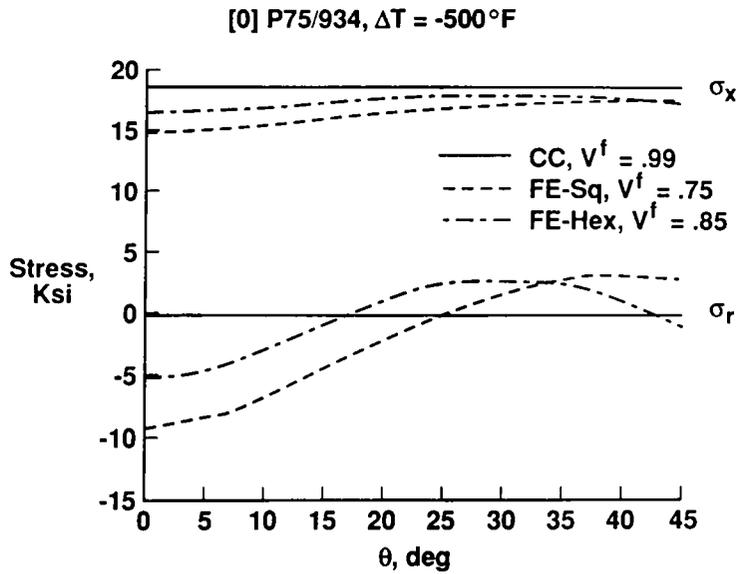
Figure 36. Effects of analysis V^f upper bound on axial and radial interfacial matrix stresses.
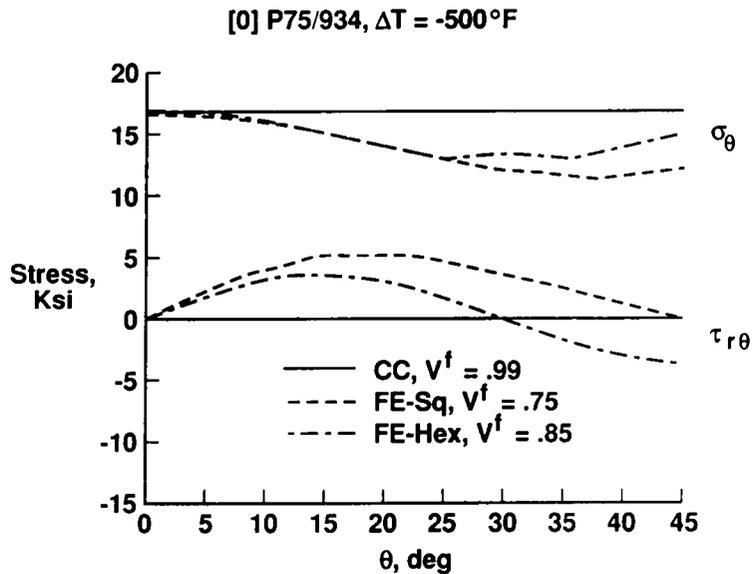
Figure 37. Effects of analysis V^f upper bound on tangential and shear interfacial matrix stresses.

values for the three different values of V^f.

A real composite does not have fibers arranged in regular periodic arrays, as assumed in the FE analysis, nor consists of cylinders of fiber and matrix with varying diameters, as assumed in the CC analysis. A photomicrograph of the structure of a real composite is shown in Figure 38. One of the most striking features revealed by this figure is the wide range of V^f's present in the specimen. Even though this specimen has an average or global V^f of .50, there are localized regions with much smaller and much larger V^f's.

An attempt at modeling localized regions of high V^f in a global V^f region of 0.60 was made using a global/local FE scheme, similar to the one described in **Section 3.3.3**. The procedure is shown schematically in Figure 39. The FE model for $V^f = .75$ in the square array was constrained by three different sets of global boundary conditions as follows: Case 1, ϵ_x and ϵ_y from $V^f = .60$, Case 2, ϵ_x from $V^f = .60$ and ϵ_y unconstrained, and Case 3, ϵ_x from $V^f = .60$ and ϵ_y from $V^f = .75$. The results from this procedure, for the matrix stress components at the fiber/matrix interface, are shown in Figures 40 and 41. Cases 2 and 3 gave nearly identical results and therefore are labled as one curve in the figures. For comparison purposes, the stresses for actual cases of $V^f = .60$ and $V^f = .75$ are also shown in the figures.

As can be seen in the figures, cases 2 and 3 gave results very similar to the actual $V^f = .75$ case. Case 1 predicted stresses lower than those of the actual $V^f = .60$ case. It should be noted that cases 1, 2, and 3 all predicted tensile σ_x fiber stresses. This is opposite of the compressive σ_x fiber stresses predicted in all of the earlier results (Figures 26-29), and is due to the imposition of the $V^f = .60$ ϵ_x boundary condition. The $V^f = .75$ model normally contracts more in the axial direction than is allowed by this boundary condition, and thus tensile axial stresses are set up in both the fiber and matrix. Although none of the three cases accurately represent the real boundary conditions, cases 2 and 3 seem more plausible since they maintain a uniform axial strain consistent with the
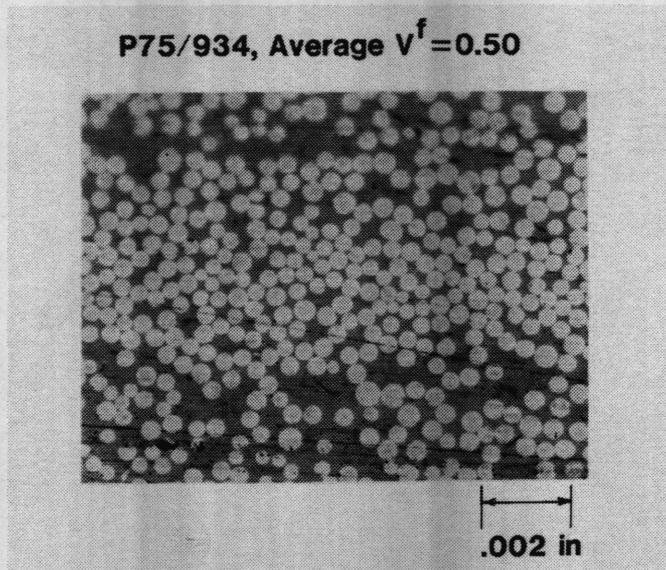
Figure 38. Photomicrograph of typical composite showing local variations in V^f.
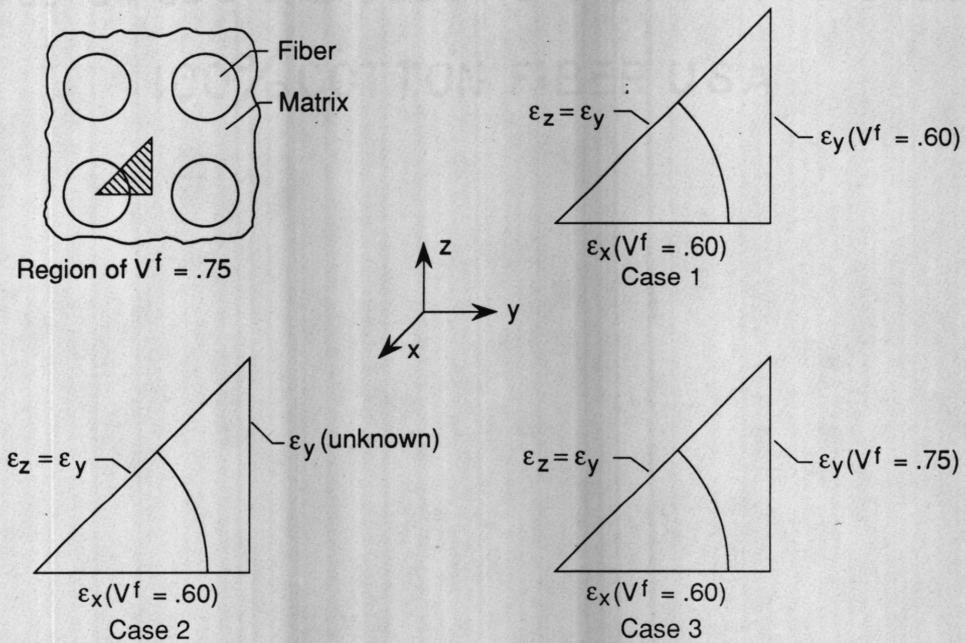

Figure 39. Global/local finite element analysis of localized high V^f regions.
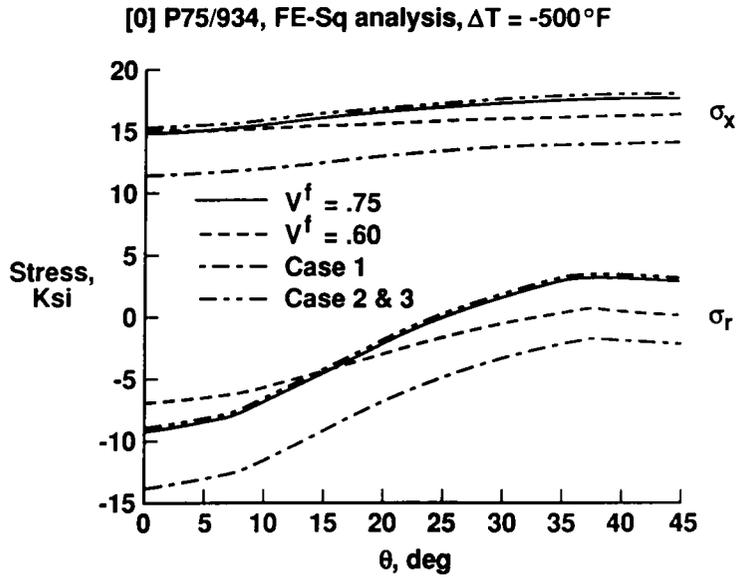
Figure 40. Effects of high local V^f on axial and radial interfacial matrix stresses.
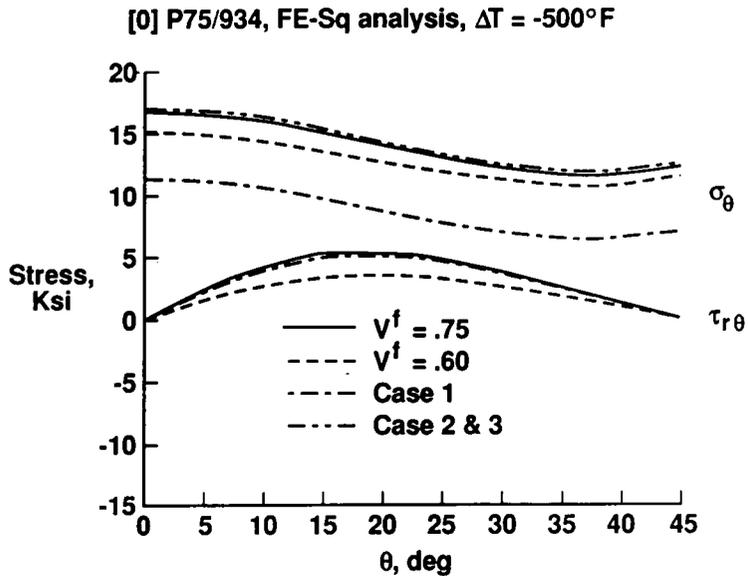
Figure 41. Effects of high local V^f on tangential and shear interfacial matrix stresses.

global V^f, but allow the transverse strains to be consistent with the local V^f. Case 1 seems overly constrained by forcing the transverse strains to be consistent with the global V^f over a distance of one fiber radius. The real boundary conditions probably lie somewhere between cases 2 and 3, and case 1. Based on these results, it appears that a resonable conservative first approximation to the matrix stresses in localized regions of high V^f can be predicted from the actual (i.e unconstrained) model of that region.

5.3.2 Multidirectional Laminates

The global/local formulation, described in **Section 3.3.3**, was used to determine the thermally induced matrix stresses in multidirectional P75/934 laminates. The class of laminates selected for investigation were the $[0_2/\pm\theta]_s$ family, with θ having values of 0, 15, 30, 45, 60, 75, and 90 degrees. This class of laminates includes both the minimum amount of ply property mismatch ($\theta = 0°$, or unidirectional), and the maximum amount of ply property mismatch ($\theta = 90°$), or "worst case". Lamina strains in the principal material coordinate directions were determined for these laminates using equations (3.3.3.1) through (3.3.3.5). The lamina elastic properties used in these calculations were determined from the CCA model of Hashin[23] using the fiber and matrix properties given in Tables 1 and 3. The calculated lamina strains for a ΔT of -500 °F are shown in Table 10. These values were used as boundary conditions for the FE micromechanics analysis.

A comparison of unidirectional and $[0_2/\pm\theta]_s$ matrix stresses in the $\pm\theta$ plies at the fiber/matrix interface are shown in Figures 42-44. The σ_x, σ_r, σ_θ, and $\tau_{r\theta}$ components (Figures 42-43) all increase in magnitude with increasing ply angle up to an angle of $\pm60°$. For angles greater than $\pm60°$ the magnitudes of the stresses remained nearly constant. These layups are labeled as one curve in the figures. The most significant difference between the unidirectional and $[0_2/\pm\theta]_s$ response is the presence of a large tensile value of σ_r at the fiber/matrix interface. The σ_r

component reaches a maximum interfacial tensile value of 7 Ksi in the $[0_2/90_2]_s$ laminate at a circumferential position of approximately 30°. The overall maximum tensile value of the matrix σ_r component occurs at this circumferential position, but at the midpoint between fibers. The other major difference between the unidirectional and $[0_2/\pm\theta]_s$ response is the presence of out-of-plane shear stresses $\tau_{\theta x}$ and τ_{xr}. The maximum matrix values of these components occurred at the fiber/matrix interface, and are shown in Figure 44. Except for the presence of these out-of-plane shear components, the magnitudes and trends of the matrix stresses in the 0° plies were very similar.

Table 10. Lamina Strains in $[0_2/\pm\theta]_s$ P75/934 Laminates (V^f=0.60, ΔT=-500 °F).

Laminate Orientation	0° Ply Strains[1] (10^{-6})				$\pm\theta$ Ply Strains[1] (10^{-6})			
	ϵ_1	ϵ_2	γ_{12}	ϵ_3	ϵ_1	ϵ_2	γ_{12}	ϵ_3
[0]	261	-7673	0	-7800	na	na	na	na
$[0_2/\pm 15]_s$	488	-7180	0	-8200	-26	-6670	-3830	-8200
$[0_2/\pm 30]_s$	654	-3730	0	-10000	-442	-2640	-3800	- 10000
$[0_2/\pm 45]_s$	358	-991	0	-11100	-316	-316	-1350	- 11100
$[0_2/\pm 60]_s$	132	-214	0	-11400	-128	45	-300	- 11400
$[0_2/\pm 75]_s$	28	-34	0	-11400	-30	24	-31	- 11400
$[0_2/90_2]_s$	~ 0	~ 0	0	-11400	~ 0	~ 0	0	-11400

(1) Calculations based on LPT

There were also differences in the fiber stresses between the $[0_2/\pm\theta]_s$ and unidirectional laminates. The largest difference was observed in the σ_x component. The $[0_2/\pm 15]_s$, $[0_2/\pm 30]_s$, and $[0_2/\pm 45]_s$ laminates all had predicted tensile values of the fiber σ_x component in the 0° plies. The largest of these was 74 Ksi in the $[0_2/\pm 30]_s$ laminate. This was in contrast to the compressive value of approximately -10 Ksi predicted for the unidirectional laminate. The other major difference was the -100 Ksi σ_x fiber stress in the ±15° plies of the $[0_2/\pm 15]_s$ laminate. This value was an order of magnitude larger than the value predicted in the unidirectional laminate.

P75/934, FE-Sq analysis, $V^f = .60$, $\Delta T = -500°F$
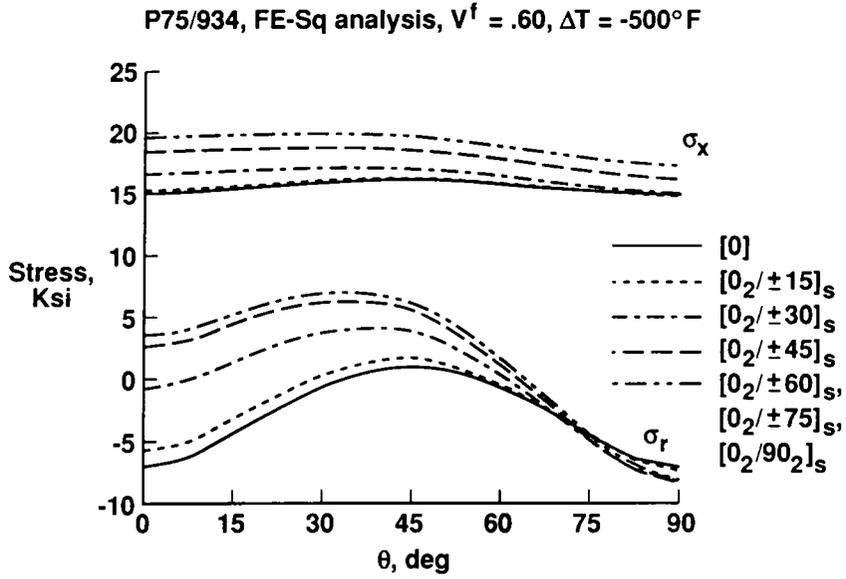
Figure 42. Effects of laminate orientation on axial and radial interfacial matrix stresses.

P75/934, FE-Sq analysis, $V^f = .60$, $\Delta T = -500°F$
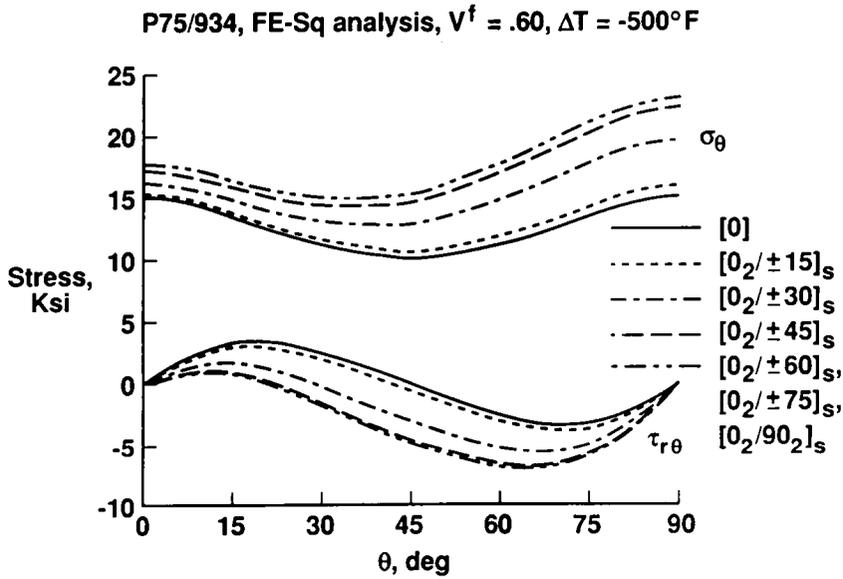
Figure 43. Effects of laminate orientation on tangential and shear interfacial matrix stresses.
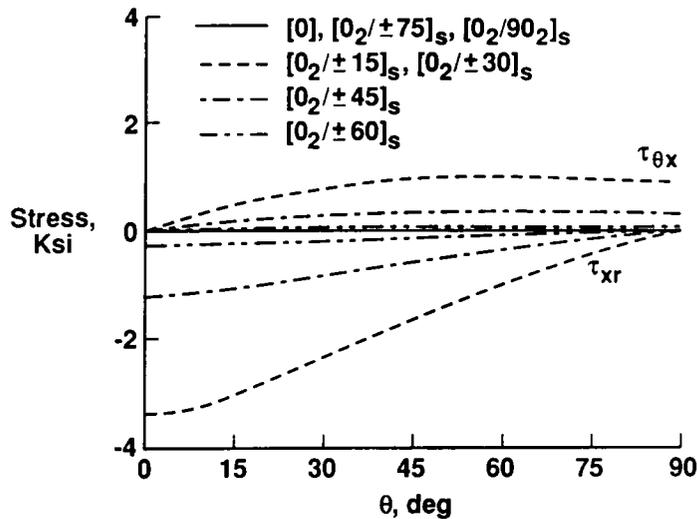
Figure 44. Effects of laminate orientation on out-of-plane shear interfacial matrix stresses.

Table 11 shows a comparison of the maximum stresses predicted from the micromechanics FE analysis with those predicted from LPT for the $[0_2/90_2]_s$ laminate. Both the maximum tensile and compressive values are shown, when present, for the FE predictions. LPT assumes that a state of plane stress exists in the laminate, with σ_x, σ_y, and τ_{xy} as the only nonzero stress components. These stresses are computed for individual lamina, which are modeled as homogeneous orthotropic layers. The micromechanics FE analysis models the fiber and matrix as distinct individual phases, and the stresses predicted from this analysis refer to these individual phases. As shown in Table 11, the micromechanics FE analysis predicts a three-dimensional state of stress in the fiber and matrix, with stress levels much larger than the lamina components predicted from LPT. These differences have a significant influence on the prediction of thermally induced damage, as will be discussed in the next section.

Table 11. Maximum stresses in $[0_2/90_2]_s$ P75/934 (V^f=0.60, ΔT=-500°F).

LPT	FE	
Lamina Stresses (Ksi)	Fiber Stresses (Ksi)	Matrix Stresses (Ksi)
$\sigma_x = -9.95$	$\sigma_x = -30.3$	$\sigma_x = 19.9$
$\sigma_y = 9.95$	$\sigma_r = 7.3, -8.9$	$\sigma_r = 12.1, -8.0$
$\tau_{xy} = 0.00$	$\sigma_\theta = 9.9, -4.5$	$\sigma_\theta = 23.4$
	$\tau_{r\theta} = 1.4, -7.6$	$\tau_{r\theta} = 2.6, -9.3$

5.4 Thermally Induced Damage

Thermally induced damage, in the form of matrix cracks, is well documented for polymer matrix composites exposed to temperatures far below their cure temperature[5-7,9,10]. The thermal stress analysis presented in the preceding sections will be used to predict the initiation temperature and location of this type of damage. These predictions will be compared to experimental data generated for this study on unidirectional and $[0_2/90_2]_s$ P75/934 composites, and with literature data on T300/934 and T300/5208 composites.

In addition to thermal stress field information, damage initiation predcitions also require failure strength data, and a failure criterion that relates the induced stresses to the failure strength. As stated earlier, the majority of experimental data suggests that thermally induced failures in polymer matrix composites take the form of matrix cracks. However, data on the failure strength of the neat matrix material is very limited. Elevated (+250°F) and RT tensile data on 934 epoxy are reported in the literature by Fox et. al.[59], but no data for temperatures below RT could be found. The 934 ultimate strengths reported by Fox et. al. were $\sigma_{ult}^m = 8.53$ Ksi and $\sigma_{ult}^m = 10.30$ Ksi at RT and +250°F, respectively. Fox et. al. also reported proportional limits, defined as the stress at which the stress-strain curve departs from linearity, of $\sigma_{pl}^m = 3.42$ Ksi and $\sigma_{pl}^m = 2.44$ Ksi at RT

and $+250\,°F$, respectively. These data were obtained during static tension tests to failure (i.e. no unloading and reloading), and therefore it is not known whether this proportional limit corresponds to a material yield point.

A maximum stress failure criterion, using the square array FE results, was used as the initial model to predict thermally induced failures in P75/934 laminates. This criterion predicts failure when any of the principal stresses first exceeds the ultimate strength of the material. For the case of failures in the 934 matrix, the maximum calculated tensile principal stress, σ_1, was compared to the ultimate tensile strength of the matrix, σ_{ult}^m. The principal stresses were calculated at temperatures of 250, 150, 75, -50, and $-150\,°F$ which correspond to applied ΔT 's of -100, -200, -275, -400, and $-500\,°F$, respectively. The results for a [0] and $[0_2/90_2]_s$ laminate at a V^f = .50 are shown in Figure 45. The V^f = .50 is consistent with the experimental P75/934 data[10]. The first failure in the [0] laminate was predicted at approximately $40\,°F$. The maximum σ_1 stress for this laminate always occured in the axial (x) direction on the fiber/matrix interface at the circumferential location shown on the figure. First failure in the $[0_2/90_2]_s$ laminate was predicted at $95\,°F$. The direction of σ_1 was in the transverse, or y direction, and again occured at the fiber/matrix interface at a circumferential location shown on the figure. Based on the results described in **Section 5.3.1.2** and shown on Figure 30, failures in T300/934 composites would be predicted at approximately the same temperatures and locations.

The results presented in Figure 45 do not agree with experimentally observed failures. First, no thermally induced failures have been observed in either P75/934, or T300/934 [0] laminates subjected to repeated thermal cycling between $\pm250\,°F$ [4,10]. Secondly, thermally induced failures in T300/934 and T300/5208 $[0_2/90_2]_s$ laminates have only been observed in specimens exposed to temperatures below $-200\,°F$ [4,9]. T300/5208 is very similar in response and properties to T300/934. Thirdly, although P75/934 $[0_2/90_2]_s$ laminates do exhibit thermally induced failures at temperatures

P75/934, FE-Sq analysis, $V^f = .50$
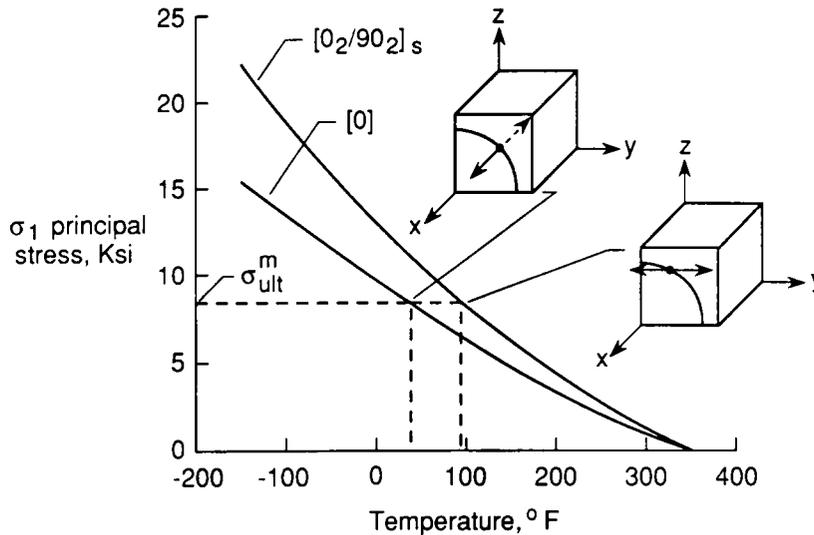
Figure 45. Predicted thermally induced matrix failures using a maximum stress failure criterion.

above $RT^{(10)}$, the mode of failure appears to be due to a combination of a transverse component and a radial normal component at the interface. A photomicrograph of a typical thermally induced failure in a P75/934 $[0_2/90_2]_s$ laminate is shown in Figure 46.

Two possible explanations for the discrepencies between the experimental data and the results of Figure 45 are as follows. First, the FE stress analysis assumed linear elastic matrix behavior. However, as noted above, Fox et. al, reported a RT proportional limit of 3.42 Ksi in the stress-strain behavior of 934 epoxy. A von Mises yield criterion was used to predict the temperature at which this proportional limit would be reached. The von Mises criterion predicts yielding when

$$\tau_{oct} = \sqrt{2}\sigma_{yp}/3 \qquad (5.4.1)$$

where

$$\tau_{oct} = \frac{\sqrt{(\sigma_1 - \sigma_2)^2 + (\sigma_2 - \sigma_3)^2 + (\sigma_3 - \sigma_1)^2}}{3} \qquad (5.4.2)$$

$[0_2/90_2]_s$ P75/934, V^f=0.50

.002 in

After fabrication
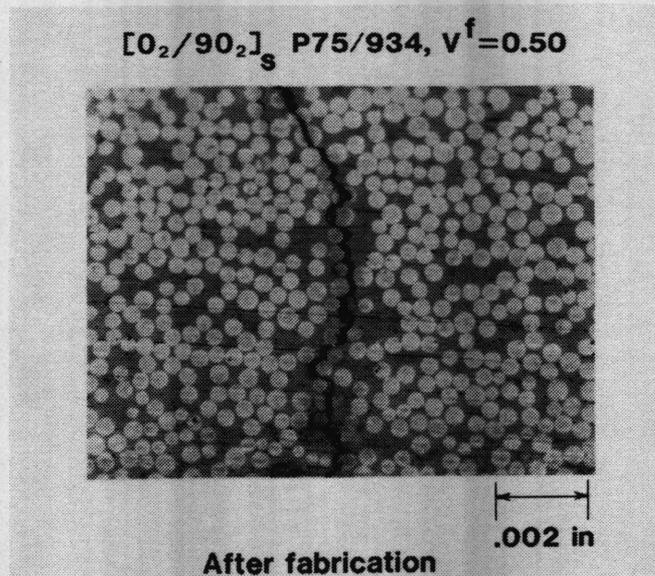
Figure 46. Photomicrograph of typical thermally induced failure in a $[0_2/90_2]_s$ P75/934 laminate.

and the components σ_1, σ_2, and σ_3 are the principal stresses. The results predicted by substituting the RT value of σ_{pl}^m for σ_{yp} in equation (5.4.1) are shown in Figure 47. As shown in the figure, matrix yielding was predicted to begin at approximately 240 and 260 °F for the [0] and $[0_2/90_2]_s$ P75/934 laminates, respectively. For the [0] laminate, the maximum value of τ_{oct} occurred on the fiber/matrix interface at a circumferential location close to the y axis. For the $[0_2/90_2]_s$ laminate, the maximum value of τ_{oct} occured a short distance away from the interface at a circumferential location close to the z axis. The inclusion of this nonlinear matrix behavior in the analysis would have lowered the predicted stresses, and changed the predicted first failure loads.

The second, and more conclusive explanation of the discrepancies between the experimentally observed thermal matrix failures, and the predicted failure loads and modes, is that the matrix ultimate strength, σ_{ult}^m, is not representative of the actual in-situ strength of the matrix. This claim is supported by the large differences observed between experimental values of σ_{ult}^m, given above, and values of the transverse tensile strength (Y_T) measured for unidirectional P75/934, at NASA-LaRC,

P75/934, FE-Sq analysis, $V^f = .50$
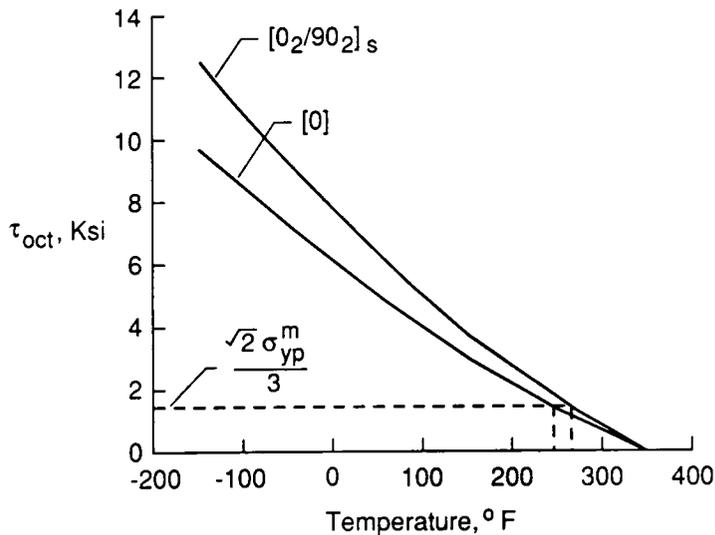
Figure 47. Predicted thermally induced matrix yielding using a von Mises yield criterion.

and T300/934[60]. These values are given in Table 12. The difference in Y_T for the two composite systems suggests a difference in the interfacial bond characteristics of the two composites. These data show that T300 fibers form a much stronger bond than P75 fibers with the 934 epoxy. The slightly larger value of Y_T compared to σ_{ult}^m at RT for the T300/934 composite is not understood, but may be within the scatter of the experimental data. One possible cause for this difference in Y_T's is the difference in morphologies (**Section 5.1**) of these two fibers due to differences in their processing. Differences in Y_T for composites with different modulus carbon fibers (AS4, 30 Msi fibers, and P75) have also been measured in thermoplastic PEEK matrix composites[65].

Table 12. Comparison of Neat Matrix and Transverse Lamina Ultimate Tensile Strengths.

Temperature (°F)	934 Epoxy σ_{ult}^m (Ksi)	P75/934 Y_T (Ksi)	T300/934 Y_T (Ksi)
250	10.30	3.20	6.76
75	8.53	3.50	9.37
-250	NA	1.00	4.56
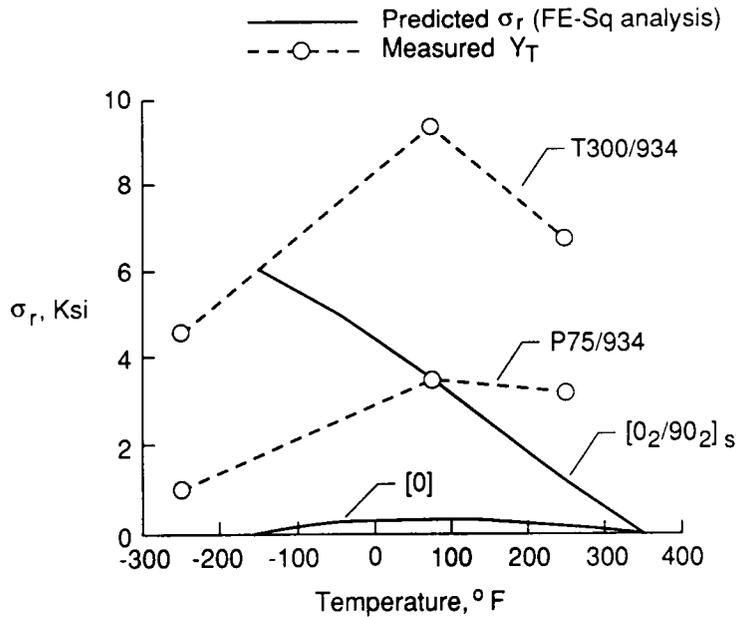
Figure 48. Comparison of radial interfacial matrix stress with measured transverse lamina strength.

The maximum predicted matrix σ_r interfacial stress as a function of temperature, for [0] and $[0_2/90_2]_s$ P75/934 laminates, is compared to the experimental values of Y_T in Figure 48. As discussed earlier, predicted σ_r values for T300/934 and T300/5208 laminates would be very similar in magnitude to those presented in Figure 48 for the P75/934 laminates. Assuming Y_T to be representative of the interfacial bond strength, failure (i.e. fiber/matrix disbonding) would be predicted when σ_r exceeded Y_T. Based on this criterion and the results of Figure 48, failures were predicted in $[0_2/90_2]_s$ P75/934 and T300/934 laminates at approximately 75°F and -150°F, respectively. No failures are predicted in [0] laminates of either system. These failure predictions are in excellent agreement with the experimental data cited earlier.

The results presented in this section show that neat matrix strength is not a good measure of composite failure strength under thermal loading conditions. A failure criterion based on interfacial bond strength was much more successful in predicting thermally induced failures in the two composite systems studied. The lamina transverse strength, Y_T, appears to be a good first

approximation of the interfacial bond strength. However, more research is needed to accurately quantify this strength.

6.0 Concluding Remarks

The objective of this research study was to analyze the deformations and stresses, induced by thermal loading, in continuous fiber reinforced composites using the properties and behavior of the constitutents (i.e. fiber and matrix). The study focused on two primary areas. First, available explicit expressions for predicting the effective coefficients of thermal expansion (CTE's) for a composite were compared with each other, and with a finite element (FE) analysis that was developed as part of this study. Comparisons were made for a wide range of fiber/matrix systems to determine the influence of the constituent properties. All of the predictions were compared with experimental data to assess the validity and shortcomings of the individual analyses. The major conclusions from this portion of the study may be stated as follows.

- All of the analyses investigated predicted nearly indentical values of the axial CTE, α_1, for a given material system, and all of the predictions were in good agreement with the experimental data. This implies that simple strength-of-materials (SOM) formulations are adequate for accurately predicting values of α_1.

- Results from the FE analysis, and those from the solution of a generalized plane strain boundary value problem, were in excellent agreement with each other, and with the experimental data for the transverse CTE, α_2. The less rigorous plane stress and strength-of-materials formulations were in poor agreement with the experimental data for all of the material systems studied.

- As was expected, predicted values of α_1 were most sensitive to the axial properties of the fiber, and the predicted values of α_2 were most sensitive to matrix properties. The sensitivity of α_2 to transverse fiber properties was less than expected.

- Moderate amounts of cylindrical fiber orthotropy (i.e. $E_r = 2E_\theta$ or vice versa) had a negligible effect on the predicted values of α_1 and α_2. This degree of cylindrical fiber orthotropy is justified based on the excellent aggreement observed between predicted and experimental values of α_1 and α_2 when transversely isotropic fiber behavior was assumed.

The second portion of this study focused on the determination of thermally induced stress fields in the individual constituents. Stresses predicted from a FE analysis were compared to those predicted from the closed-form Composite Cylinder (CC) analysis for unidirectional laminates. The thermal load was representative of cooling from an elevated temperture cure ($350\,°F$) to a typical cold ($-150\,°F$) spacecraft environment. The constituent properties and microstructure that control the behavior were identified and material modifications to improve the behavior were suggested. A simple global/local FE formulation was used to asses the influence of local variations in fiber volume fraction, V^f, and multiple ply laminate constraints on the constituent stresses. Thermal stress calculations were used to predict probable damage initiation locations, and the results were compared to experimentally observed damage in several epoxy matrix composites. The major conclusions from this portion of the study may be stated as follows.

- The type of analysis (i.e. CC or FE) significantly affected the distributions and magnitudes of the predicted thermally induced stresses. The most notable difference was the absence of any tensile values of the radial matrix stress component, and the absence of any in-plane shear stresses. These differences are due to the fact that the CC analysis does not account for the influence of adjacent fibers.

Concluding Remarks   . 80

- Thermally induced matrix stresses were not a strong function of fiber properties. Consequently, moderate amounts of fiber orthotopy had negligible effects on the matrix stresses. The two most promising methods to significantly lower the magnitudes of thermally induced matrix stresses are reducing the product of the matrix modulus and CTE ($E^M \alpha^m$), and reducing the applied temperature change. For a fixed operating temperature, this implies lowering the cure temperature.

- Matrix stresses increased in absolute value with increasing V^f. Global/local analyses showed that stresses in local regions of high V^f, constrained by a lower global V^f, can be approximated by an unconstrained analysis of the high V^f region.

- Multidirectional $[0_2 / \pm \theta]_s$ laminates had larger predicted matrix stresses than unidirectional ($[0]$) laminates. The stresses increased with increasing lamination angle θ, up to $\theta = \pm 60°$. The magnitudes of matrix stresses remained approximately constant for $\theta \geq 60°$ up to $\theta = 90°$. The most significant differences from the $[0]$ laminate response were the presence of a large tensile radial matrix stress component, σ_r, at the interface, and the existence of non-zero out-of-plane matrix shear stresses, $\tau_{\theta x}$ and τ_{xr}.

- Thermally induced matrix failure predictions, using a maximum stress failure criterion and the ultimate tensile strength of the matrix, σ_{ult}^m, were in very poor agreement with experimental data. The two reasons postulated for these discrepancies were non-linear matrix behavior, and σ_{ult}^m, a neat matrix property, not being representative of the in-situ matrix strength. The second reason was supported by experimental observations of matrix damage, and measured values of transverse lamina strength, Y^T. A failure criterion based on the radial interfacial stress component and Y^T, was in excellent agreement with experimental data.

In summary, a micromechanics analysis was developed, and used for predicting the thermally induced deformations and stresses in a composite exposed to a typical spacecraft environment.

Predicted deformations of the composite were in good agreement with experimental data. Calculated matrix stresses were used to predict thermally induced matrix failures, and were in good agreement with the experimental data when representative values of the in-situ matrix strength were used in the failure criterion. Future research should focus on more accurate modeling of matrix behavior (i.e. nonlinear behavior), and a more thorough understanding of interfacial bond characteristics.

7.0 References

1. Bowles, D. E.; and Tenney, D. R.:Composite Tubes for the Space Station Truss Structure. *Proceedings of 18th National SAMPE Technical Conference*, October 1986, pp. 414-428.

2. Mahoney, M. J.:Report of the Asilomar III LDR Workshop. *Jet Propulsion Laboratory Report 88-23*, August 15, 1988.

3. McMahan, L. L.:Space Telescope Optical Telescope Assembly Structural Materials Characterization. *Proceedings of AIAA Technology for Space Astrophysics Conference*, October 1982, pp. 127-137.

4. Tenney, D. R,; Sykes, G. F.; and Bowles, D. E.:Composite Materials for Space Structures. *Proceedings of 3rd European Symposium on Spacecraft Materials in Space Environment*, October 1985, pp. 9-21.

5. Herakovich, C. T.; Davis, J. G.; and Mills, J. S.:Thermal Microcracking in Celion 6000/PMR-15 Graphite/Polyimide. *Proceedings of International Conference on Thermal Stresses in Materials and Structures in Severe Environments*, 1980, pp.649-664.

6. Tompkins, S. S.; and Williams, S. L.:Effects of Thermal Cycling on Residual Mechanical Properties of C6000/PMR-15 Graphite/Polyimide. AIAA paper No. 82-0710, *Proceedings of AIAA 23'rd SDM Conference*, 1982.

7. Cohen D.; Hyer, M. W.; and Tompkins, S. S.:The Effect of Thermal Cycling on Matrix Cracking and Stiffness Changes in Cross-Ply Graphite/Epoxy Tubes. *Virginia Tech Report VPI-E-84-29*, August 1984.

8. Bowles, D. E.:Effects of Microcracks on the Thermal Expansion of Composite Laminates. *Journal Composite Materials*, Vol. 18, No. 2, March 1984, pp. 173-187.

9. Adams, D. S.; Bowles, D. E.; and Herakovich, C. T.:Thermally Induced Transverse Cracking in Graphite/Epoxy Cross-Ply Laminates. *Journal of Reinforced Plastics and Composites*, Vol. 5, July 1986, pp. 152-169.

10. Bowles, D. E.; and Shen, J.:Thermal Cycling Effects on the Dimensional Stability of P75 and P75-T300(Fabric) Hybrid Graphite/Epoxy Laminates. *Proceedings of 33'rd International SAMPE Symposium and Exhibition*, March 1988, pp. 1659-1671.

11. Bowles, D. E.:Finite Element Composite Analysis Program (FECAP) for a Microcomputer. *NASA TM100670*, July 1980.

12. Bowles, D. E.; and Tompkins, S. S.:Prediction of Coefficients of Thermal Expansion for Unidirectional Composites. *Journal of Composite Materials*, Vol. 23, April 1989, pp. 370-388.

13. Bowles, D. E.; and Griffin, O. H., Jr.:Analysis of Thermal Stresses in Polymer Matrix Composites. *Proceedings of 34'th International SAMPE Symposium and Exhibition*, May 1989, pp. 575-584.

14. Chamis, C. C.; and Sendeckyj, G. P.:Critique on Theories Predicting Thermoelastic Properties of Fibrous Composites. *Journal of Composite Materials*, Vol. 2, No. 3, July 1968, pp. 332-358.

15. Shapery, R. A.:Thermal Expansion Coefficients of Composite Materials Based on Energy Principles. *Journal of Composite Materials*, Vol. 2, No. 3, 1968, pp. 380.

16. Strife, J. R.; and Prewo, K. M.:The Thermal Expansion Behavior of Unidirectional and Bidirectional Kevlar/Epoxy Composites. *Journal of Composite Materials*, Vol. 13, October 1979, pp. 264-277.

17. Chamberlain, N. J.:Derivation of Expansion Coefficients for a Fibre Reinforced Composite. *BAC Report SON(P) 33*, November 1968.

18. Rogers, K. F; Phillips, L. N.; Kingston-Lee, D. M.; Yates, B.; Overy, M. J.; Sargent, J. P.; and McCalla, B. A.:The Thermal Expansion of Carbon Fibre Reinforced Plastics. *Journal of Materials Science*, Vol. 12, 1977, pp. 718-734.

19. Chamis, C. C.:Simplified Composite Micromechanics Equations for Hygral, Thermal, and Mechanical Properties. *SAMPE Quarterly*, Vol. 15, No. 3, April 1984, pp. 14-23.

20. Caruso, J. J.; and Chamis, C. C.:Assessment of Simplified Composite Micromechanics Using Three-Dimensional Finite Element Analysis. *Journal of Composites Technology and Research*, Vol. 8, No. 3, Fall 1986, pp. 77-83.

21. Rosen, B. W.; and Hashin, Z.:Effective Thermal Expansion Coefficients and Specific Heats of Composite Materials. *International Journal of Engineering Science*, Vol. 8, 1970, pp. 157-173.

22. Levin, V. M.:Thermal Expansion Coefficients of Heterogeneous Materials. *Mechanics of Solids*, Vol. 2, No. 1, 1967, pp. 58-61.

23. Hashin, Z.:Analysis of Properties of Fiber Composites with Anisotropic Constituents. *Journal of Applied Mechanics*, Vol. 46, September 1979, pp. 543-550.

24. Adams, D. F.; and Miller, A. K.:Hygrothermal Microstresses in a Unidirectional Composite Exhibiting Inelastic Material Behavior. *Journal of Composite Materials*, Vol. 11, July 1977, pp. 285-299.

25. Miller, A. K.; and Adams, D. F.:Inelastic Finite Element Analysis of a Heterogeneous Medium Exhibiting Temperature and Moisture Dependent Material Properties. *Fiber Science and Technology*, Vol. 13, 1980, pp. 135-153.

26. Adams, D. F.; and Crane, D. A.:Finite Element Micromechanical Analysis of a Unidirectional Composite Including Longitudinal Shear Loading. *Computers and Structures*, Vol. 18, No. 6, 1984, pp. 1153-1165.

27. Adams, D. F.:A Micromechanics Analysis of the Influence of the Interface on the Performance of Polymer-Matrix Composites. *Journal of Reinforced Plastics and Composites*, Vol. 6, January 1987, pp. 66-88.

28. Foye, R. L:Theoretical Post-Yielding Behavior of Composite Laminates, Part I-Inelastic Micromechanics. *Journal of Composite Materials*, Vol. 7, April 1973, pp. 178-193.

29. Dvorak, G. J.; Rao, M. S. M.; and Tarn J. Q.:Yielding in Unidirectional Composites Under External Loads and Temperature Changes. *Journal of Composite Materials*, Vol. 7, April 1973, pp. 194-216.

30. Aboudi,J:Generalized Effective Stiffness Theory for the Modeling of Fiber-Reinforced Composites. *International Journal of Solids and Structures*, Vol.17, No. 10, 1981, pp. 1005-1018.

31. Aboudi, J:Minimechanics of Tri-Orthogonally Fiber-Reinforced Composites: Overall Elastic and Thermal Properties. *Fiber Science and Technology*, Vol. 21, 1984, pp. 277-293.

32. Aboudi, J:Elastoplasticity Theory for Composite Materials. *Solid Mechanics Archives*, Vol. 11, No. 3, 1986, pp. 141-183.

References

33. Pindera, M. J.; Aboudi, J; and Herakovich, C. T.:Nonlinear Response of Boron/Aluminum Under Combined Loading. *Proceedings of IUTAM/ICM on Yielding, Damage, and Failure of Anisotropic Solids*, August, 1987.

34. Hashin, Z:Theory of Fiber Reinforced Materials. *NASA CR- 1974*, March 1972.

35. Avery, W. B.; and Herakovich, C. T.:Effect of Fiber Anisotropy on Thermal Stresses in Fibrous Composites. *Journal of Applied Mechanics*, Vol. 53, December 1986, pp. 751-756.

36. Mikata, Y.; and Taya, M.:Stress Field in a Coated Continuous Fiber Composite Subjected to Thermomechanical Loadings. *Journal of Composite Materials*, Vol. 19, November 1985, pp. 554-578.

37. Min, B. K.:A Plane Stress Formulation for Elastic-Plastic Deformation of Unidirectional Composites. *Journal of the Mechanics and Physics of Solids*, Vol. 29, No. 4, 1981, pp. 327-352.

38. Dvorak, G. J.; and Bahei-El-Din, Y. A.:Plasticity Analysis of Fibrous Composites. *Journal of Applied Mechanics*, Vol. 49, June 1982, pp. 327-335.

39. Chamis, C. C.:Simplified Composite Micromechanics for predicting Microstresses. *Journal of Reinforced Plastics and Composites*, Vol. 6, July 1987, pp. 268-289.

40. Carnahan, B; Luther, H. A.; and Wilkes, J. O.:*Applied Numerical Methods.* John Wiley and Sons, Inc., New York, 1969.

41. Zienkiewicz, O. C.:*The Finite Element Method.* McGraw-Hill Book Company, New York, NY, 1977.

42. Cohen, D.; and Hyer, M. W.:Residual Stresses in Cross-Ply Composite Tubes. *CCMS-84-04*, Virginia Tech, 1984.

43. Jones, R. M.:*Mechanics of Composite Materials.* Scripta Book Company, Washington, D.C., 1975.

44. Pagano, N. J.:Thickness Expansion Coefficients of Composite Laminates. *Journal of Composite Materials*, Vol. 8, July 1974, pp. 310- 312.

45. Hahn, H. T.; and Pagano, N. J.:Curing Stresses in Composite Laminates. *Journal of Composite Materials*, Vol. 9, January 1975, pp. 91-106.

46. Tompkins, S. S.; Bowles, D. E.; and Kennedy, W. R.:A Laser-Interferometric Dilatometer for Thermal Expansion Measurements of Composites. *Experimental Mechanics*, Vol. 26, No. 1, March 1986, pp. 1-6.

47. Wicks, J. B.; and Coyle, R. A.:Microstructural Inhomogeneity in Carbon Fibers. *Journal of Materials Science*, Vol. 11, 1976, pp. 376-383.

48. Barnet, F. R.; and Norr, M. K.:A Three-Dimensional Structural Model for a High Modulus Pan-Based Carbon Fiber. *Composites*, April 1976, pp. 93-99.

49. Brydges, W. T.; Badami, D. V.; Joiner, J. C.; and Jones, G. A.:The Structure and Elastic Properties of Carbon Fibers. *Applied Polymer Symposia*, No. 9, 1969, pp. 255-261.

50. Diefendorf, R. J.; and Tokarsky, E.:High Performance Carbon Fibers. *Polymer Engineering and Science*, Vol. 15, No. 3, March 1975, pp. 150-159.

51. Guigon, M.; and Oberlin, A.:Structure and Microtexture of Some Pitch-Base Fibers. *Proceedings of 16'th Biennial Conference on Carbon*, July 1983, pp. 513-514.

52. Knott, T.W.:Effect of Fiber Morphology on Composite Properties, *M.S. Thesis*, Virginia Tech, May 1988.

53. Wolff. E. G.:Stiffness-Thermal Expansion Relationships in High Modulus Carbon Fibers. *Journal of Composite Materials*, Vol. 21, January 1987, pp. 81-97

54. Kowalski, I. M.:Determining the Transverse Modulus of Carbon Fibers. *SAMPE Journal*, July/August 1986, pp. 38-42.

55. Helmer, J. F.; and Diefendorf, R. J.:Transverse Thermal Expansion of Carbon Fiber/Epoxy Matrix Composites. *Proceedings of 5th International Symposium on Composite Metallic Materials*, November 1983, pp. 15-20.

56. Thornel Carbon Fiber Data Sheets, Amoco, 1987.

57. Hercules Carbon Fiber Data Sheets, Hercules Inc., 1984.

58. *Handbook of Applied Engineering Science*, Bolz, R. E. and Tuve, G. L. Editors, CRC Press, 1972.

59. Fox, D. J.; Sykes, G. F.; and Herakovich, C. T.:Space Environmental Effects on Graphite/Epoxy Compressive Properties and Epoxy Tensile Properties. *CCMS-87-11*, Virginia Tech, July 1987.

60. Milkovich, S. M.; Sykes, G.F.; and Herakovich, C. T.:Space Radiation Effects on the Thermo-Mechanical Behavior of Graphite/Epoxy Composites. *Journal of Composite Materials*, Vol. 20, No. 6, November 1986, pp. 579-593.

61. Tompkins, S. S.:Thermal Expansion of Selected Graphite Reinforced Polyimide-, Epoxy-, and Glass-Matrix Composites. *International Journal of Thermophysics*, Vol. 8, No.1, January 1987, pp. 119-132.

62. Dries, G. A.; and Tompkins, S. S.:Effects of Thermal Cycling on Thermal Expansion and Mechanical Properties of Several Graphite-Reinforced Aluminum Metal-Matrix Composites. *NASA TP2701*, 1987.

63. Tsai, S. W.; and Hahn, H. T.:*Introduction to Composite Materials.* Technomic Publishing Company, Westport, CT, 1980.

64. Margolis, J. M.:*Engineering Thermoplastics, Properties and Applications.* Marcel Dekker, Inc., New York, NY, 1985.

65. Silverman, E. M.; Griese, R. A.; and Forbes, W. C.:Property Performance of Thermoplastic Composites for Spacecraft Systems. *SAMPE Journal*, Vol. 25, No. 6, November/December 1989, pp. 38-47.

66. Frederick, D.; and Chang, T. S.:*Continuum Mechanics.* Scientific Publishers, Inc., Boston, MA, 1972.

Appendix A. Rosen and Hashin Analysis

Due to the transverse isotropy of the constituents and the unidirectional composite, the only non-zero components in the material property tensors of equations (2.1.8) and (2.1.9) are given by[23]

$$\alpha_{11} = \alpha_{(1)}, \quad \alpha_{22} = \alpha_{33} = \alpha_{(2)}$$

$$S_{1111} = 1/E_{(1)}, \quad S_{2222} = S_{3333} = 1/E_{(2)}$$

$$S_{1122} = S_{1133} = -\nu_{(12)}/E_{(1)}, \quad S_{2233} = -\nu_{(23)}/E_{(2)} \qquad (A.1)$$

$$S_{1212} = S_{1313} = 1/4G_{(12)}, \quad S_{2233} = 1/4G_{(23)}$$

These relations are true for the effective property (superscript $^{-}$), the volume average property (superscript $^{\wedge}$), and the constituent property (superscripts f,m) tensors. The subscripts on the engineering constants refer to the material property coordinates of Figure 4, and are enclosed in parentheses to distinguish them from tensor indices.

Using contracted tensor notation[66] (subscripts a,b = 1,2,3,4,5,6), equation (A.1) may be rewritten as

$$\alpha_1 = \alpha_{(1)}, \quad \alpha_2 = \alpha_3 = \alpha_{(2)}$$

$$S_{11} = 1/E_{(1)}, \quad S_{22} = S_{33} = 1/E_{(2)}$$

$$S_{12} = S_{13} = -\nu_{(12)}/E_{(1)}, \quad S_{23} = -\nu_{(23)}/E_{(2)} \tag{A.2}$$

$$S_{66} = S_{55} = 1/4G_{(12)}, \quad S_{44} = 1/4G_{(23)}$$

Now, equations (2.1.11a) and (2.1.11b) may be rewritten using contracted notation as

$$\alpha_1 = \hat{\alpha}_1 + (\alpha_a^{(f)} - \alpha_a^{(m)})P_{ab}(\bar{S}_{b1} - \hat{S}_{b1}) \tag{A.3}$$

$$\alpha_2 = \hat{\alpha}_2 + (\alpha_a^{(f)} - \alpha_a^{(m)})P_{ab}(\bar{S}_{b2} - \hat{S}_{b2}) \tag{A.4}$$

Equations (A.3) and (A.4) may be expanded and simplified by keeping only the nonzero terms and noting that S_{ab} is symmetric and therefore P_{ab} is symmetric. The following relations can also be shown for P_{ab}

$$P_{22} = P_{33}, \quad P_{12} = P_{13}, \quad P_{55} = P_{66} \tag{A.5}$$

Equations (A.3) and (A.4) may now be written as

$$\alpha_1 = \hat{\alpha}_1 + (\bar{S}_{11} - \hat{S}_{11})[(\alpha_1^{(f)} - \alpha_1^{(m)})P_{11} + (\alpha_2^{(f)} - \alpha_2^{(m)})2P_{12}]$$

$$+ (\bar{S}_{12} - \hat{S}_{12})[(\alpha_1^{(f)} - \alpha_1^{(m)})2P_{12} + (\alpha_2^{(f)} - \alpha_2^{(m)})2(P_{22} + P_{23})] \tag{A.6}$$

$$\alpha_2 = \hat{\alpha}_2 + (\bar{S}_{12} - \hat{S}_{12})[(\alpha_1^{(f)} - \alpha_1^{(m)})P_{11} + (\alpha_2^{(f)} - \alpha_2^{(m)})2P_{12}]$$

$$+ (\bar{S}_{22} - \hat{S}_{22})[(\alpha_1^{(f)} - \alpha_1^{(m)})P_{12} + (\alpha_2^{(f)} - \alpha_2^{(m)})(P_{22} + P_{23})]$$

$$+ (\bar{S}_{23} - \hat{S}_{23})[(\alpha_1^{(f)} - \alpha_1^{(m)})P_{12} + (\alpha_2^{(f)} - \alpha_2^{(m)})(P_{23} + P_{33})] \qquad (A.7)$$

where P_{ab} is determined from equation (2.1.9) which may be rewritten in contracted form as

$$P_{ab}(S_{bc}^{(f)} - S_{bc}^{(m)}) = I_{ac} \qquad (A.8)$$

The solution of equation (A.8) gives the elements of P_{ab} appearing in equations (A.6) and (A.7), and may be written as

$$P_{11} = (A_{22}A_{22} - A_{23}A_{23})/\text{Det } A$$

$$P_{12} = (A_{12}A_{23} - A_{22}A_{12})/\text{Det } A$$

$$P_{22} = (A_{11}A_{22} - A_{12}A_{12})/\text{Det } A \qquad (A.9)$$

$$P_{23} = (A_{12}A_{12} - A_{11}A_{23})/\text{Det } A$$

where A_{ab} is defined as $(S_{ab}^{(f)} - S_{ab}^{(m)})$, and Det A is given by

$$\text{Det } A = [A_{11}(A_{22}A_{22} - A_{23}A_{23}) + 2A_{12}(A_{12}A_{23} - A_{22}A_{12})] \qquad (A.10)$$

Appendix B. Finite Element Formulation

As stated in **Section 3.4**, 8-node quadratic isoparametric elements were used for the FE analysis. The global and local coordinate systems for this element are shown in Figure B1. The relationship between the global and local coordinates can be written as

$$y = \sum_{i=1}^{8} N_i y_i \tag{B.1}$$

$$z = \sum_{i=1}^{8} N_i z_i \tag{B.2}$$

where the interpolation polynomials N_i are functions of the local nodal coordinates (ξ, η), and y_i and z_i are the global coordinates of the i'th node.

The interpolation polynomials for the 8-node elements are quadratic, and defined as

$$N_i = \frac{1}{4}(1 + \xi_0)(1 + \eta_0)(\xi_0 + \eta_0 - 1), \quad i = 1, 3, 5, 7 \tag{B.3}$$

$$N_i = \frac{1}{2}(1 - \xi^2)(1 + \eta_0), \quad \xi_i = 0, \quad i = 2, 6 \tag{B.4}$$

$$N_i = \frac{1}{2}(1 + \xi_0)(1 - \eta^2), \quad \eta_i = 0, \quad i = 4, 8 \tag{B.5}$$
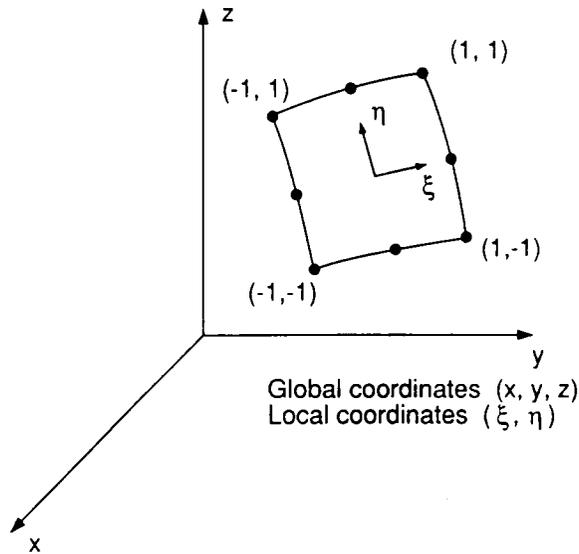
**Figure B1. Element local and global coordinate systems.**

where $\xi_o = \xi\xi_i$, $\eta_o = \eta\eta_i$, and ξ and η range from -1 to $+1$ at the corners.

Isoparametric elements use the same interpolation functions for the geometry and the nodal variables (i.e. displacements). Therefore, the unknown displacement functions of equation (3.4.1) may be written as

$$U(y,z) = \sum_{i=1}^{8} N_i u_i$$

$$V(y,z) = \sum_{i=1}^{8} N_i v_i \qquad \qquad (B.6)$$

$$W(y,z) = \sum_{i=1}^{8} N_i w_i$$

where u_i, v_i, and w_i are the unknown displacements at the nodes.

A displacement based FE formulation requires the minimization of the total potential energy, PE, for each element with respect to the unknown variables. This procedure leads to a set of linear simul-

taneous equations relating the unknown nodal displacements to the applied loads. The equations for each element are assembled into a global system, the boundary conditions are applied, and the system is solved for the nodal displacements. A detailed description of this procedure may be found in the literature[41]. An abbreviated description of this general procedure, and special modifications for the specific problem under consideration, follows.

The total PE of an element is the sum of the strain energy, U_S, and the work of the external loads, W_L. The strain energy for an element is written as

$$U_S = \frac{1}{2} \int_{vol} \{\sigma\}\{\epsilon_M\} dvol \qquad (B.7)$$

where $\{\sigma\}$ and $\{\epsilon_M\}$ are the element stresses and mechanical strains, respectively, and have the form

$$\{\sigma\}^T = \{\sigma_x, \sigma_y, \sigma_z, \tau_{yz}, \tau_{zx}, \tau_{xy}\} \qquad (B.8)$$

$$\{\epsilon_M\}^T = \{\epsilon_x, \epsilon_y, \epsilon_z, \gamma_{yz}, \gamma_{zx}, \gamma_{xy}\} \qquad (B.9)$$

The work of the external loads is written as

$$W_L = -\{q\}\{f\}^T - \epsilon_x^o F_x^o \qquad (B.10)$$

where $\{q\}$ are the nodal displacements, $\{f\}$ are the applied nodal loads, and F_x^o is the uniform average axial force (i.e. a scalar quantity).

The total strain for a linear elastic system is written as the sum of the mechanical strain and the free thermal strain, or

$$\{\epsilon\} = \{\epsilon_M\} + \{\epsilon_T\} \qquad (B.11)$$

Rearranging to solve for the mechanical strain leads to

$$\{\epsilon_M\} = \{\epsilon\} - \{\epsilon_T\} \qquad (B.12)$$

Minimization of the total PE with respect to the nodal displacements requires that $\{\sigma\}$ and $\{\epsilon_M\}$ in equation (B.7) be expressed in terms of the displacements, and is accomplished by using the strain-displacement relationships of linear strain theory. These relationships are written in matrix form as

$$\{\epsilon\} = [L]\{u\} \tag{B.13}$$

where $\{u\}$ is the vector of total displacements, and the matrix $[L]$ is defined as

$$\begin{bmatrix} \partial/\partial x & 0 & 0 \\ 0 & \partial/\partial y & 0 \\ 0 & 0 & \partial/\partial z \\ 0 & \partial/\partial z & \partial/\partial y \\ \partial/\partial z & 0 & \partial/\partial x \\ \partial/\partial y & \partial/\partial x & 0 \end{bmatrix} \tag{B.14}$$

Note that engineering shear strain has been used in the above relationships.

Combining equations (3.4.1) and (B.6) and substituting into equation (B.13) leads to an expression for strain in terms of the nodal displacements written as

$$\{\epsilon\} = [B]\{q\} + \{\epsilon_x^0\} \tag{B.15}$$

where

$$\{q\}^T = \{u_1, v_1, w_1, \ldots u_8, v_8, w_8\} \tag{B.16}$$

and

$$\{\epsilon_x^0\}^T = \{\epsilon_x^0, 0, 0, 0, 0, 0\} \tag{B.17}$$

The matrix $[B]$ (6×24) is defined as the matrix product of $[L]$ and a partitioned matrix involving the interpolation polynomials (equations (B.3- B.4)) written as

$$[B] = ([L]) \, ([I](N_1)|[I](N_2)| \ldots [I](N_8)) \tag{B.18}$$

where I is a 3x3 identity matrix. Substitution of equation (B.15) into equation (B.12) leads to an expression for the mechanical strains in terms of the displacements, written as

$$\{\epsilon_M\} = [B]\{q\} + \{\epsilon_x^0\} - \{\epsilon_T\} \tag{B.19}$$

where the free thermal strain vector is defined as

$$\{\epsilon_T\} = \{\alpha\}\Delta T \tag{B.20}$$

and

$$\{\alpha\}^T = \{\alpha_x, \alpha_y, \alpha_z, \alpha_{yz}, \alpha_{zx}, \alpha_{xy}\} \tag{B.21}$$

and ΔT is a uniform change in tempertaure.

The stresses are expressed in terms of the displacements through the material constitutive equations, written in general form as

$$\{\sigma\} = [\bar{C}]\{\epsilon_M\} \tag{B.22}$$

The specific form of $[\bar{C}]$ depends upon the relative orientation of the material principal axes with respect to the global (x,y,z) axes. The elements of $[\bar{C}]$ for an orthotropic material (i.e. a material with 3 principal planes of symmetry) with two different orientations (coincident , and a rotation about the x-axis) are given in **Appendix C**. For rotations about the x-axis, the angle of rotation, θ, varies with position in the yz plane, and therefore varies within a given element. This variation is included in the analysis by computing θ from the global coordinates at each of the Gauss points used for the numerical integration in equations (B.26-B.27) and equations (B.30-B.32). The matrix $\{\alpha\}$, defined in equation (B.21), also depends upon the relative orientation of the principal material axes with respect to the global axes. The elements of $\{\alpha\}$ for the two orientations described above are also given in **Appendix C**.

Equations (B.19) and (B.22) are substituted into equation (B.7) to write an expression for the strain energy in terms of the displacements as

$$U_S = \frac{1}{2} \int_{vol} \{\hat{B}\}^T [\bar{C}] \{\hat{B}\} dvol \qquad (B.23)$$

where

$$\{\hat{B}\} = ([B]\{q\} + \{\epsilon_X^o\} - \{\epsilon_T\}) \qquad (B.24)$$

Two cases must be considered for the minimization of the total PE (equations (B.10) and (B.23)) with respect to the unknowns. First, for the case of a known ϵ_X^o, the PE is minimized with respect to only the nodal displacements, $\{q\}$. This minimization results in an expression written as

$$[K]\{q\} = \{F\} \qquad (B.25)$$

where

$$[K] = \int_{vol} [B]^T [\bar{C}] [B] dvol \qquad (B.26)$$

and

$$\{F\} = - \int_{vol} [B]^T [\bar{C}] (\{\epsilon_X^o\} - \{\epsilon_T\}) dvol + \{f\} \qquad (B.27)$$

The case of an unknown ϵ_X^o requires that the PE be minimized with respect to both the nodal displacements, $\{q\}$, and ϵ_X^o. This formulation is specific to the case of generalized plane strain with an applied uniform axial force, F_X^o, and does not appear in the reference[41] cited previously. The minimization of the PE for this case results in an expression of the general form

$$[K^*]\{q^*\} = \{F^*\} \qquad (B.28)$$

which may be expanded and written as

$$\begin{bmatrix} [K] & \{K_x\} \\ \{K_x\}^T & K_x^o \end{bmatrix} \begin{Bmatrix} \{q\} \\ \epsilon_X^o \end{Bmatrix} = \begin{Bmatrix} \{F\} \\ F_X^o - F_x \end{Bmatrix} \qquad (B.29)$$

where $[K]$, $\{q\}$, $\{F\}$, and F_x^o have the same definitions as previously given, and

$$\{K_x\} = 1'\text{st column of } \int_{vol} [B]^T[\bar{C}]dvol \tag{B.30}$$

$$K_x^o = \int_{vol} [\bar{C}_{11}]dvol \tag{B.31}$$

and

$$F_x = 1'\text{st element of } \int_{vol} [\bar{C}]\{\epsilon_T\}dvol \tag{B.32}$$

Two steps are required to compute the elements of $[K]$, $[K^*]$, $\{F\}$, and $\{F^*\}$. First, the derivatives of the interpolation polynomials, N_i, with respect to the global coordinates, (y,z), must be evaluated for terms involving $[B]$. However, the shape functions are in terms of the local element coordinates, (ξ, η). The derivative evaluation is acomplished by use of the Jacobian matrix in an expression written as

$$\left\{ \begin{array}{c} \partial N_i/\partial y \\ \partial N_i/\partial z \end{array} \right\} = [J]^{-1} \left\{ \begin{array}{c} \partial N_i/\partial \xi \\ \partial N_i/\partial \eta \end{array} \right\} \tag{B.33}$$

where the Jacobian matrix is defined as

$$[J] = \begin{bmatrix} \partial N_1/\partial \xi & \cdots & \partial N_8/\partial \xi \\ \partial N_1/\partial \eta & \cdots & \partial N_8/\partial \eta \end{bmatrix} \begin{bmatrix} y_1 & z_1 \\ \vdots & \vdots \\ y_8 & z_8 \end{bmatrix} \tag{B.34}$$

The second step is to numerically evaluate the integrals in equations (B.26- B.32). This is accomplished by first transforming the integral into the (ξ, η) coordinate system noting that

$$dvol = |J|(d\xi)(d\eta) \tag{B.35}$$

where $|J|$ is the determinate of the Jacobian matrix. The limits of integration become -1 to +1 on both ξ and η. Gauss quadrature is used for the integration and all of the integrals can be written in the form

$$\int_{vol} Gdvol = \sum_{i=1}^{n} \sum_{j=1}^{n} H_i H_j G(\xi_i, \eta_j)|J| \tag{B.36}$$

where H_i and H_j are the weight functions and $G(\xi_i, \eta_j)$ is the function to be integrated. A 2x2 (n=2) Gauss quadrature rule was used for the integration. The weight functions and coordinates of the Gauss points are given in the FE reference text cited earlier[41].

Equations (B.25) and (B.29) represent a system of linear simultaneous equations for one element. These element equations are assembled into a global system of equations by requiring continuity of the displacements at the nodes of adjoining elements. The prescribed boundary conditions are imposed and the resulting system of simultaneous linear equations is solved for the unknown nodal dispalcements, and if necessary ϵ_x^0. The element strains and stresses are computed from the nodal displacements by using equations (B.13) and (B.22).

Resultant internal nodal forces are computed from

$$\{P\} = \int_{vol} [B]^T \{\sigma\} dvol \tag{B.37}$$

where P is the vector of resultant nodal forces for an element. The integration in equation (B.37) is evaluated numerically by rewriting it in the form of equation (B.35). The summation of these nodal forces in the x, y, and z directions, respectively, must equal zero for static equilibrium, and can be used as a check on the validity of the solution.

It should be noted that the formulation presented above (i.e. minimization of the total potential energy) insures that [K] and [K*] will be symmetric and positive definite, after the imposition of boundary conditions which prohibit rigid-body motion. Therefore the inverse of [K] and/or [K*] exists and a solution can be found.

The three types of boundary conditions allowed in the displacement formulation presented above are prescribed nodal displacements, applied nodal forces, and constrained nodal displacements. The first two involve standard procedures for appropriately modifying the global stiffness matrix

([K] or [K*]) and load vector ({F} or {F*}), and are well documented in texts on finite element analysis[41]. The application of constrained nodal displacements is not as well documented and requires further explanation. Constrained nodal displacements refer to a series of nodes whose displacements are proportional to one another but whose absolute values are unknown (e.g. $v_1 = v_3 = 4v_6$). This effectively reduces the total number of unknowns in the system. The global stiffness matrix and load vector are modified by combining the contributions of the affected nodes into a single row and/or column. These modifications do not destroy the symmetry of the stiffness matrix, but can increase the bandwidth (to be discussed subsequently). The specifics of the procedure for modifying the stiffness matrix and load vector are given by Adams and Crane[26].

The solution of equations (B.25) or (B.29) involves solving a system of simultaneous linear algebraic equations. As stated earlier, [K] and [K*] will be symmetric and positive definite, and therefore an inverse will exist, and a solution is possible. The matrix [K] will also be banded due to the assembly procedure in which a nodal displacement affects only those elements adjoining that node. However, [K*] is not banded due to the fact that every element contributes to ϵ_x^o. This type of matrix is sometimes refered to as an "arrowhead" matrix. Both matrices are shown schematically in Figure B2. Numerous solution algorithms exist for banded symmetric systems. These algorithms require storage of only the terms that lie on or above the diagonal and within the band, thus greatly reducing the amount of computer memory and time needed for the solution. A special solution algorithm was developed for this study that allows a banded storage scheme to be used for [K*] also. This was accomplished by storing the terms of [K*] which contribute to ϵ_x^o as a separate vector. A standard [L][U] decomposition was then used to solve the banded system for the unknowns, with terms from this separate vector used when needed.
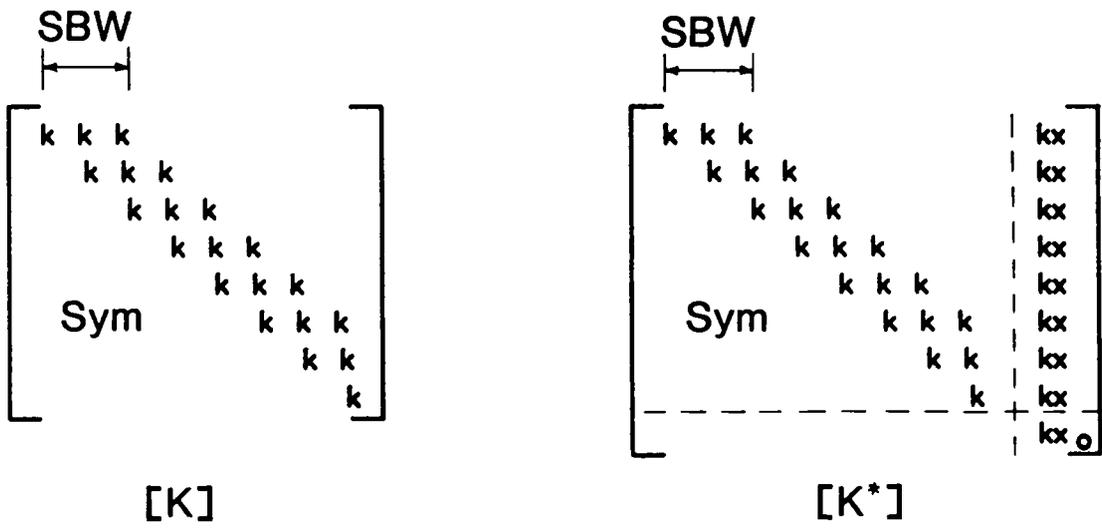
SBW = Semi-bandwidth

Figure B2. Finite element global stiffness matrix architecture.

Appendix C. Finite Element Constitutive Equations

The material stiffness matrix, [C] is a 4'th order symmetric tensor. Following the contracted tensor notation used in **Appendix A**, [C] can be written as a 6x6 symmetric matrix as

$$\begin{bmatrix} C_{11} & C_{12} & C_{13} & 0 & 0 & 0 \\ C_{12} & C_{22} & C_{23} & 0 & 0 & 0 \\ C_{13} & C_{23} & C_{33} & 0 & 0 & 0 \\ 0 & 0 & 0 & C_{44} & 0 & 0 \\ 0 & 0 & 0 & 0 & C_{55} & 0 \\ 0 & 0 & 0 & 0 & 0 & C_{66} \end{bmatrix} \tag{C.1}$$

where the elements of [C] are given by

$$C_{11} = \frac{1 - \nu_{23}\nu_{32}}{E_2 E_3 \Delta} \quad C_{12} = \frac{\nu_{12} + \nu_{32}\nu_{13}}{E_1 E_3 \Delta} \quad C_{13} = \frac{\nu_{13} + \nu_{12}\nu_{23}}{E_1 E_2 \Delta}$$

$$C_{22} = \frac{1 - \nu_{13}\nu_{31}}{E_1 E_3 \Delta} \quad C_{23} = \frac{\nu_{23} + \nu_{21}\nu_{13}}{E_1 E_2 \Delta} \quad C_{33} = \frac{1 - \nu_{12}\nu_{21}}{E_1 E_2 \Delta} \tag{C.2}$$

$$C_{44} = G_{23} \quad C_{55} = G_{31} \quad C_{66} = G_{12}$$

and

$$\Delta = \frac{1 - \nu_{12}\nu_{21} - \nu_{23}\nu_{32} - \nu_{13}\nu_{31} - 2\nu_{21}\nu_{32}\nu_{13}}{E_1 E_2 E_3} \tag{C.3}$$

The terms E_i, G_{ij}, and ν_{ij} in the above equations refer to the Young's moduli, shear moduli, and Poisson's ratios, respectively, in the material principal coordinates.

When the material principal (1,2,3) axes are coincident with the global (x,y,z) axes, then the $[\bar{C}]$ matrix appearing in **Appendix B** is equal to the [C] matrix defined above. This will be the case for most of the micromechanics problems analyzed in this study.

However, materials that possess cylindrical orthotropy (circumferential or radial) in the (2,3) plane require a transformation of the [C] matrix to $[\bar{C}]$. The appropriate transformation involves a rotation about the global x axis, and is shown schematically in Figure C1. The elements of $[\bar{C}]$ are determined using a standard 4'th order tensor transformation law[66], and can be written in contracted notation as

$$\bar{C}_{11} = C_{11}$$

$$\bar{C}_{11} = C_{11}$$

$$\bar{C}_{12} = m^2 C_{12} + n^2 C_{13}$$

$$\bar{C}_{13} = n^2 C_{12} + m^2 C_{13}$$

$$\bar{C}_{14} = mn(C_{12} - C_{13})$$

$$\bar{C}_{22} = m^4 C_{22} + m^2 n^2 (2C_{23} + 4C_{44}) + n^4 C_{33}$$

$$\bar{C}_{23} = m^2 n^2 (C_{22} - 4C_{44} + C_{33}) + (m^4 + n^4) C_{23}$$

$$\bar{C}_{24} = m^3 n(C_{22} - C_{23} - 2C_{44}) + mn^3 (C_{23} + 2C_{44} - C_{33}) \qquad \text{(C.4)}$$

$$\bar{C}_{33} = m^4 C_{33} + m^2 n^2 (2C_{23} + 4C_{44}) + n^4 C_{22}$$

$$\bar{C}_{34} = m^3 n(C_{23} + 2C_{44} - C_{33}) + mn^3 (C_{22} - C_{23} - 2C_{44})$$

$$\bar{C}_{44} = m^4 C_{44} + m^2 n^2 (C_{22} - 2C_{23} - 2C_{44} + C_{33}) + n^4 C_{44}$$

$$\bar{C}_{55} = m^2 C_{55} + n^2 C_{66}$$

$$\bar{C}_{56} = mn(C_{66} - C_{55})$$

$$\bar{C}_{66} = m^2 C_{66} + n^2 C_{55}$$

where all other $\bar{C}_{ij} = 0$, and $m = \cos\theta$ and $n = \sin\theta$.
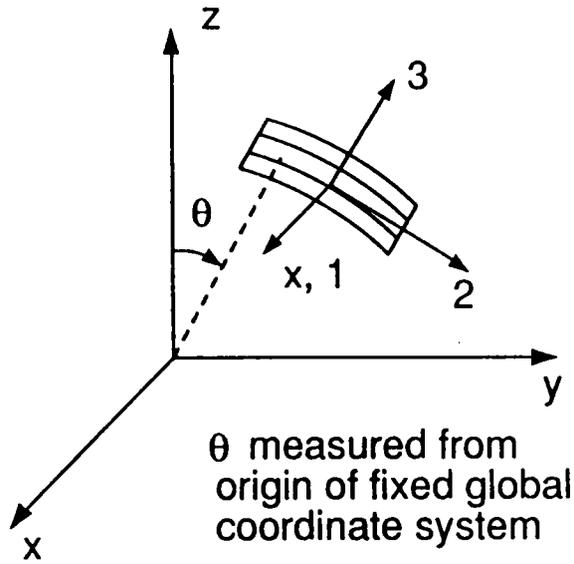
Figure C1. Cylindrical material transformation geometry.

The elements of $\{\alpha\}$ used in **Appendix B**, for orientations where the material principal axes are coincident with the global axes, are defined as

$$\alpha_x = \alpha_1, \quad \alpha_y = \alpha_2, \quad \alpha_z = \alpha_3,$$

$$\alpha_{yz} = 0, \quad \alpha_{zx} = 0, \quad \alpha_{xy} = 0$$

(C.5)

where α_1, α_2, and α_3 are the CTE's in the material principal directions.

The elements of $\{\alpha\}$ for a rotation about the global x axis are given by

$$\alpha_x = \alpha_1$$

$$\alpha_y = m^2\alpha_2 + n^2\alpha_3$$

$$\alpha_z = n^2\alpha_2 + m^2\alpha_3$$

$$\alpha_{yz} = 2mn(\alpha_2 - \alpha_3)$$

(C.6)

$$\alpha_{zx} = 0$$

$$\alpha_{xy} = 0$$

The above transformation for $\{\alpha\}$ is based on the use of engineering shear strain in the FE formulation, as opposed to tensor shear strain.

Appendix D. Composite Cylinder Solution

The orthotropic constitutive relations in terms of the cylindrical coordinate system of Figure 7 may be written as

$$
\begin{Bmatrix} \sigma_x \\ \sigma_r \\ \sigma_\theta \\ \tau_{r\theta} \\ \tau_{\theta x} \\ \tau_{xr} \end{Bmatrix} = \begin{bmatrix} C_{11} & C_{12} & C_{13} & 0 & 0 & 0 \\ C_{12} & C_{22} & C_{23} & 0 & 0 & 0 \\ C_{13} & C_{23} & C_{33} & 0 & 0 & 0 \\ 0 & 0 & 0 & C_{44} & 0 & 0 \\ 0 & 0 & 0 & 0 & C_{55} & 0 \\ 0 & 0 & 0 & 0 & 0 & C_{66} \end{bmatrix} \begin{Bmatrix} \epsilon_x - \alpha_1 \Delta T \\ \epsilon_r - \alpha_2 \Delta T \\ \epsilon_\theta - \alpha_3 \Delta T \\ \gamma_{r\theta} \\ \gamma_{\theta x} \\ \gamma_{xr} \end{Bmatrix} \qquad \text{(D.1)}
$$

where the [C] matrix has the same definition as given in **Appendix C**, except that the material principal coordinates 1,2, and 3 are coincident with the x, r, and θ directions, respectively, of Figure 7.

The solution to equation (3.3.2.5), presented by Avery and Herakovich[35], has two forms depending upon whether the material is cylindrically orthotropic (i.e. properties in r and θ directions are not equal), or transversely isotropic (i.e. properties in r and θ directions are equal). If the fiber is cylindrically orthotropic the displacements in the fiber are given by

$$
w^f(r) = A_1^f r^{\lambda_1^f} + A_2^f r^{\lambda_2^f} + L_1^f \epsilon_x^o r + L_2^f \Delta T \qquad \text{(D.2)}
$$

where

$$
L_1^f = \frac{C_{13} - C_{12}}{C_{22} - C_{33}} \qquad \text{(D.3)}
$$

and

$$L_2^f = \frac{(C_{ir} - C_{i\theta})\alpha_i}{C_{22} - C_{33}} \qquad (D.4)$$

If the fiber is transversely isotropic the displacements in the fiber are given by a much simpler equation written as

$$w^f(r) = A_1^f r^{\lambda_1^f} + A_2^f r^{\lambda_2^f} \qquad (D.5)$$

The term $\lambda_{1,2}$, in both of the above displacement fields, is given by

$$\lambda_{1,2} = \pm\sqrt{\frac{C_{33}}{C_{22}}} \qquad (D.6)$$

The displacements in the matrix, assuming isotropic material behavior, take the same form as equation (D.5) and are written as

$$w^m(r) = A_1^m r^{\lambda_1^m} + A_2^m r^{\lambda_2^m} \qquad (D.7)$$

where $\lambda_{1,2}$ is given by equation (D.6) using the stiffness coefficients of the matrix phase. For isotropic or transversely isotropic phases the values of λ are given by $\lambda_{1,2} = \pm 1$.

The stresses in each phase are obtained by substituting the the expressions for the radial displacemts, equations (D.2,D.5,D.7), into the first equilibrium equation of **Section 3.3.2** (equation (3.3.2.3)), and the results into equation (D.1). The resulting expressions for the stresses in each phase are given by

$$\sigma_i^f = A_1^f(C_{i\theta}^f + C_{ir}^f \lambda_1^f)r^{\lambda_1-1} + A_2^f(C_{i\theta}^f - C_{ir}^f \lambda_2^f)r^{\lambda_2-1} + M_i^f \epsilon_x^o + N_i^f \Delta T \qquad (D.8)$$

with

$$M_i^f = C_{ix}^f + L_1^f(C_{i\theta}^f + C_{ir}^f) \qquad (D.9)$$

and

$$N_i^f = L_2^f(C_{i\theta}^f + C_{ir}^f) - C_{ij}^f\alpha_j^f \qquad (D.10)$$

for a cylindrically orthotropic fiber, and

$$\sigma_i^f = A_1^f(C_{i\theta}^f + C_{ir}^f) + A_2^f(C_{i\theta}^f - C_{ir}^f)\frac{1}{r^2} + C_{ix}^f\epsilon_x^o - C_{ij}^f\alpha_j^f\Delta T \qquad (D.11)$$

for a transversely isotropic fiber, and

$$\sigma_i^m = A_1^m(C_{i\theta}^m + C_{ir}^m) + A_2^m(C_{i\theta}^m - C_{ir}^m)\frac{1}{r^2} + C_{ix}^m\epsilon_x^o - C_{ij}^m\alpha_j^m\Delta T \qquad (D.12)$$

for an isotropic matrix.

The five constants in the above equations, A_1^f, A_2^f, A_1^m, A_2^m, and ϵ_x^o are determined from the following boundary and continuity conditions.

1. The radial displacement w must be zero at r = 0. This in conjunction with the fact that $\lambda_2^f < 0$ requires that A_2^f be equal to zero.

2. The radial displacement must be continuous across the fiber/matrix interface, $w^f(a) = w^m(a)$.

3. The radial component of stress, σ_r, must be continuous across the fiber matrix interface, $\sigma_r^f(a) = \sigma_r^m(a)$.

4. There are no tractions applied on the outer boundary of the matrix for pure thermal loading, therfore $\sigma_r^m(b) = 0$. The condition that $\tau_{xr}^m(b) = 0$ was already used to determine the constant of integration arising from the solution of the second equilibrium equation (**Section 3.3.2**).

5. The net axial force on the composite must be zero for pure thermal loading, or

$2\pi \int_0^b \sigma_x r dr = 0$.

Conditions 2-4 result in 4 equations that can be solved simultaneously for the remaining unkowns, A_1^f, A_1^m, A_2^m, and ϵ_x^0.